Title	Magnetodielectric Effect Coupled with Magnetization Reversal in Néel N-type Ferrimagnet SmMnO_3
Author(s)	Jung, Jong-Suck
Citation	大阪大学, 2012, 博士論文
Version Type	VoR
URL	https://hdl.handle.net/11094/27507
rights	
Note	

Magnetodielectric Effect Coupled with Magnetization Reversal in Néel *N*-type Ferrimagnet $SmMnO_3$

JONG-SUCK JUNG

SEPTEMBER 2012

JONG-SUCK JUNG   Magnetodielectric Effect Coupled with Magnetization Reversal in Néel N-type Ferrimagnet $SmMnO_3$ SEPTEMBER 2012

Magnetodielectric Effect Coupled with Magnetization Reversal in Néel *N*-type Ferrimagnet $SmMnO_3$

A dissertation submitted to
THE GRADUATE SCHOOL OF ENGINEERING SCIENCE
OSAKA UNIVERSITY
in partial fulfillment of the requirements for the degree of
DOCTOR OF PHILOSOPHY IN ENGINEERING

BY

JONG-SUCK JUNG

SEPTEMBER 2012

Abstract

Recent discoveries of multiferroic properties in some perovskite rare-earth manganites RMnO$_3$ (R = Tb, Dy, Ho, and so on) have attracted considerable interest in terms of fundamental science and potential applications. The multiferroic properties are known to originate from complex magnetic orders such as spiral and E-type antiferromagnetic (AF) orders, which break the inversion symmetry and make the system ferroelectric. Such complex magnetism coupled with multiferroic properties appear in RMnO$_3$ with relatively small ionic radii of the R ions r_R (e.g., R = Tb, Dy, and Ho). On the other hand, RMnO$_3$ with relatively large r_R (R = La, Sm, and Eu) exhibits A-type AF and paraelectric structure without breaking the inversion symmetry. Since the A-type AF RMnO$_3$ shows the non-ferroelectric nature, it had not received much attention in the field of multiferroics research. In this thesis, we focus on one of the non-multiferroic A-type AF RMnO$_3$, SmMnO$_3$, to show a new type of magnetodielectric (or magnetocapacitive) effect. In this thesis, we report the discovery of the magnetocapacitive effect in SmMnO$_3$ and aim to clarify the microscopic origin of the effect.

For this purpose, we grew single crystals of SmMnO$_3$ and investigated their structural, magnetic, and dielectric properties using various experimental techniques such as measurements of magnetization, dielectric constant, and striction in applied magnetic fields. Additionally, we performed hard and soft x-ray magnetic circular dichroism measurements to confirm the magnetic moment configurations of Sm 4f and Mn 3d moments. We place great emphasis on "the large magnetocapacitive effect" observed in relatively high magnetic fields, which has never before been reported in SmMnO$_3$.

First, we studied magnetic and dielectric properties in the absence and presence of magnetic fields for SmMnO$_3$. In weak magnetic fields, no anomaly was observed in the dielectric constant, whereas in strong magnetic fields, we found remarkable first-order-like anomalies in the dielectric constant at around a certain temperature (compensation temperature T_{comp}). The dielectric anomaly is accompanied by a magnetization jump, which

means that there is strong coupling between the magnetism and the dielectric property. Thus, the magnetodielectric coupling gives rise to the large magnetocapacitive effect. We suggested that the MC effect is ascribed to a simultaneous reversal of ferrimagnetically coupled Sm 4*f* and Mn 3*d* moments and is crucially affected by the canting angles of Mn moments. To prove our suggestion of the simultaneous both moment reversals, a hard XMCD measurement was carried out for powder $SmMnO_3$. Though the exact alignment of the Sm and Mn moments against the B_c direction was not defined through the method, it revealed the reversal of both XMCD signals of Mn *K* and Sm *L* edges, indicating the reversal of both moments. Thus, we conclude that the large magnetocapacitive effect originates from the simultaneous reversal of Sm 4*f* and Mn 3*d* moments. Furthermore, we observed peculiar asymmetric magnetocapacitance at T_{comp}, dielectric dispersion commonly appeared in rare-earth manganites, and relaxation time jumps at the transition temperatures (T_{TP}).

Second, we investigated striction for A-type AF manganites, such as $SmMnO_3$ and $EuMnO_3$ by means of strain gauge measurement with and without the application of B_c. The result showed that a significant lattice distortion (magnetostriction) appeared at a temperature around T_{comp}, where the anomalies were observed in the magnetization and the dielectric constant. We explained the origin of magnetostrictive effect in terms of relative orbital-occupancy change in Mn e_g electrons. In addition, it revealed that the rare earth moments may enhance the effect.

Finally, we performed soft XMCD to clarify the magnetic states of Sm 4*f* and Mn 3*d* moments below and above T_{comp} in the applied weak and strong magnetic fields. Based on obtained XMCD signals of Sm *M* and Mn *L* edges, we successfully observed the reversal of Mn spin angular, Sm spin angular, and Sm orbital angular momenta at T_{TP} at the same time. We propose that origin of the magnetocapacitive effect observed in $SmMnO_3$ is attributed to intimate combination among magnetic configurations, lattice distortion, and *p*-*d* hybridization.

In conclusion, we found that the Néel *N*-type ferrimagnet $SmMnO_3$, in which the Sm-Mn moments are aligned in the antiparallel configuration, shows a close correlation between magnetic and dielectric properties. The correlation crucially affects the dramatic and large magnetodielectric effect induced by the simultaneous reversal of Sm 4*f* and Mn 3*d* moments. This newly discovered magnetodielectric material (and effect) may evoke interest in terms of fundamental science and potential applications.

Contents

Chapter 1.

Introduction

The revival of coupling between magnetic and (ferro) electric properties called as the magnetoelectric (ME) effect - induction of magnetization (or polarization) by an electric field (or a magnetic field) - with discovery of "spin-driven ferroelectricity" in $TbMnO_3$ [1] has created considerable interest because of the obvious potential for technical application such as memory devices [2,3]. Since this class of materials in which (ferro or antiferro) magnetic and ferroelectric orders simultaneously coexist, namely, multiferroics, displays a gigantic ME response by applying magnetic fields, it approaches applicability closer to the application. Recently, the advent of Z-type hexaferites representing the ME multiferroics in a low magnetic field at room temperature has become an important step towards practical device applications [4].

There is another class of intriguing materials, magnetodielectrics, in which magnetic and dielectric properties are intimately coupled differently from the ME multiferroics. This is partly spurred not only by the related problem of understanding the ME coupling origin, but by new potential devices such as tunable filters, magnetic sensors, and spin-charge transducers [5]. In spite of such interest in the magnetodielectric(s) (effect), it had never attracted much attention in multiferroics field of rare-earth manganite (RMnO$_3$) systems due to its lack of ferroelectric nature. However, in this thesis, we present the discovery and understanding of a new type of the magnetodielectric effect in RMnO$_3$.

In this chapter, we first overview former studies of the ME multiferroics, properties of perovskite RMnO$_3$, and the Néel N-type ferrimagnet. Next, we introduce the magnetic properties of $SmMnO_3$ which are the groundwork for this study. Finally, we explain the motivation and purpose of this thesis.

1.1. Background of this study

1.1.1. Magnetoelectric (ME) effect

It was discovered by Faraday that there is a connection between electricity and magnetism, and the connection was then theoretically described by Maxwell. The magnetoelectric effect, which is the induction of magnetization by an electric field or the induction of electric polarization by a magnetic field by coupling between magnetic and electric orders, was assumed by Pierre Curie on the basis of symmetry consideration in 1894 [6]. The magnetoelectric effect was actively studied in the 1960s and 1970s [7,8] after the theoretical prediction by Dzyaloshinskii using a real material Cr_2O_3 in 1959 [9] and the first experimental observation by Astrov in 1960 [10]. Since after, the effect has continued to attract interest for more than five decades. It is expected that by using the magnetoelectric effect, new applications, such as memory devices [11] in which magnetic (ferroelectric) domains are controlled by an electric (magnetic) field, will be possible.

Formulation of ME effect obtained from the expansion of the free energy

A systematic expression of contributions to the ME effect described in Landau theory can be obtained from the expansion of the free energy *F* of a material [2] as follows:

$$F(\boldsymbol{E},\boldsymbol{H}) = F_0 - P_i^S E_i - M_i^S H_i - \frac{1}{2}\varepsilon_0\varepsilon_{ij}E_iE_j - \frac{1}{2}\mu_0\mu_{ij}H_iH_j - \alpha_{ij}E_iH_j - \frac{1}{2}\beta_{ijk}E_iH_jH_k - \frac{1}{2}\beta_{ijk}H_iE_jE_k - \cdots, \tag{1.1}$$

with ***E*** and ***H*** presenting the electric and magnetic field, respectively. Here, P_i^S, M_i^S, ε_0, μ_0, ε_{ij}, and μ_{ij} are spontaneous polarization, spontaneous magnetization, electric constant of vacuum, magnetic permittivity of vacuum, electric susceptibility, and magnetic susceptibility, respectively. Differentiation leads to the electric polarization $\boldsymbol{P}$:

$$P_i(\boldsymbol{E},\boldsymbol{H}) = -\frac{\partial F}{\partial E_i}$$

$$= P_i^S + \varepsilon_0\varepsilon_{ij}E_j + \alpha_{ij}H_j + \frac{1}{2}\beta_{ijk}H_jH_k + \gamma_{ijk}H_iE_j -\cdots, \tag{1.2}$$

and to the magnetization $\boldsymbol{M}$:

$$M_i(\boldsymbol{E},\boldsymbol{H}) = -\frac{\partial F}{\partial H_i}$$

$$= M_i^S + \mu_0\mu_{ij}H_j + \alpha_{ij}E_i + \beta_{ijk}E_iH_j + \frac{1}{2}\gamma_{ijk}E_jE_k -\cdots, \tag{1.3}$$

The tensor α_{ij} corresponds to the induction of $\boldsymbol{P}$ ($\boldsymbol{M}$) by $\boldsymbol{H}$ ($\boldsymbol{E}$), which is designated as the linear ME effect:

$$P_i = \alpha_{ij}H_j \text{ and } M_i = \alpha_{ij}E_j \ (\boldsymbol{P} = \tilde{\alpha}\boldsymbol{H} \text{ and } \boldsymbol{M} = \tilde{\alpha}\boldsymbol{E}), \tag{1.4}$$

where α_{ij} is the linear ME effect coefficient, which is a component of the linear ME tensor $\tilde{\alpha}$. The tensors $\tilde{\beta}$ and $\tilde{\gamma}$ are in Eqs. (1.2) and (1.3) for the higher order ME effects. In general, the research on the ME effect was broadly carried out for the linear ME effect, and it is acceptable to omit the 'linear' and simply to refer to it as the 'ME effect', as the higher order ME effect was normally small.

Symmetry considerations

Searching for new materials representing the ME effect is closely connected with symmetry analysis of the materials. The symmetry requirement is shortly introduced for the manifestation of the ME effect. To explain it, we bring a term, symmetry operation A. By performing the symmetry operation, Eq. (1.4) is switched to

$$AP = \tilde{\alpha} AH \quad \text{and} \quad AM = \tilde{\alpha} AE \tag{1.5}$$

Using the fact that **E** and **P** are polar vectors, whereas **H** and **M** are axial vectors, we find that

$$\begin{aligned} IE &= -E, \quad RE = E \\ IP &= -P, \quad RP = P \\ IH &= H, \quad RH = -H \\ IM &= M, \quad RM = -M, \end{aligned} \tag{1.6}$$

where I and R are space inversion and time reversal symmetries, respectively. From Eqs. (1.5) and (1.6), it is expected that materials in which I and R are broken at the same time can only show the ME effect.

With the breakthrough of the ME effect material beginning with Cr_2O_3 [9], a variety of ME materials subsequently showed up, such as $LiCoPO_4$ [12], yttrium iron garnet film [13], $TbPO_4$ [14] and so on. However, the observed ME effect from the materials showed a small magnitude of the induced polarization or magnetization for applications. It was further shown that the ME response is limited by the relation [15]

$$\alpha_{ij}^2 < \varepsilon_{ii} \mu_{jj} \tag{1.7}$$

According to Eq. (1.7), the ME coefficient can only be large in ferroelectric and/or ferromagnetic materials. This is a key implication for the development of ME materials.

1.1.2. Multiferroics

Multiferroics are defined as materials that simultaneously have multiple ferroic order properties (i.e., (anti)ferromagnetic, ferroelectric, and ferroelastic properties) [16,17]. In this study, we generally deal with multiferroics as materials showing (anti)ferromagnetic and ferroelectric properties simultaneously. Conventional multiferroics, for example, some boracites ($Ni_3B_7O_{13}I$, etc.) [18], some fluorides ($BaMF_4$) [19], hexagonal manganites ($YMnO_3$, $HoMnO_3$) [20,21], and so on, did not attract as much attention as their ferroelectric ordering temperatures are much larger than their magnetic ones. This demonstrates a weak coupling between magnetism and ferroelectricity indicating a small ME effect. However, this field has gained interest in recent years after the observation of gigantic ferroelectric polarization for $BiFeO_3$ [22] and after the discovery of a new class of multiferroics, $TbMnO_3$, in which ferroelectricity originates from a cycloidal spiral magnetic structure showing a large magnetoelectric effect and resultant giant magnetocapacitance [23].

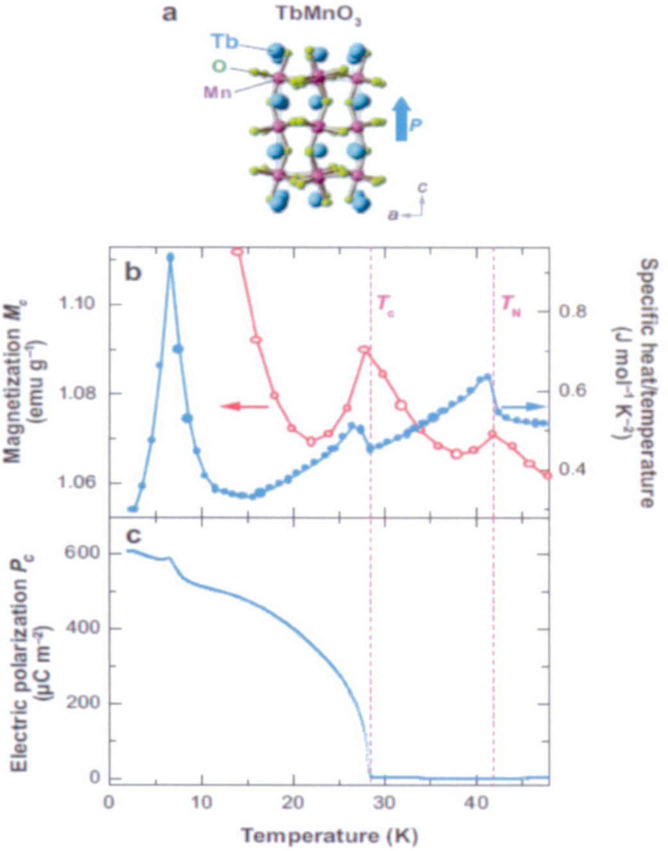

Figure 1.1. Ferroelectricity accompanied by a magnetic transition in TbMnO$_3$.
(a) The orthorhombically distorted perovskite structure, (b) temperature profiles of magnetic susceptibility, and specific heat divided by temperature, and (c) electric polarization along the *c* axis of TbMnO$_3$ [24].

1.1.3. Ferroelectricity induced by magnetic order in TbMnO$_3$ [3,24]

The conventional multiferroics are caused by breaking the inversion symmetry of crystal structures. On the other hand, new classes of multiferroics, such as TbMnO$_3$ and GdMnO$_3$, and so on [25,26,27], induce ferroelectricity by breaking the inversion symmetry through the changed magnetic structure. This magnetically induced ferroelectricity gives rise to strong magnetoelectric coupling and a resulting large ME effect.

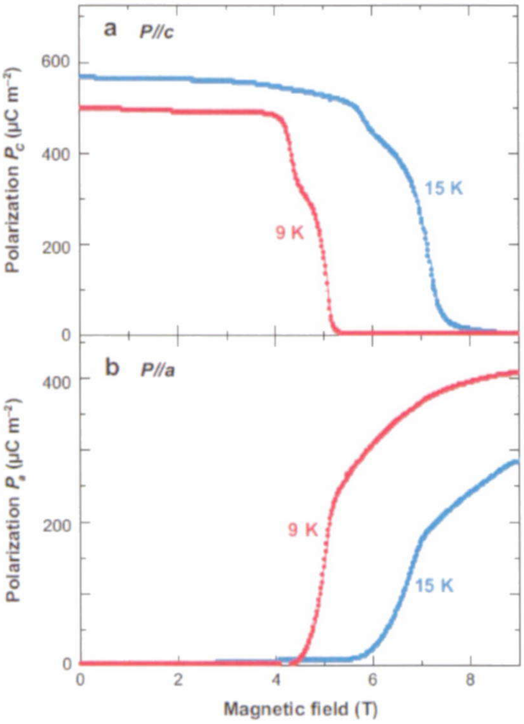

Figure 1.2. Switching of the direction of electric polarization by application of a magnetic field (electric polarization flop). Magnetic-field dependence of electric polarization along the *c* axis (a) and *a* axis (b) in $TbMnO_3$ (*H*//*b*) [24].

Figure 1.1 shows an orthorhombically distorted perovskite structure (the space group *Pbnm* and the point group *mmm*) at room temperature [see Fig. 1.1.a], temperature dependence of magnetization at a magnetic field of 0.5 T and specific heat divided by temperature in Fig.1.1.b, and electric polarization in Fig. 1.1.c along the *c* axis for a single crystal of $TbMnO_3$. $TbMnO_3$ undergoes successive magnetic phase transitions and represents an antiferromagnetic behavior at $T_N \sim 41$ K corresponding to paraelectric behavior at the same time. At lower temperatures, it shows spontaneous polarization at T_C where anomalies of magnetization and specific heat appear. Fig. 1.2 shows the magnetic field dependence of electric polarization along the *c* axis (P_c) and the *a* axis (P_a). Spontaneous polarization can be controlled by a magnetic field (*H*) and can be switched (or flopped) by application of a magnetic field of 4 ~ 8 T from a direction along the *c* axis to that along the *a* axis. The magnetic structures of $TbMnO_3$ have been reported [25,26] to have a collinear sinusoidal spin structure below T_N and a noncollinear spiral spin structure below T_C. It is also known that the spiral spin structure alignment of the magnetic moment gives rise to ferroelecricity. The mechanism of the magnetically induced ferroelectricity will be introduced in the next section with the proposed model, the 'spin current model' [28], or the 'inverse Dzyaloshinskii - Moriya (DM) effect' [29].

Microscopic origin of the magnetically-induced ferroelectricity

In the mechanism of ferroelectricity induced by magnetic structure, noncollinearly lied spiral magnetic structures with cycloidal component are regarded as an important factor. Katsura and coworkers [28] first considered that spin current (or vector spin chirality: $\boldsymbol{S}_i \times \boldsymbol{S}_j$) induced between noncollinearly coupled spins leads to electric polarization. Sergienko and Dagotto [29] reported that the inverse DM effect can be caused when oxygen sandwiched between the two magnetic moments is placed at two noncollinearly coupled magnetic moments and that the electric polarization occurs through electron-lattice interaction. As shown in Fig. 1.3(a), local electric polarization is to be uniform when the noncollinearly coupled magnetic moments are aligned in a cycloidal spiral manner of counterclockwise (CCW) or clockwise (CW) direction.

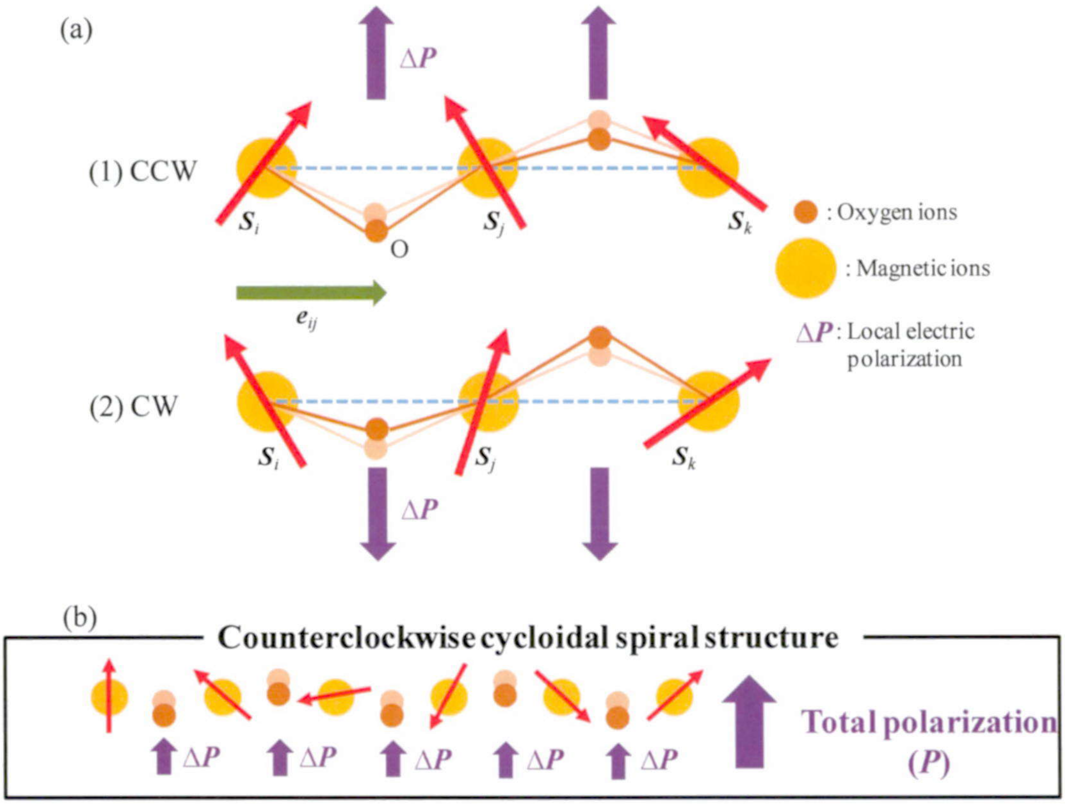

Figure 1.3. Schematics of (a) inverse DM effect with induced local electric polarization (1) counterclockwise cycloidal spiral, (2) clockwise cycloidal spiral structures and of (b) finite electric polarization $\boldsymbol{P}$ expected in cycloidal spiral structure (CCW).

Thus, the total electric polarization is finite as shown in Fig. 1.3(b) by the following equation, in which the total electric polarization can be finite when neighboring magnetic moments are coupled noncollinearly in a spiral manner and when the spin rotation axis is not parallel to the propagation vector.

$$\boldsymbol{P}_{ij} = \gamma \boldsymbol{e}_{ij} \times (\boldsymbol{S}_i \times \boldsymbol{S}_j), \tag{1.8}$$

where γ is a constant proportional to the spin-orbit coupling and superexchange interaction, and e_{ij} is the vector connecting two sites, i and j, along the propagation vector of a spiral structure.

1.1.4. Magnetodielectric (magnetocapacitive) effect

For overviewing the magnetodielectric effect, we refer to the Ph. D. thesis "*Magnetodielectric Coupling in Multiferroic Transition Metal Oxides*" of Dr. Umut Adem from University of Groningen [30].

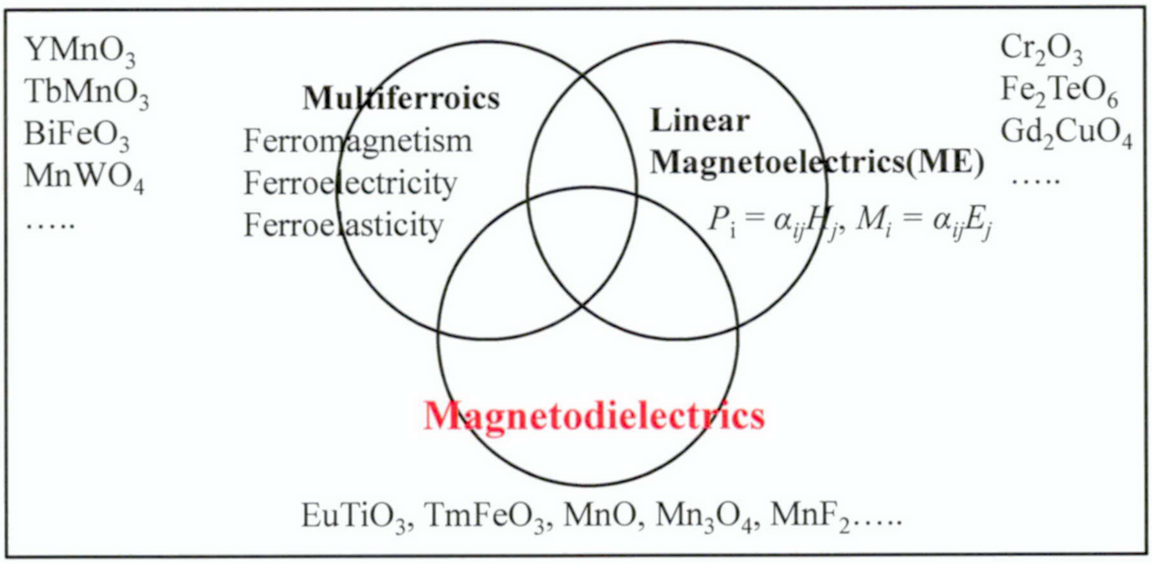

Figure 1.4. Schematics of relationship between multiferroics, the linear magnetoelectrics, and magnetodielectrics

Apart from the classes of magnetoelectrics and multiferroics, another class of material has recently been introduced to distinguish from them. It is denominated as 'magnetodielectics', which possess neither spontaneous polarization nor the ME effect as seen in Fig. 1.4. Nevertheless, it shows a kind of coupling between dielectric and magnetic properties. It was first introduced by Lawes and coworkers who proposed "for more general couplings" the term magnetodielectric effect [31]. Such materials display a change in dielectric constant at the magnetic ordering temperature, or show finite magnetocapacitance. Materials such as MnO [32], MnF_2 [33], $TmFeO_3$ [34], $Tb_3Fe_5O_{12}$ [35] and so on are included in this class.

In the framework of the Ginzburg-landau theory for the second-order phase transition, Smolenskii [36], Kimura, and their coworkers [37] explained the origin of the anomaly in dielectric constant ε on the magnetic order of the ferroelectromagnets, that is, multiferroics. In a ferroelectromagnets, the thermodynamic potential ϕ can be written in the form:

$$\phi = \phi_0 + \alpha P^2 + \frac{\beta}{2} P^4 - PE + \alpha' M^2 + \frac{\beta'}{2} M^4 - MH + \gamma P^2 M^2 \ , \tag{1.9}$$

where α, β, α', β', and γ are functions of temperature. The term of exchange ME interaction of the form $\gamma P^2 M^2$ is allowed in any ferroelectromagnet and in any symmetry. Eq. (1.9) was used to calculate the effect of magnetic ordering on the dielectric susceptibility, $\chi = \varepsilon + 1$. Thus, the dielectric constant ε can be derived using $\chi^{-1} = \partial^2 \phi / \partial P^2$. It can be expressed that the change in ε is proportional to the square of magnetization ($\delta\varepsilon \sim \gamma M^2$) [37]. Figure 1.5 displays a good example of the relationship.

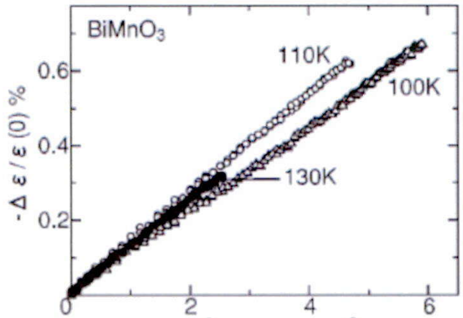

Figure 1.5. Magnitude of field-induced change of ε, $\Delta\varepsilon/\varepsilon(0)$, as function of square of magnetization M^2 at temperatures in the vicinity of magnetic ordering in $BiMnO_3$ [37].

1.2. Perovskite RMnO$_3$ (R = rare-earth)

In this section, I introduce details of the magnetic phase diagram of rare-earth manganites RMnO$_3$ with the distorted perovskite structure.

1.2.1. Various magnetic structures modulated by *R* ion radii

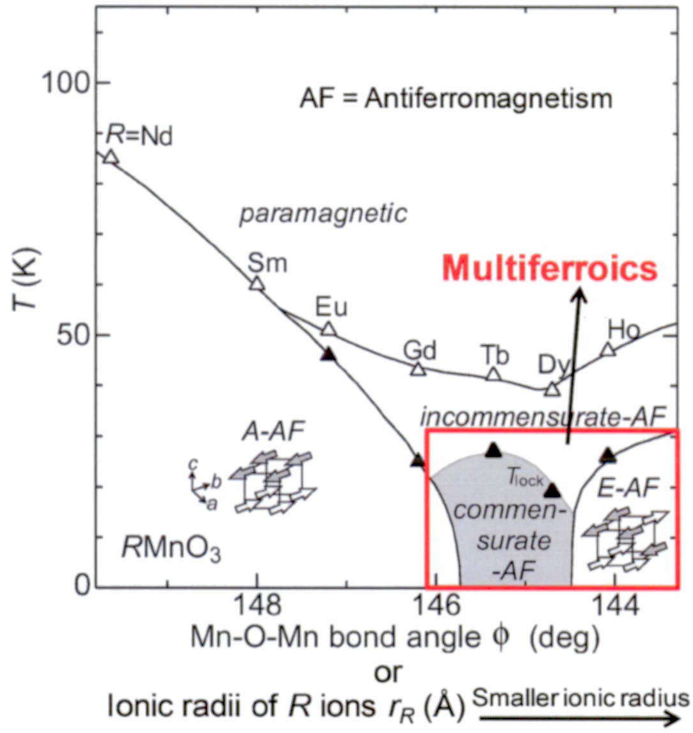

Figure 1.6. Transformation of magnetic structure for RMnO$_3$ modulated by ionic radii of R ions or Mn-O-Mn bond angle [23,38].

In all the perovskite rare-earth manganites with Jahn–Teller active Mn^{3+} ions, an orbital ordered state is stabilized [39]. The onset temperature for the orbital ordering is 770 K in LaMnO$_3$ with the largest ionic radius of the R site (r_R), increasing with decreasing r_R, and reaching more than 1000 K in some RMnO$_3$ such as NdMnO$_3$. In substituting smaller R^{3+}

ions for the La^{3+} ion, the Mn-O-Mn bond angle connecting MnO_6 octahedra decreases and the $GdFeO_3$-type distortion increases by reason of an expansion of the vacancy for the octahedron network. As a result, the change in the bond angle or the $GdFeO_3$-type distortion (an enhancement of the cooperative rotation of the MnO_6 octahedra) leading to variation of superexchange interactions between neighboring (and further-neighboring) Mn ions through O ions affects the magnetic structures of $R\text{MnO}_3$. This bond angle (or r_R) and the superexchange interaction dependences of the magnetic structure have been well studied by Kimura and coworkers [38]. As displayed in Fig. 1.6, the ground state of $R\text{MnO}_3$ with large r_R (e.g., R = La, Sm, and Eu) is a paraelectric A-type antiferromagnetic (AF) ordered phase in which Mn moments are aligned ferromagnetically within the *ab* plane but antiferromagnetically in the *c* direction in the ***Pbnm*** notation (will be introduced in next section). On the other hand, the two magnetic structures, spiral and/or collinear E-type AF structures which present the multiferroic nature, are stabilized in $R\text{MnO}_3$ with intermediate (e.g., R = Tb and Dy) [25,26] and small (e.g., R= Ho and Tm) [40,41] r_R, respectively.

1.2.2. A-type antiferromagnetic order in $LaMnO_3$

Here, we explain the A-type AF structure using $LaMnO_3$ as a good model and well-studied in $R\text{MnO}_3$ materials. The magnetic structure of $LaMnO_3$ can be explained in terms of the electronic configuration and the crystal structure. In a MnO_6 octahedron of the perovskite $LaMnO_3$, five-fold degenerated 3*d* orbitals in the Mn ion are split onto three t_{2g} orbitals (d_{xy}, d_{yz}, d_{zx}) avoiding the oxygen ion direction and two e_g orbitals ($d_{x^2-y^2}, d_{3z^2-r^2}$) extending to the oxygen ion direction owing to crystal field created by oxygen ions. The valence of a Mn ion is 3+ in $LaMnO_3$, which means that there are four 3*d* electron spins in a Mn ion. Following Hund's rule, three Mn spins (S=3/2) occupy the t_{2g} orbital, and the remaining one (S=1/2) is placed at the e_g orbital. The t_{2g} orbital is energetically placed at a deep position, and the band gap is small because there is little hybridization with the 2*p* orbital of the oxygen ion so that the t_{2g} orbital forms a localized spin S = 3/2. In contrast, the e_g orbital is strongly hybridized with the 2*p* orbital of the oxygen ion, and it is considered that the Mn spin in the e_g orbital plays a crucial role in the electric and magnetic properties of RMnO$_3$. In RMnO$_3$ such as LaMnO$_3$, the e_g electrons occupy $[d_{x^2-y^2}/d_{3z^2-r^2}]$ orbitals staggeredly within the *ab* plane, i.e., orbital order, which originates from the corporative JT effect [see Fig. 1.7]. In the *ab*-plane, the e_g orbitals are elongated into the oxygen direction and hybridized to the $2p$-σ orbital of oxygen ions, whereas, in the *c* axis direction, the t_{2g} orbitals are mixed to the $2p$-π orbital of oxygen ions. Below the AF ordering temperature $T_N = 150$ K for LaMnO$_3$, since in the *ab* plane the nearest-neighbor e_g orbitals cross at right angles to each other, Mn spins are aligned ferromagnetically through super-exchange interactions via oxygen $2p$-σ orbital, while in the *c* axis direction (direction between planes), they are aligned anti-ferromagnetically due to the antiferromagnetic superexchange interaction between t_{2g} through the oxygen $2p$-π orbitals [42,43]. Figure 1.7 schematically draws the A-type AF order whose spin ordered configuration is ferromagnetic within the *ab* plane but antiferromagnetic along the *c* axis.

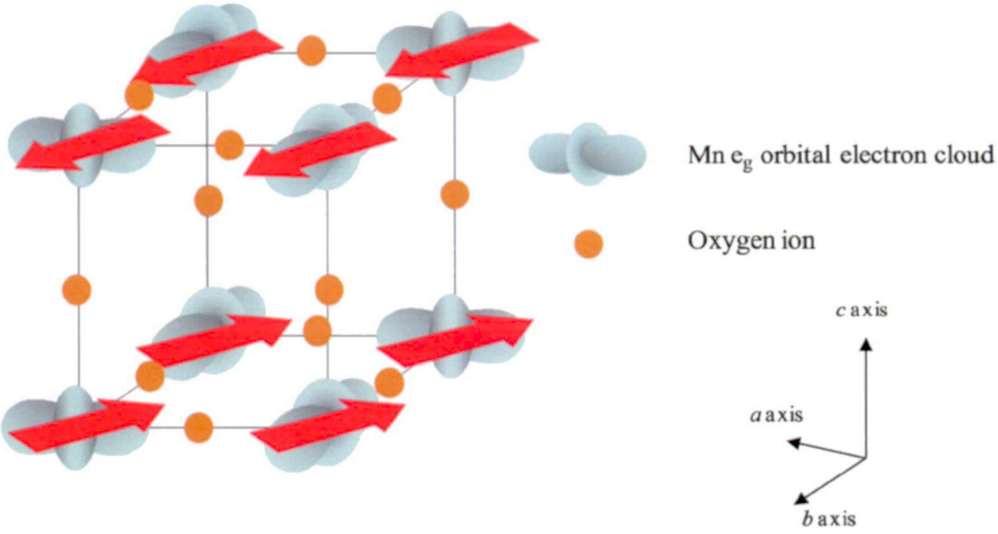

Figure 1.7. e_g orbital order and A-type AF structure in RMnO$_3$.

1.2.3. Weakly canted ferromagnetism [44]

Spin canting and the resultant weak ferromagnetism (FM) along the *c* axis is generally accompanied by the A-type AF order in $R\mathrm{MnO}_3$ with large r_R. The origin of the weak FM has been discussed in terms of the single-ion anisotropy and the DM interaction [45]. In this thesis, we focus on the asymmetric DM interaction to explain the weak FM.

This interaction does not have the form $(\boldsymbol{S}_1 \cdot \boldsymbol{S}_2)$ but rather $[\boldsymbol{S}_1 \times \boldsymbol{S}_2]$ between two spins, $\boldsymbol{S}_1$ and $\boldsymbol{S}_2$. It was first proposed by Dzyaloshinskii [46] phenomenologically that the interaction between two spins can be induced by the introduction of crystal symmetry and symmetrical operation of spin (time) reversal. Later, Moriya [47] microscopically explained this interaction by speculation on magnetic bond and crystal symmetry to a non-degenerate ground state. This interaction causes weak ferromagnetism with an antiferromagnetic spin arrangement which is shown in α-$\mathrm{Fe}_2\mathrm{O}_3$ and so on. This system can be expressed in terms of the free energy of spin variables (magnetic moments) by

$$\varepsilon_{\mathrm{ex.DM}} = \boldsymbol{D} \cdot (\boldsymbol{S}_1 \times \boldsymbol{S}_2), \tag{1.10}$$

where $\boldsymbol{D}$ is the DM vector. The magnitude of $\boldsymbol{D}$ is calculated by:

$$|D| \cong \frac{\lambda J}{\Delta E} \sim \frac{\Delta g}{g} J \ , \tag{1.11}$$

where λ is the spin-orbit interaction constant. The interaction energy of $\boldsymbol{D} \cdot (\boldsymbol{S}_1 \times \boldsymbol{S}_2)$ reaches minimum, when the $(\boldsymbol{S}_1 \times \boldsymbol{S}_2)$ vector is inverse to the $\boldsymbol{D}$ vector direction, and the two spins ($\boldsymbol{S}_1$ and $\boldsymbol{S}_2$) in in-plane perpendicular to $\boldsymbol{D}$ form a right angle (90 degrees). This type of interaction barely exists alone, although it affects spin configurations coexisting with different interactions. When considering the coexistence of the interaction between two spins ($\boldsymbol{S}_1$ and $\boldsymbol{S}_2$) and an antiferromagnetic Heisenberg interaction, (the nearest neighbor interaction, $J_1 < 0$), the coupling energy can be expressed by:

$$E(\theta) = -2|J_1|S^2 \cos\theta - DS^2 \sin\theta \qquad (|\boldsymbol{D}| = D), \tag{1.12}$$

under the assumption that $|\boldsymbol{S}_1| = |\boldsymbol{S}_2| = S$, and the angle formed by two spins, $(\pi - \theta)$. The θ which minimizes the coupling energy will be calculated as follows:

$$\tan\theta = \frac{D}{2|J_1|} \tag{1.13}$$

Namely, canted antiferromagnetism sharing ferromagnetic components with the coupled two spins forming an angle emerges. When $2|J_1| \gg D$, weak ferromagnetism appears as displayed in Fig. 1.8. Additionally, when J_2 (the next nearest neighbor interaction) works in the direction of two coupling atoms, as in case of $J_2 > 0$, canted antiferromagnetism emerges. However, in the case of $J_2 \lesssim 0$ and $|J_2| < D$, there is a stable spiral spin structure in which the θ of the Eq. (1.12) is caused by the D. Thus, asymmetric interaction can also be the origin of the spiral spin structure. Figure 1.9 displays the weak ferromagnetism in $LaMnO_3$ only along the *c* axis.

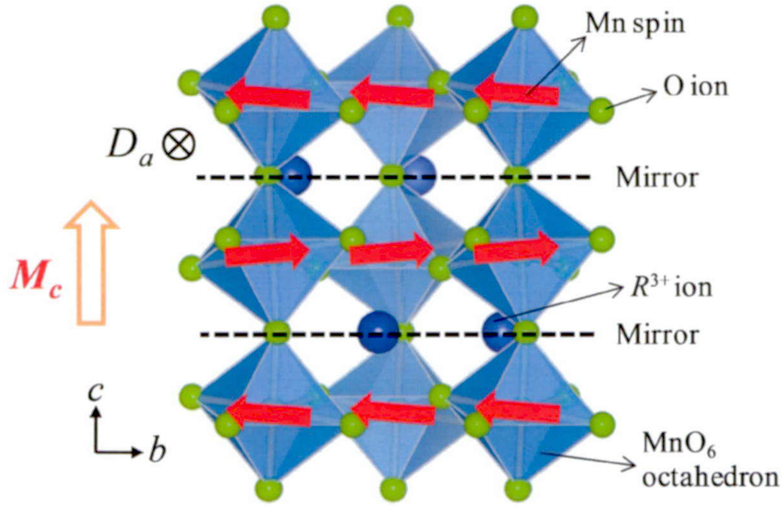

Figure 1.8. Weakly canted FM in terms of asymmetric DM interaction in $R\text{MnO}_3$ system.

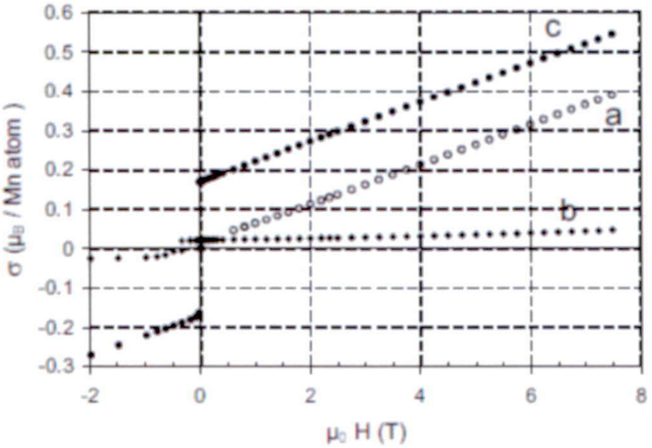

Figure 1.9. Magnetization curves at 20 K for a single crystal of LaMnO_3 along the three orthorhombic axes. It is seen that the weak moment (FM) is directed along only *c* [45].

1.3. Néel *N*-type ferrimagnet

In this section, the *N*-type ferrimagnet is shortly introduced as it was part of the discovery of the new magnetodielectric effect in $SmMnO_3$.

A ferrimagnet is defined as a material in which two or more magnetic moments of the atoms on different sublattices are aligned antiferromagnetically [see Fig. 1.10(a)]. However, the magnetic moments are not equal so a spontaneous magnetization can remain. Ferrimagnetism can be observed in some ferrites, magnetic garnets, and so on. In 1948, Lois Néel [48] classified ferrimagnetism into several types: Q-, R-, P-..., as illustrated in Fig. 1.10(b). Among them, the *N*-type ferrimagnet is unique. This is because it shows negative magnetization below a certain temperature (compensation temperature T_{comp}) which is lower than T_N. However, as temperature decreases, the magnetization is suppressed and then disappears at the compensation temperature. As the temperature continues to decrease, the magnetization becomes negative when an applied magnetic field is relatively small. This evolution is due to the change in the sum of the two opposite moments caused by the temperature. At the compensation temperature, the magnitude of the two opposite moments becomes equal. Then, the magnetization becomes negative below the compensation temperature because the magnitude of the moment which is aligned antiparallel to the applied weak magnetic field direction is larger than that of the other moment due to their antiferromagnetic interaction. However, when a strong magnetic field is applied, the magnetization suddenly increases below the compensation temperature as seen in Fig. 1.10(b). This feature observed in the Néel *N*-type ferrimagnet reemerges in $SmMnO_3$. Results of magnetic field effects on magnetization coupled with dielectric properties for $SmMnO_3$ are introduced in Chapter 3.

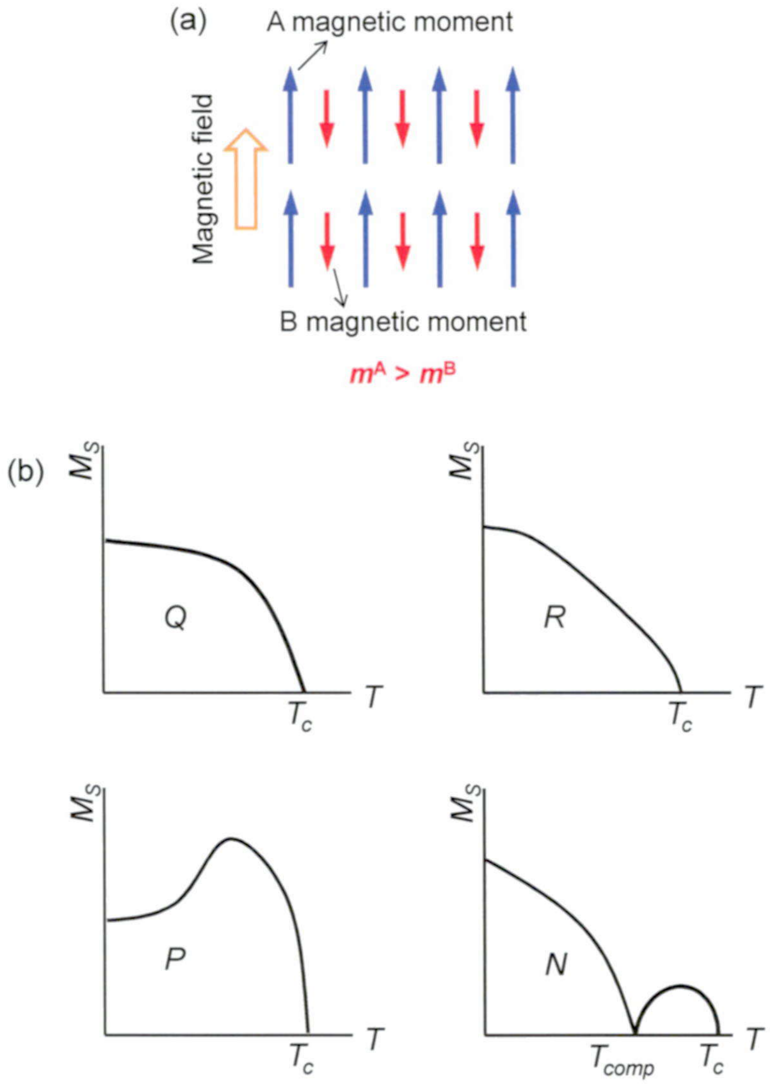

Figure 1.10. Ferrimagnetic alignment (a) and ferrimagnet types (b).

1.4. Physical properties of $SmMnO_3$

The ground state of $SmMnO_3$ is the A-type AF ordered state with the weak ferromagnetism along the *c* axis due to the asymmetric DM interaction. This is the same with $LaMnO_3$. However, T_N of $SmMnO_3$ is 60 K which is much lower than that of $LaMnO_3$ (T_N = 140 K). Furthermore, $SmMnO_3$ can be viewed as ferrimagnetic because it consists of two magnetic moments, Sm and Mn ones, which are strongly antiparallel to each other. This characteristic contributes significantly to physical properties in $SmMnO_3$.

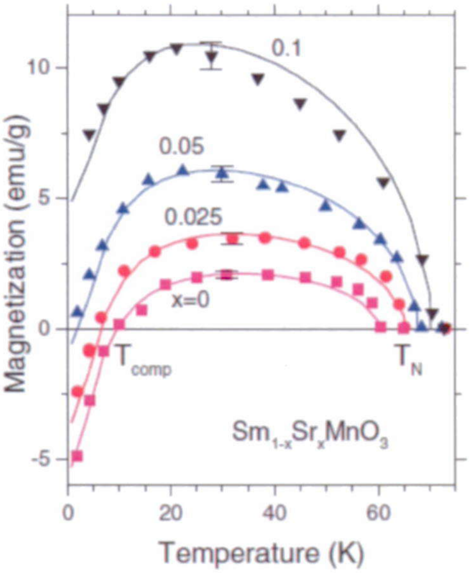

Figure 1.11. Temperature dependence of the spontaneous magnetization for $Sm_{1-x}Sr_xMnO_3$ crystals: experiment (points), and theory (solid lines) [49].

Previously, magnetic properties of $Sm_{1-x}Sr_xMnO_3$ single crystals were investigated by Ivanov and coworkers [49]. They reported that a compensation point of spontaneous magnetization along the *c* axis (in the *Pbnm* setting) was observed at $T_{comp} \approx 9$ K for a pure untwined $SmMnO_3$, as seen in Fig. 1.11. Below T_{comp}, unusual behavior appeared, and the magnetization showed negative values in spite of a positive magnetic field being applied.

They observed that it originates from an antiparallel orientation of the Mn weak ferromagnetic moment and of the Sm moment induced by Sm-Mn exchange interactions [48]. They calculated the temperature dependence of the spontaneous magnetization for $SmMnO_3$ along the easy axis taking into account the ground Sm^{3+} Kramers doublet characterized by a splitting due to the Sm-Mn exchange, $\Delta_{ex} \approx 6\ cm^{-1}$, and by the Sm^{3+} magnetic moment $\mu_c \approx 0.4\mu_B$ [49]. A more detailed explanation of behaviors such as the observed compensation point and the negative magnetization measured at a relatively weak magnetic field for $SmMnO_3$ will be introduced in chapter 3 with speculated magnetic configurations.

1.5. Motivation of this work

As mentioned before, magnetodielectrics, which possess neither multiferroics nor magnetoelectric effect, should attract more attention for their potential applications, and to better understand the origin of the magnetoelectric effect. In magnetodielectrics, several signs can be seen: an anomaly of the dielectric constant at magnetic ordering temperature and a finite magnetic field dependence of the dielectric constant, namely, magnetocapacitance. In this thesis, therefore, we aim to investigate the magnetocapacitive effect of $SmMnO_3$ with (1) A-type antiferromagnetic ordering, (2) paraelectric behavior, and (3) complex magnetic structure (*N*-type ferrimagnet). It is expected that we will discover a new, strong dielectric and magnetic coupling, that is, a new magnetodielectric type. Another purpose in this study is to clarify origin of the magnetodielectric effect.

In short, the goals of this thesis are as follows:

1. The discovery of magnetic field effects on dielectric and magnetic properties to A-type AF and ferrimagnetic $SmMnO_3$.
2. The development of approaches to resolve the origin of dielectric dispersion in RMnO$_3$.
3. The understanding significant lattice distortion induced by change in magnetic configurations.
4. The clarification of complex magnetic states between Sm-Mn moments to understand the microscopic origin of magnetocapacitive effect in $SmMnO_3$.

We performed macroscopic and microscopic measurements to achieve these goals.

1.6. An outline of this thesis

This thesis consists of the following contents. In the next chapter, single crystal growth and the various measurement techniques we used for this study, such as the floating zone method, dielectric constant and magnetization measurements, strain gauge measurement, and hard and soft x-ray magnetic circular dichroism (XMCD) measurements, respectively, are explained explicitly. In chapter 3, we display the results of various magnetic field effects on dielectric and magnetic properties for single crystals of $SmMnO_3$ and of hard XMCD for polycrystalline $SmMnO_3$. We state that large and new magnetocapacitive effects are observed in this material and are attributed to a change in magnetic moment configurations. In chapter 4, we show results of magnetostrictive effects coupled with magnetic ordering and configurations, and discuss them in terms of orbital occupancy change. In chapter 5, we present soft XMCD results of the Sm 4*f* and Mn 3*d* ions to get a clue to solve the microscopic origin of the magnetocapacitive effect. Finally, we summarize this thesis in chapter 6.

Bibliography for Chapter 1

[1]T. Kimura, T. Goto, H. Shintani, K. Ishizaka, T. Arima, and Y. Tokura, Nature **426**, 55-58 (2003).

[2]H. Schumid, "Magnetoelectric effects in insulating materials", *In Introduction to Complex Mediums for Optics and Electromagnetics*. eds. W. S. Weiglhoger and A. Lakhtakia (Bellingham, WA: SPIE Press) pp. 167-95 (2003).

[3]M. Fiebig, J. Phys. D: Appl. Phys. **38**, R123-R152 (2005).

[4]Y. Kitagawa, Y. Hiraoka, T. Honda, T. Ishikura, H. Nakamura, and T. Kimura, Nature Materials **9**, 797-802 (2010).

[5]G. Lawes, T. Kimura, C. M. Varma, M. A. Subramanian, N. Rogado, R. J. Cava, and A. P. Ramirez, Prog. Sol. Sta. Chem. **37**, 40-54 (2009).

[6]P. Curie, J. Phys. **3** (Ser. III): 393-415, (1984).

[7]T. H. O'Dell, *The Electrodynamics of Magneto-Electric Media*. Amsterdam: North-Holland (1970).

[8]A. J. Freeman and H. Schmid, eds., *Magnetoelectric Interaction Phenomena in Crystals*. London: Gordon & Breach (1975).

[9]I. E. Dzyaloshinskii, Sov. Phys. JETP **10**, 628–629 (1960).

[10]D. N. Astrov, Sov. Phys. JETP **11**, 708 (1960).

[11]V. E. Wood and A. E. Austin, Int. J. Magn. **5**, 303-315 (1974).

[12]J. P. Rivera, Ferroelectrics **161**, 147 (1993).

[13]B. B. Krichevtsov, V. V. Pavlov, and R. V. Pisarev, JETP lett. **49**, 535 (1989).

[14]G. T. Rado, J. M. Ferrari, and S. Shtrikman, Phys. Rev. B **29**, 4041 (1984).

[15]W. F. Brown, R. M. Hornreich, and S. Shtrikman, Phys. Rev. 168, 574 (1968).

[16]D. I. Khomskii, J. Magn. Magn. Mater. **306**, 1-8 (2006).

[17]W. Eerenstein, N. D. Murther, and J. F. Scott, Nature **442**, 759-65 (2006).

[18]E. Ascher, H. Rieder, H. Schmid, and Stössel, J. Appl. Phys. **37**, 1404 (1966).

[19]D. L. Fox, D. R. Tilley, J. F. Scott, and H. J. Guggenheim, Phys. Rev. B **21**, 2926 (1980).

[20] G. A. Smolenskii and V. A. Bokov, J. Appl. Phys. **35**, 915 (1964).

[21] Z. J. Huang, Y. Cao, Y. Y. Sun, Y. Y. Xue, and C. W. Chu, Phys. Rev. B **56**, 2623 (1997).

[22] J. Wang, J. B. Neaton, H. Zheng, V. Nagarajan, S. B. Ogale, B. Liu, D. Viehland, V. Vaithyanathan, D. G. Schlom, U. V. Waghmare, N. A. Spaldin, K. M. Rabe, M. Wuttig, and R. Ramesh, Science **299**, 1719 (2003).

[23] T. Goto, T. Kimura, G. Lawes, A. P. Ramirez, and Y. Tokura, Phys. Rev. Lett. **92**, 257201 (2004).

[24] T. Kimura, Annu. Rev. Mater. Res. **37**, 387-413 (2007).

[25] M. Kenzelmann, A. B. Harris, S. Jonas, C. Broholm, J. Schefer, S. B. Kim, C. L. Zhang, S.-W. Cheong, O. P. Vajk, and J.W. Lynn, Phys. Rev. Lett. **95**, 087206 (2005).

[26] M. Mostovoy, Phys. Rev. Lett. **96**, 067601 (2006).

[27] T. Arima, T. Goto, Y. Yamasaki, S. Miyasaka, K. Ishii, M. Tsubota, T. Inami, Y. Murakami, and Y. Tokura, Phys. Rev. B **72**, 100102 (2005).

[28] H. Katsura, N. Nagaosa, and A. V. Balatsky, Phys. Rev. Lett **95**, 057205 (2005).

[29] I. A. Sergienko and E. Dagotto, Phys. Rev. B **73**, 094434 (2006).

[30] U. Adem, "*Magnetodielectric Coupling in Multiferroic Transition Metal Oxides*" Ph. D. thesis, University of Groningen (2008).

[31] G. Lawes, A. P. Ramirez, C. M. Varma, and M. A. Subramanian, Phys. Rev. Lett. **91**, 257208 (2003).

[32] M. S. Seehra and R. E. Helmick, Phys. Rev. B **24**, 5068 (1981).

[33] M. S. Seehra and R. E. Helmick, J. Appl. Phys. **55**, 2330 (1984).

[34] R. Muralidharan, T. –H. Jang, C. –H. Yang, Y. H. Jeong, and T. Y. Koo, Appl. Phys. Lett. **90**, 012506 (2007).

[35] N. Hur, S. Park, S. Guha, A. Borissov, V. Kiryukhin, and S. –W. Cheong, Appl. Phys. Lett. **87**, 042901 (2005).

[36] G. A. Smolenskii and I. E. Chupis, Sov. Phys. Usp. **25**, 475 (1982).

[37] T. Kimura, S. Kawamoto, I. Yamada, M. Azuma, M. Takano, and Y. Tokura, Phys. Rev. B 67, 180401(R) (2003).

[38] T. Kimura, S. Ishihara, H. Shintani, T. Arima, K. T. Takahashi, K. Ishizaka, and Y. Tokura, Phys. Rev. B 68, 060403(R) (2003).

[39] J. Rodríguez-Carvajal, M. Hennion, F. Moussa, and A. H. Moudden, Phys. Rev. B **57**, 3189(R) (1998).

[40] I. A. Sergienko, C. Sen, and E. Dagotto, Phys. Rev. Lett. **97**, 227204 (2006).

[41] V. Y. Pomajakushin, M. Kenzelmann, A. Doenni, A. B. Harris, T. Nakajima, S. Mitsuda, M. Tachibana, L. Keller, J. Mesot, H. Kitazawa, E. Takayama-Muromachi, New. J. Phys. **11**, 043019 (2009).

[42] I.Solovyev, N.Hamada, and K.Terakura, Phys.Rev. Lett **76**, 4825 (1996).

[43] K.Hirota, N.Kaneko, A.Nishizawa, and Y. Endoh, J.Phys. Soc. Jpn. **65**, 3736 (1996).

[44] K. Adachi, Magnetism of compounds – Localised spin system (1996).

[45] V. Skumryev, F. Ott, J. M. D. Coey, A. Anane, J. -P. Renard, L. Pinsard-Gaudart, and A. Revcolevschi, Eur. Phys. J. B **11**, 401 (1999).

[46] I. Dzyaloshinsky, J. Phys. Chem. Solids **4**, 241 (1958).

[47] T. Moriya, Phys. Rev. **120**, 91 (1960).

[48] L. Néel, Ann. Phys. (Paris) **3**, 137 (1948).

[49] V. Y. Ivanov, A. A. Mukhin, A. S. Prokhorov, and A. M. Balbashov, Phys. Stat. Sol. (b) **236**, 445 (2003).

Chapter 2.

Experimental methods

2.1. Single crystal growth

Single crystals of $SmMnO_3$ used for measurements of magnetization, dielectric constant, strain, and soft x-ray magnetic circular dichroism were grown by the floating zone (FZ) method. The procedures to grow the single crystals are as follows (see Fig. 2.1).

(1) Powders of Sm_2O_3 and Mn_3O_4 with 99.9 % purity (purchased from Kojundo Chemical Laboratory Co., Ltd.), were weighed in the desired ratio and well mixed in acetone. The powders were dried in the air, and then, were pre-heated to 1200°C for 24 hours in an air atmosphere for solid state reaction.

(2) The solid state reacted powders were mixed again and put into a rubber balloon. The balloon was hydrostatically pressed under a pressure of 45 MPa for 2 minutes to make a rod (6 mm in diameter and 120 mm in length).

(3) The hydrostatically pressed polycrystalline rods were heated again at 1350°C for 30 hours in the air atmosphere.

(4) Upper and lower rods were set in a single crystal growth apparatus (D-1, Cannon Machinery) and the rods were melted (floating zone state) by focused infrared light produced by double ellipsoidal reflectors and two halogen lamps. Single crystals were fabricated by transferring the two rods downward at 3mm/h in flowing N_2.

Portions of the obtained single crystals were crushed into powders and characterized by powder x-ray diffraction (XRD) measurements to have a single phase of the *Pbnm* orthorhombic structure. The grown crystals were oriented through Laue XRD patterns, and cut into rectangular shaped specimens with the widest faces perpendicular to the crystallographic principal axes for the various measurements.

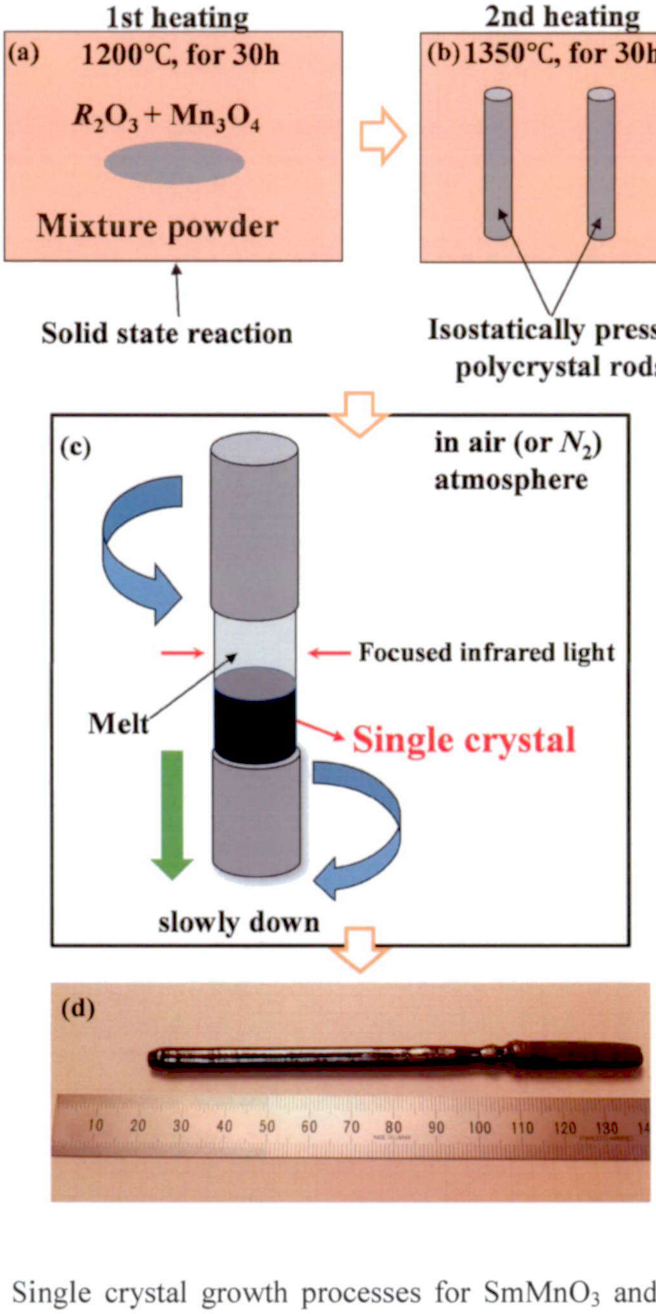

Figure 2.1. (a-c) Single crystal growth processes for $SmMnO_3$ and (d) the grown single crystal by means of the FZ method

2.2. Dielectric constant measurement

In this study, we carried out capacitance measurement to get the dielectric constant we need. For this measurement, silver electrodes were vacuum deposited on the opposite faces (the *c* plane here) which were polished. Figure 2.2 shows the schematics of the prepared sample with the electrode, and of the wiring setup for the four-terminal measurement which connects Cu lead wires from the sample with coaxial cables for the measurement of dielectric constant. For this, AC electric field E_c and magnetic fields B_c were applied along *c*. A more detailed introduction of this measurement follows.

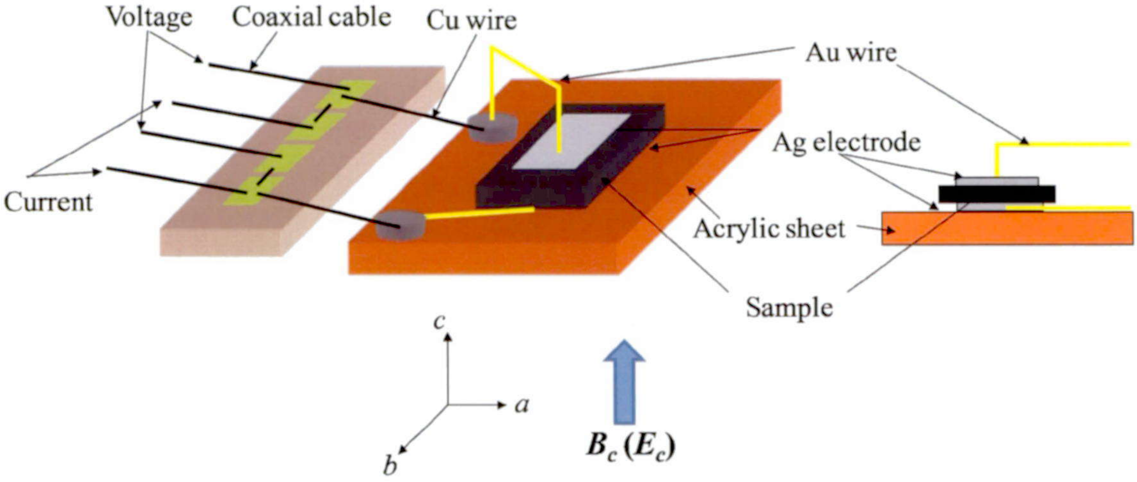

Figure 2.2. Schematic illustrations of the prepared sample and of the wiring setup for the four-terminal measurement for dielectric constant.

Dielectric constant (Capacitance)

Dielectric constant is one of the important parameters which reflect the response of a material to external electric fields. Since the dielectric constant is frequency dependent, a proper technique is used for the measurement. In this study, we used a range of low frequency from 1 to 200 kHz belonging to a dipole moment range in dielectric constant using a capacitance method.

Figure 2.3 displays a schematic illustration of a capacitor structure, where an insulator sample is covered with conducting electrodes on both surfaces. Capacitance C is expressed as $C = Q/V$, where Q is the charge on the electrodes and V is the electric potential between the electrodes. C can be obtained by:

$$C = \varepsilon \frac{A}{d}, \tag{2.1}$$

and

$$\varepsilon_r = \frac{Cd}{\varepsilon_0 A} \quad (\text{from } \frac{\varepsilon}{\varepsilon_0} = \varepsilon_r), \tag{2.2}$$

where ε is the dielectric constant, A is the area of electrodes, d is thickness of the sample, ε_r is relative dielectric constant, and ε_0 is the dielectric constant of the vacuum (ε_0=8.855×10^{-12}F/m). Thus, by measuring C, one can obtain dielectric constant ε or relative dielectric constant ε_r.

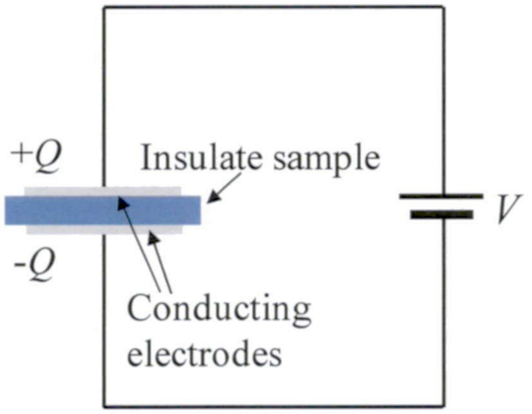

Figure 2.3. A schematic illustration for the capacitance measurement.

A precision LCR meter (Agilent E4980A) was used for this measurement with a wide frequency range (1~200 kHz). The AC voltage was set to be 1 V. For observation of magnetic field effects on the dielectric constant, we used a superconducting magnet (Oxford, up to 8 T) and the Physical Properties Measurement System (Quantum Design PPMS, up to 9 T).

2.3. Magnetization measurement

To obtain magnetic information, we measured magnetization by means of a commercial PPMS (up to 9 T) and the Vibrating Sample Magnetometry (VSM-SQUID, Quantum Design, up to 7 T). We used these apparatuses to measure the magnetization as functions of temperature and magnetic field. For these measurements, magnetic fields were applied only along the *c* axis.

Figure 2.4. A picture of the VSM-SQUID

2.4. Strain gauge measurement

In this section, we introduce the strain gauge measurement. For explanation of the strain gauge measurement technique, we refer to the Ph.D. thesis of Dr. K. Kimura (Osaka University) [1].

Strain gauge measurement was performed to study the striction ($\Delta L/L$) of temperature and magnetic field profiles for $SmMnO_3$. We briefly state the principle of the method. The strain gauge is a sensor which can detect a small mechanical change of sample length as an electric signal. Figure 2.5(a) shows the setup of a strain gauge and dummy (Cu) for the measurement. The strain gauge is tightly attached to a sample so that the sensing element (metallic resistive foil) elongates or contracts from the strain induced by the sample as seen in Fig. 2.5(b). When the gauge elongates or contracts, the sensing element undergoes a change in electric resistance (R) from Eq. (2.3):

$$\frac{\Delta R}{R} = G\frac{\Delta L}{L}, \tag{2.3}$$

where $\Delta R/R$ is a relative change of gauge resistance, and G is a temperature-dependent proportional constant (called as gauge factor).

A bridge circuit for this measurement is used for high resolution. We measure the changes in voltage converted from those in resistance. There are various types of the circuits depending on the situation. Here, we used the active-dummy method to reduce the temperature-dependent resistance of lead wire and of the magnetoresistant component of the gauges which affect obtained data. A home-built bridge circuit [1] for the active-dummy method, in which a non-magnetic Cu-plate as dummy material, is also shown in Fig. 2.5(a), where E_{IN} and E_{OUT} are input and output voltage, respectively. With appropriate approximation, $\Delta L/L$ is expressed as:

$$\frac{\Delta L}{L} = \frac{\Delta L_C}{L_C} + \frac{4}{G}\frac{E_{OUT}}{E_{IN}} , \tag{2.4}$$

where $\Delta L_C/L_C$ is the striction of the dummy (Cu) part.

In this study, we measured magnetostriction $\Delta L / L$ of $SmMnO_3$ as functions of temperature with or without magnetic fields and of a magnetic field at various selected temperatures.

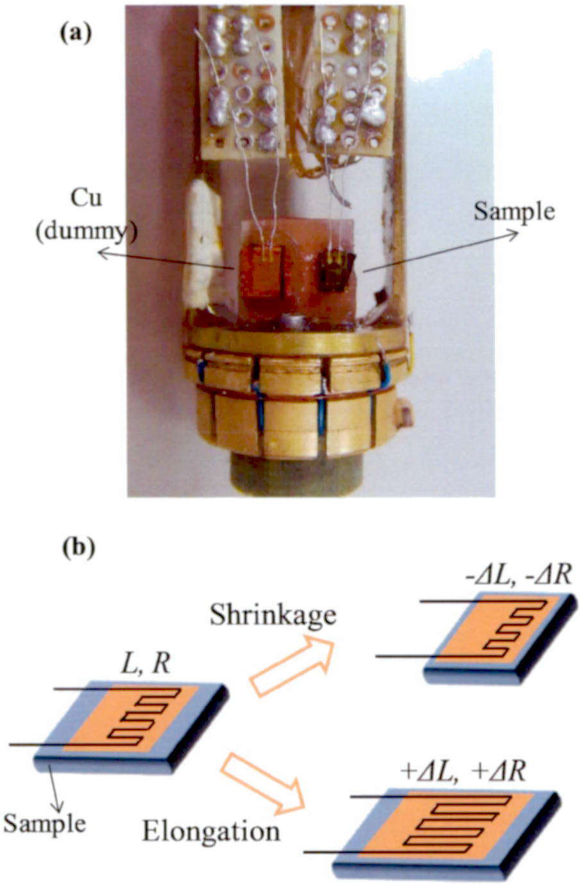

Figure 2.5. (a) A real set-up sample picture for the strain gauge measurement of the active-dummy (Cu) method. (b) Schematics of sample elongation or contraction corresponding to the change of the gauge length.

If we put the reference temperature and magnetic field into T_0 and B_0, respectively, $\Delta L/L$ at an arbitrary temperature (T) and magnetic field (B) is written as:

$$\frac{\Delta L(T,B)}{L(T_0,B_0)}=\frac{\Delta L_C(T,B)}{L_C(T_0,B_0)}+\frac{4}{G}\frac{E_{OUT}}{E_{IN}}=\frac{\Delta L_C(T)}{L_C(T_0)}+\frac{4}{G}\frac{E_{OUT}}{E_{IN}}, \qquad (2.5)$$

A Cu plate was used as the dummy in this measurement, as it does not show magnetostriction. $\Delta L_C(T)/L_C(T_0)$ is the thermal expansion of the Cu plate and can be obtained by the data calculation [2]. Therefore, we can observe the striction $\Delta L(T, B)/L_C(T_0, B_0)$ of our sample through the determined E_{IN} and measured E_{OUT}. And since G data are given to 77 K in Ref. [2], we obtained the G values below 77 K by extrapolation.

The strain gauge measurement was carried out through PPMS. The commercial strain gauge (KYOWA, KFL-1-120-C1-11 type) was bonded onto a polished sample and Cu-plate surfaces by using adhesive gauge cement (KYOWA, PC-6). To apply E_{IN} and to measure E_{OUT}, a voltage generator (ADCMT 6144) and a multimeter (Keithley 2000) were used, respectively. Note that suitable parallel alignment of the gauges between the active (sample) and dummy (Cu) is required for reduction of the magnetoresistant component.

2.5. Hard and soft x-ray Magnetic Circular Dichroism (XMCD) techniques

In this section, we briefly introduce the XMCD technique, a powerful method for investigating element specific magnetization, using hard and soft x-rays for the Sm and Mn moments of $SmMnO_3$. Because, in principle, the fundamentals of XMCD are similar regardless of hard and soft x-rays performed at BL39XU (see Fig. 2.5) and BL25SU of SPring-8, respectively, we concentrate on an explanation of the soft XMCD technique in this section. We refer to textbooks [3, 4] for taking into account for it.

The principle of the XMCD effect can be explained easily with the so-called *two-step* model proposed by G. Schütz et al. [5] and later by J. Stöhr et al. [6]. The first step is the excitation of a core electron by a circularly polarized x-ray photon that carries an angular momentum [right handed photon $+\hbar$ (= +1) and left handed photon $-\hbar$ (= -1)] coincident with helicity vector parallel (right) or antiparallel (left) to the direction of propagation. Owing to the conservation of angular momentum in the absorption process, the angular momentum carried by the photon is entirely transferred to the excited photoelectron. Both the orbital (l) and spin (s) moments of the photoelectron are affected by this momentum transfer dependent on the initial core state and on the nature of interactions. Let us consider this process with an example, a photoelectron excited from spin-orbit-split core levels of L_2 ($2p_{1/2} \rightarrow 3d$) and L_3 ($2p_{3/2} \rightarrow 3d$) absorption edges in $3d$ shell transition as displayed in Fig. 2.5(a). Then, part of the angular momentum carried by the photon will be changed into the spin moment via a spin-orbit interaction known as the Fano effect [7]. The spin moment of the photoelectron is always parallel to the direction of propagation of the photon. However, its sign is determined by the helicity of the incident x-ray photon and by the spin-orbit interaction, such as $l + s$ at the L_3 edge and $l - s$ at the L_2 edge. Note that in the absence of the spin-orbit coupling, the angular momentum of the photon is entirely converted into $+\hbar$ (or $-\hbar$) orbital moments, and there cannot be any polarization of the photoelectron. Namely, no asymmetric XMCD signal appears.

The second step is derived from magnetic properties of the sample. X-ray absorption spectra (XAS) basically reflect the density of empty states for an angular momentum l depending on the symmetry of the initial core state and on selection rules of the transition.

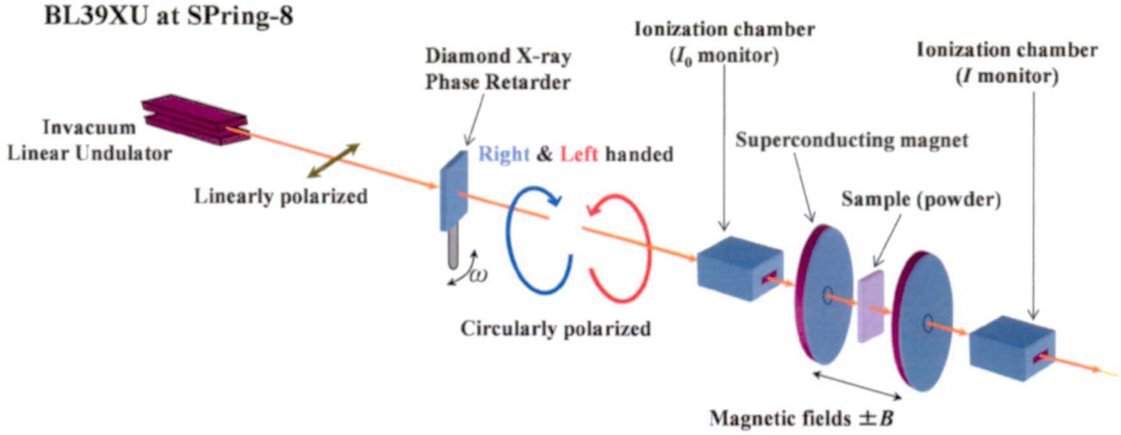

Figure 2.5. A simple illustration for hard XMCD measurement set-up for powder transmission mode by using the helicity-modulation technique performed at BL39XL in SPring-8.

XMCD spectra simply reflect the difference in the density of states with a different spin or orbital moment, which takes advantage of the *relative transition probability* [see Fig. 2.6(a). In the case of spin-orbit split initial states, the excited photoelectron carries both a spin and an orbital momentum, and any imbalance in either spin or orbital momentum in the final states will immediately give rise to a dichroic effect [3]. Thus, the XMCD signal is obtained from the difference of the XAS intensity detected between right and left handed polarized photoelectrons or by between positive and negative magnetic fields. Thus, the XMCD signal can be written as:

$$XMCD = I^{+(R)} - I^{-(L)} = I^{+B} - I^{-B}, \tag{2.6}$$

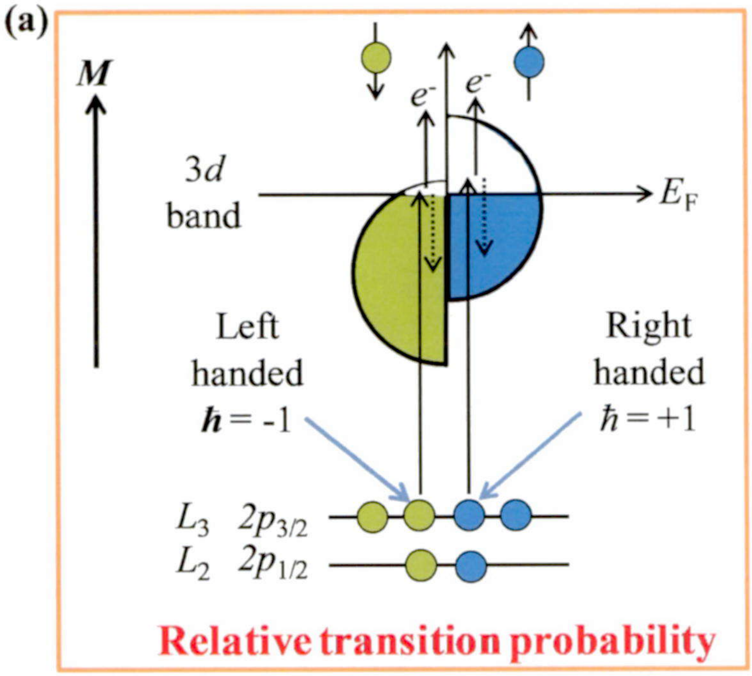

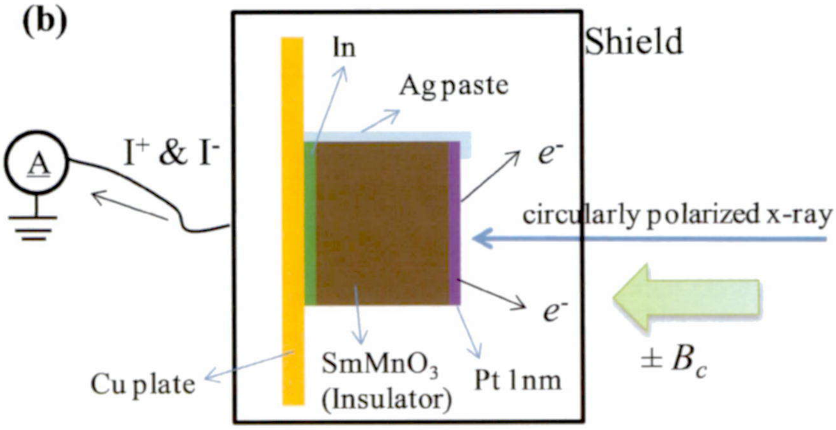

Figure 2.6. (a) Illustration of XMCD principle for *L*-edge absorption with density of spin-up and spin-down states. (b) Schematics of total electron yield method performed at BL25SU of SPring-8 for this study.

The advantage of the soft XMCD method is that it makes possible the direct observation of the magnetic states of 3*d* transition metals ($L_{2,3}$ absorption edges) and of 4*f* rare earths ($M_{4,5}$ absorption edges), which determine their magnetic properties. Furthermore, the magneto-optical sum rule originally derived by B. T. Thole et al. and P. Carra et al. [8, 9] for the absorption edges provides their quantitative values of the spin magnetic moment $(m_S = -2\mu_B\hbar\langle S_z\rangle)$ and of the orbital magnetic moment $(m_L = -\mu_B\hbar\langle L_z\rangle)$, and of the resultant total magnetic moment from soft XMCD results, respectively. The derived sum rule of orbital m_L and spin m_S moments of transition metal, for example, an Mn ion, is given respectively as

$$m_L^{Mn} = -\frac{4}{3}\frac{\Delta A_{L_3} + \Delta A_{L_2}}{A_{L_3} + A_{L_2}} n_h \cdot \mu_B \ , \tag{2.7}$$

$$m_S^{Mn} = -\sum_{\alpha=x,y,z} \frac{(2\Delta A_{L_3} - 4\Delta A_{L_2})_\alpha}{3(A_{L_3} + A_{L_2})} n_h \cdot \mu_B \ , \tag{2.8}$$

, where $n_h = 10 - n_{3d}$ with n_{3d} being the 3*d* electron occupation number, ΔA_{L_3} and ΔA_{L_2}, A_{L_3} and A_{L_2} are the L_3 and L_2 integrated XMCD and XAS sum intensities, respectively. Since the bare spin sum rule generally underestimates m_S, we used a correction factor given by the calculation [10, 11]. In addition, the sum rule of orbital $\langle M_{LZ}\rangle$ and spin $\langle M_{SZ}\rangle$ moments of rare earth elements, for example, a Sm ion, can be respectively given as

$$\langle m_{LZ}^{Sm}\rangle = -\langle L_Z\rangle\mu_B = 2n_h \frac{\Delta B_{M_5} + \Delta B_{M_4}}{B_{M_5} + B_{M_4}} \mu_B \ , \tag{2.9}$$

$$\langle m_{SZ}^{Sm}\rangle = -2\langle S_Z\rangle\mu_B = \left(2n_h \frac{\Delta B_{M_5} - \frac{3}{2}\Delta B_{M_4}}{B_{M_5} + B_{M_4}} + 6\langle T_Z\rangle \right)\mu_B \ , \tag{2.10}$$

where L_Z, S_Z, T_Z, and n_h are the orbital and spin angular momenta, magnetic dipole operator, and the number of holes in the 4*f* shell, respectively. And ΔB_{M_5} and ΔB_{M_4}, B_{M_5}, and B_{M_4} are the M_5 and M_4 integrated XMCD and XAS sum intensities in the 4*f* shell, respectively [12]. For rare-earth elements with a less-than-half filled 4*f* shell, the off-diagonal term of the 3*d*-4*f* exchange interaction causes a large amount of $3d_{5/2}$-$3d_{3/2}$ mixing, and the sum rule for m_S becomes invalid [13]. Ref.[13] defined a correction factor X_I/X_E to describe the effect of this mixing as follows:

$$X_I = -\frac{\Delta B_{M_5} - \frac{3}{2}\Delta B_{M_4}}{\frac{3}{2}(B_{M_5} + B_{M_4})}, \tag{2.11}$$

and

$$X_E = \frac{2}{3n}\langle S_Z \rangle + \frac{2}{n}\langle T_Z \rangle, \tag{2.12}$$

where X_I, X_E, and n are the integrated XMCD intensity related to the absorption, the expectation value, and the number of 4*f* electrons, respectively. For 3*d* electrons, $\langle T_Z \rangle$ can be regarded as zero for polycrystalline samples because of the decoupling between the quadrupolar charge distribution and magnetic spin orientation due to the small spin-orbit interaction. It is not necessary for $\langle T_Z \rangle$ to be considered [12]. On the other hand, for 4*f* electrons, the crystal field is weaker than the spin-orbit interaction, and $\langle T_Z \rangle$ is almost free from the crystal field and isotropic. Its value, therefore, for polycrystalline samples is about the same as that for free ions [12].

In this study, we investigated XAS and XMCD around Mn *K* and Sm $L_{2,3}$ edges for a powder sample of $SmMnO_3$ in transmission mode by using the helicity-modulation technique [14] with hard x-rays under various temperatures and magnetic fields. Then, we performed a soft XMCD measurement for Mn $L_{2,3}$ and Sm $M_{4,5}$ edges for single crystal $SmMnO_3$ in the total photoelectron yield mode [see Fig. 2.6(b)] to investigate the magnetic states in more detail.

Bibliography for Chapter 2

[1]K. Kimura, “Magnetoelectric Properties in a Geometrically-Frustrated Triangular Lattice Antiferromagnet $CuCrO_2$”, Ph. D. thesis, University of Osaka (2010).

[2]F. R. Kroeger and C. A. Swenson, J. Appl. Phys. **48**, 853 (1977).

[3]E. Beaurepaire, H. Bulou, F. Scheurer, and J.–P. Kappler (Eds.), Magnetism: A Synchrotron Radiation Approach, Lect. Notes Phys. **697** (Springer, Berlin Heidelberg) (2006).

[4]J. Stöhr and H. C. Siegmann, Magnetism: From Fundamentals to Nanoscale Dynamics, (Springer, Berlin Heidelberg) (2006).

[5]G. Schütz, W. Wagner, W. Wilhelm, P. Kienlm, P. Kienle, R. Zeller, R. Frahm, G. Materlik, Phys. Rev. Lett. **58**, 737 (1987).

[6]J. Stöhr and R. Nakajima, IBM J. Res. Develop. **42**, 73 (1998).

[7]U. Fano, Phys. Rev. **178**, 131 (1969).

[8]B. T. Thole, P. Carra, F. Sette, and g. van der Laan, Phys. Rev. Lett. **68**, 1943 (1992).

[9]P. Carra, H. König, B. T. Thole, and M. Altarelli, Physica B **192**, 182 (1993).

[10]Y. Teramura, A. Tanaka, and T. Jo, J. Phys. Soc. Jan. **65**, 1053 (1996).

[11]T. Koide, h. Miyauchi, J. Okamoto, T. Shidara, T. Sekine, T. Saitoh, A. Fujimori, H. Fukutani, M. Takano, and Y. Takeda, Phys. Rev. Lett. **87**, 246404 (2001).

[12]S. Qiao, A. Kimura, H. Adachi, K. Iori, K. Miyamoto, T. Xie, H. Namatame, M. Taniguchi, T. Muro, S. Imada, and S. Suga, Phys. Rev. B **70**, 134418 (2004).

[13]T. Jo, Electron Spectrosc. Relat. Phenom. **86**, 73 (1997).

[14]M. Suzuki, N. Kawamura, M. Mizumaki, A. Urata, H. Maruyama, S. Goto, and T. Ishikawa, Jpn. J. Apl. Phys., Part 2 **37**, L1488 (1998).

Chapter 3.

Large magnetodielectric effect in $SmMnO_3$

3.1. Introduction

The main purpose of this thesis is to investigate the correlation between magnetic and dielectric properties and to clarify the origin of the correlation of single crystals of $SmMnO_3$. In this chapter, magnetocapacitive effects were investigated for $SmMnO_3$ possessing a relatively large r_R and the A-type AF ground state of Mn moments. Although the backgrounds of this study and $SmMnO_3$ were mentioned in Chapter 1, we briefly present it again.

Recent discoveries of spin-driven ferroelectricity and gigantic magnetoelectric effects in some multiferroics have created considerable interest in terms of both basic and technological points of view [1, 2]. Among such multiferroics, ferroelectricity in perovskite manganites, RMnO$_3$ (R = rare-earth ions), with the *Pbnm* orthorhombic structure originates from a spiral [3, 4] or collinear E-type [5, 6] AF structure, breaking the inversion symmetry. These two magnetic structures are stabilized in RMnO$_3$ with intermediate (e.g., R = Tb and Dy) and small (e.g., R= Ho and Tm) ionic radii of the R ion r_R, respectively [7, 8]. On the other hand, the ground state of RMnO$_3$ with large r_R (e.g., R = La, Sm, and Eu) is the paraelectric A-type AF ordered phase in which Mn moments are aligned ferromagnetically within the *ab* plane but antiferromagnetically in the *c* direction [9]. More precisely, the A-type AF structure possesses a canted component along the *c* axis. The origin of the canting has been discussed in terms of the single-ion anisotropy and the Dzyaloshinskii-Moriya (DM) interaction [10]. With or without the ferroelectricity, most of the above-mentioned RMnO$_3$ show distinct dielectric dispersion at low temperatures only when an ac electric field is applied along the *c* axis [7, 11]. The origin of the dielectric dispersion remains an open question.

This manganite has never received attention mainly due to its lack of spin-driven ferroelectricity. However, $SmMnO_3$ shows distinct phenomena such as temperature-induced magnetization reversal and resultant negative magnetization opposite to the magnetic-field direction in a low magnetic field [12]. Such phenomena are observed in Néel *N*-type ferrimagnetic compounds [13], consisting of two or more magnetic sublattices (e.g., spinel ferrites [14]). In the case of $SmMnO_3$, the temperature-induced magnetization reversal and the negative magnetization are interpreted in connection with the canted Mn moments whose direction is the opposite of the polarized Sm moments [12]. Here, we report on dielectric anomalies coupled with the magnetization reversal induced by changes in temperature T and a magnetic field B for single crystals of $SmMnO_3$. It was found that the dielectric properties are dominated by relative configurations of the polarized Sm and the canted Mn moments with respect to the direction of B. We also report hard XMCD measurement results for proof of our suggestion concerning the simultaneous reversal, and peculiar cooling-field dependent asymmetric magnetocapacitance observed at T_{comp}. Furthermore, we present dielectric dispersion associated with relaxation time generally observed in rare earth manganites as well.

3.2. Experimental procedures

Single crystals of $SmMnO_3$ were grown by the floating-zone method. The crystals were oriented by using Laue x-ray diffraction patterns and were cut into rectangular plates with the widest faces perpendicular to the c axis. The magnetization along the c axis (M_c) was measured with commercial magnetometers, SQUID and VSM-SQUID. Real (ε'_c) and imaginary (ε''_c) parts of the dielectric constant along the c axis were measured using an LCR meter with the frequency f range from 1 to 200 kHz. Magnetic fields were applied only along the c axis. To obtain the element-specific information about the contribution to net magnetization, x-ray absorption (XAS) and x-ray magnetic circular dichroism (XMCD) spectra around Mn K and Sm $L_{2,3}$-edges were also measured for a powder sample crushed from a single crystal in transmission mode by using the helicity-modulation technique [15] on BL39XU at SPring-8.

3.3. Experimental results

3.3.1. Temperature dependent magnetization (M) and dielectric constant (ε')

Figures 3.1(a) and 3.1(b) show the T dependence of M_c and ε'_c, respectively. Prior to every in-field measurement, magnetic fields were applied at 80 K [field cooling (FC)]. First, we focus on the data at zero (or very weak) magnetic fields. As shown in the data at 0.01 T of Fig. 3.1(a), a steep rise of M_c is observed at $T_N = 60$ K, where the canted A-type AFM order of Mn moments arises. Upon cooling, M_c shows the maximum value of ~0.1 μ_B/f.u. around 30 K and starts to decrease gradually below ~30 K. As T decreases, it becomes zero at the compensation temperature $T_{\mathrm{comp}} = 9.4$ K and then becomes negative below T_{comp}. This T-induced magnetization reversal can be attributed to an antiparallel orientation between the canted Mn moment and the gradually polarized Sm moment induced by Sm-Mn exchange interactions [12]. Possible relative orientations between them above and below T_{comp} are schematically drawn in the insets of Fig. 3.1(a). Above T_{comp}, the vector sum of the canted Mn moments (M_{Mn}) is larger than the polarization of Sm moments (M_{Sm}). As T decreases, M_{Sm} grows rapidly and then exceeds M_{Mn} below Tcomp, which causes the negative magnetization. As seen in Fig. 3.1(b), at $B = 0$ T, no clear anomaly was observed in the T dependence of ε'_c at around T_{comp}.

Next, we focus on the data at $B \geq 2$ T. In contrast to the data at 0.01 T, the negative magnetization was not observed in M_c-T curves at $B \geq 2$ T [Fig. 3.1(a)]. Instead, M_c shows an abrupt increase at T_{jump} (just below T_{comp}) during the cooling process, and increases again as T decreases. The abrupt change at T_{jump} accompanies thermal hysteresis centered at T_{comp}, suggesting the existence of a first order phase transition. These behaviors are detected at all B above 1 T, but the hysteresis region gradually narrows down toward T_{comp} with increasing B. Corresponding to the abrupt changes in M_c around T_{comp}, ε'_c measured in high B shows a sudden drop at T_{jump} with a thermal hysteresis.

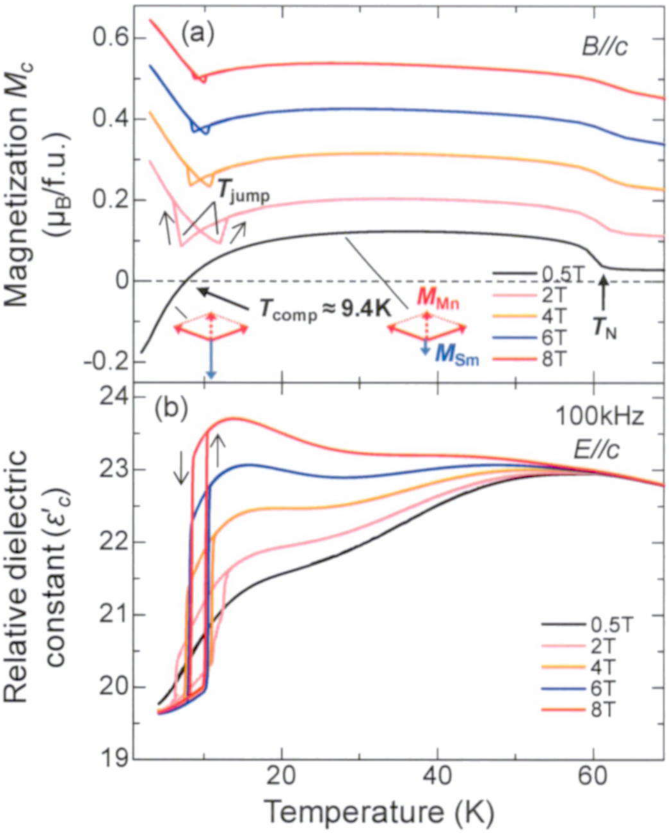

Figure 3.1. T profiles of (a) M_c and (b) ε'_c at selected B along c axis for single crystals of $SmMnO_3$. The inset of (a) depicts possible configurations of the polarized Sm and the canted Mn moments. Dashed arrows denote the vector sum of the canted Mn moments.

3.3.2. Magnetic field (B) dependent magnetization (M) and dielectric constant (ε')

To further examine the effects of B on M_c and ε'_c, we measured the isothermal magnetization M_c and magnetocapacitance $\{\Delta\varepsilon'_c(B)/\varepsilon'_c(0) = [\varepsilon'_c(B)-\varepsilon'_c(0)]/\varepsilon(0)\}$ as functions of B. Figures 3.2(a) and 3.2(b) display M_c-B curves measured at selected temperatures above and below T_{comp}, respectively. At 70 K (> T_N), M_c is linearly dependent on B while hysteresis loops with sharp jumps at coercive magnetic fields B_{coer} due to magnetization reversal are observed at 30 K and 15 K ($T_{\mathrm{comp}} < T < T_{\mathrm{N}}$). Below 30 K, the remanent magnetization M_{rem} decreases with decreasing T toward T_{comp}, but the magnitude of B_{coer} increases. At $T_{\mathrm{comp}} = 9.4$ K, the hysteresis behavior becomes negligible and M_c shows a linear B dependence again. With further decreasing T, hysteresis loops appear again, and M_{rem} (B_{coer}) increases (decreases) toward lower T, as seen in the 7 K and the 5 K data of Fig. 2(b).

Isothermal magnetocapacitance measurements were done at ac electric fields of 10 kHz [Figs. 2(c) and 2(d)] or 100 kHz [Figs. 3.2(e) and 3.2(f)], at which the most pronounced magnetocapacitive effects were observed. At 70 K (> T_{N}), magnetocapacitance is negligibly small while it becomes evident at $T_{\mathrm{comp}} < T < T_{\mathrm{N}}$. As seen in Figs. 3.2(c) and 3.2(e), the magnitude of $\Delta\varepsilon'_c(B)/\varepsilon'_c(0)$ increases with decreasing T, and a clear butterfly-shape is observed in the $\Delta\varepsilon'_c(B)/\varepsilon'_c(0)$-$B$ curve at 15 K. At $T_{\mathrm{comp}} = 9.4$ K, the butterfly-shaped hysteresis in $\Delta\varepsilon'_c(B)/\varepsilon'_c(0)$ disappears again [Figs. 3.2(d) and 3.2(f)], which also corresponds to the disappearance of the hysteresis in M_c. Below T_{comp}, the butterfly-shaped magnetocapacitance shows up again in accordance with the re-emergence of the hysteresis behavior in M_c. The observed butterfly curves can be ascribed to the magnetization reversal process because the magnetic field where $\Delta\varepsilon'_c(B)/\varepsilon'_c(0)$ increases abruptly corresponds well to B_{coer} in each M_c-B curve. The magnetocapacitance curves above and below T_{comp} show a sharp contrast, though both of them exhibit the butterfly-shaped hysteresis, and the corresponding M_c-B curves show similar hysteresis loops. Above T_{comp}, $\Delta\varepsilon'_c(B)/\varepsilon'_c(0)$ abruptly increases at B_{coer} [Figs. 3.2(c) and 3.2(e)], whereas it shows a sudden drop below T_{comp} [Figs. 3.2(d) and 3.2(f)]. In other words, the features of the magnetocapacitance above and below T_{comp} are opposite in sign to each other.

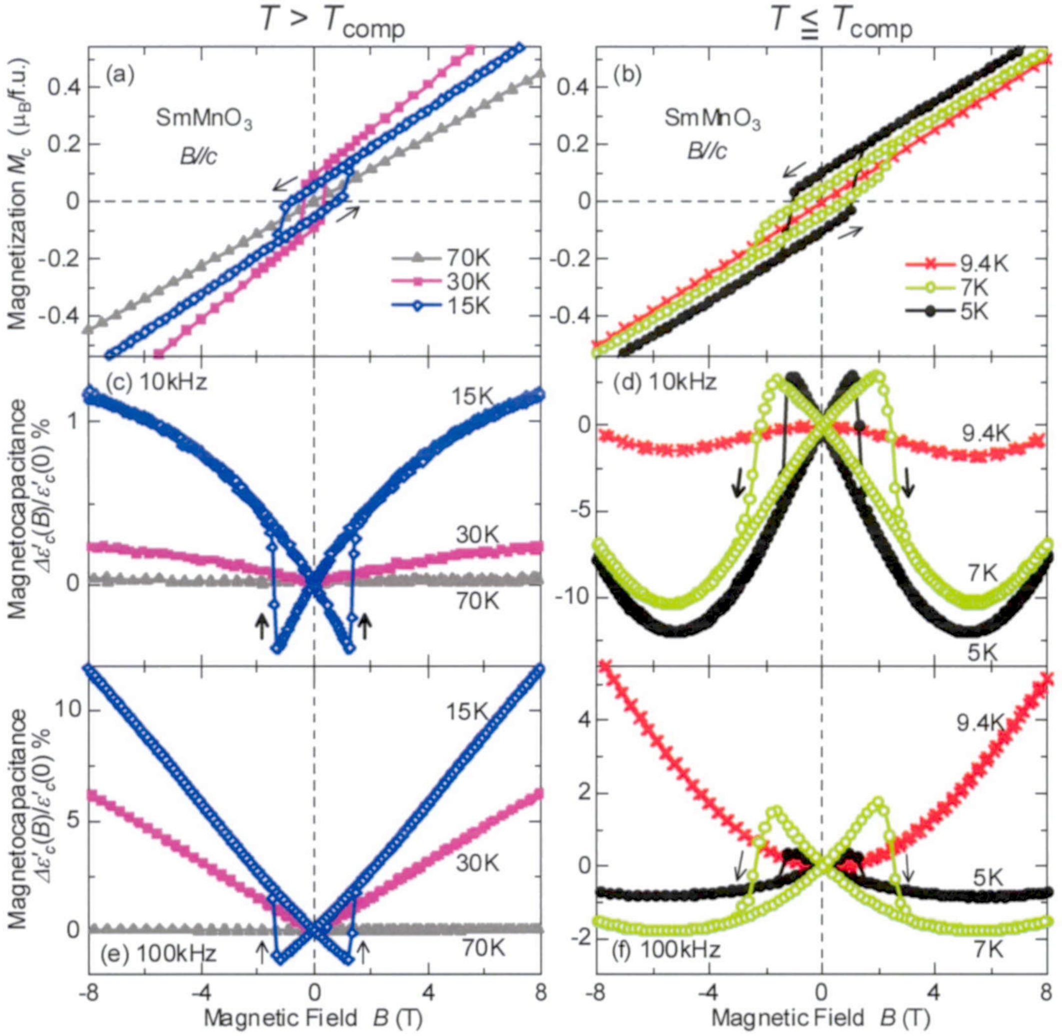

Figure 3.2. Isothermal magnetization curves measured at temperatures (a) above and (b) below T_{comp} for $\mathrm{SmMnO_3}$. (c)-(f) Corresponding magnetocapacitance curves measured at 10 and 100 kHz. Magnetic fields are applied along the *c* axis.

3.3.3. Magnetic phase diagram and hard XMCD results for $SmMnO_3$

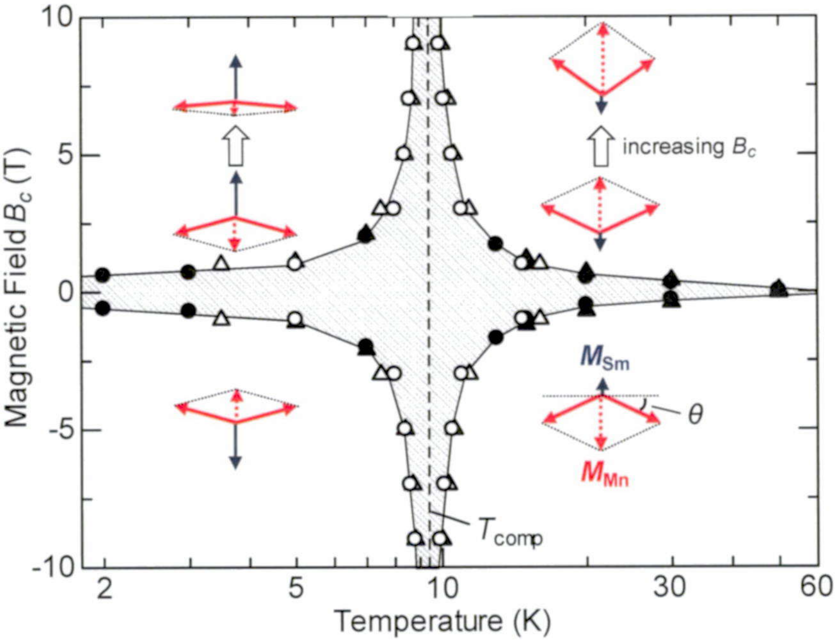

Figure 3.3. Magnetic phase diagram of $SmMnO_3$. Illustrations in the inset depict possible configurations of polarized Sm (blue arrows) and canted Mn (red arrows) moments in the respective phases. Open and closed triangles represent B_{coer} obtained from the M_c-B and the ε'_c-B curves, respectively. Open and closed circles represent T_{jump} obtained from the M_c-T and the ε'_c-T curves, respectively. The gray area represents the hysteresis region.

Figure 3.3 displays the B-T phase diagram in which phase boundaries were determined by T_{jump} [circles] or B_{coer} [triangles]. The phase diagram clearly shows that the T_{jump} at which the anomalies were observed in the M_c-T and ε'_c-T curves overlaps B_{coer} at which the magnetization reversal occurs. The gray area in the phase diagram represents the hysteresis region. With increasing B at around T_{comp}, B_{coer} shows a tendency to diverge and T_{jump} approaches T_{comp} from both the low- and the high-T ends. Such a tendency is often observed in Néel N-type ferrimagnetic compounds [16]. We schematically illustrate possible orientations of M_{Sm} and M_{Mn} with respect to $B//c$ in each phase [insets of Fig. 3.3]. At $|B| \leq \sim 0.5$ T, the system cannot cross the phase boundary down to the lowest T. Therefore, there is no change in the relative configurations of M_{Sm} and M_{Mn} with respect to B, and the negative magnetization state appears. By contrast, at $|B| > \sim 0.5$ T, the system does cross the boundary at T_{jump}. When the energy of applied B exceeds the magnetic anisotropy energy, the states with positive magnetization may become more stable. Thus, the reversals of both M_{Sm} and M_{Mn} [right insets ↔ left insets of Fig. 3.3] are likely to occur at T_{jump}.

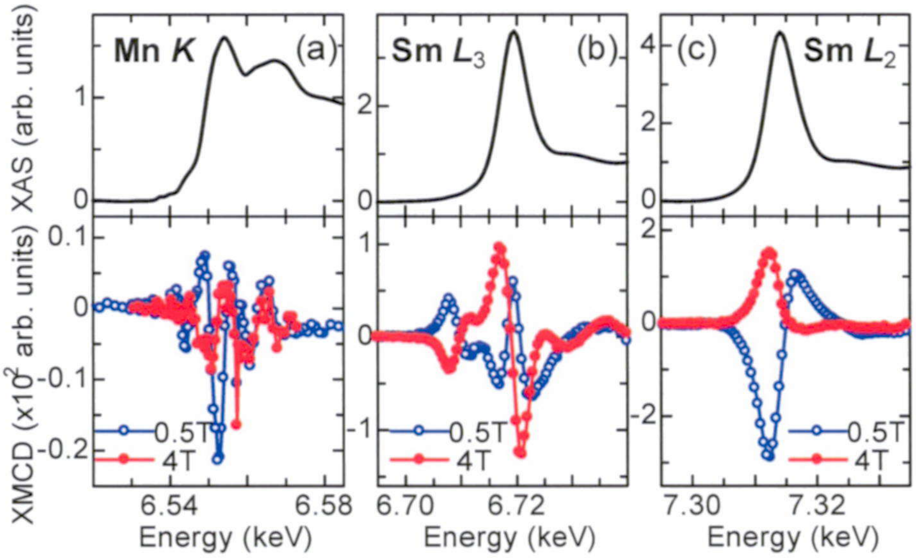

Figure 3.4. (a), (b), and (c) show XAS and XMCD signals of Mn K, Sm L_3, and Sm L_2-edges, respectively, at 2 K. After field-cooling at 0.5 T, the measurements were done at 0.5 T and 4 T.

The reversals of M_{Sm} and M_{Mn} in crossing the phase boundary were demonstrated by XMCD measurements. Figures 3.4(a), 3(b), and 3(c) show the XAS (upper) and the XMCD (lower) spectra around Mn *K*, Sm L_3, and Sm L_2-edges, respectively. For these measurements, the sample was first field-cooled down to 2 K at 0.5 T. Subsequently, the spectra were taken at 0.5 T ($<B_{\mathrm{coer}}$) and then at 4 T ($>B_{\mathrm{coer}}$). In all three spectra, the XMCD signals at 4 T are opposite in sign to those at 0.5 T. This result indicates that both M_{Sm} and M_{Mn} are reversed when crossing the phase boundary, as illustrated in the insets of Fig. 3.3.

In addition, the possible relative orientations between them above and below T_{comp} schematically drawn in Fig. 3.1(a) are well supported by the temperature profile of XMCD signals at 6.553 keV (Mn-*K* edge) and 6.708 keV (Sm-L_3 edge), represented by open triangles and squares, respectively. The XMCD spectra were obtained in B = 0.5 T for the powder $SmMnO_3$. The temperature profiles of the sum of the two XMCD signals [= C×(Mn-*K*) + (Sm-L_3), where C is constant] well overlap that of the low-field M_c-T curve [Compare open circles with black line in Fig. 3.5].

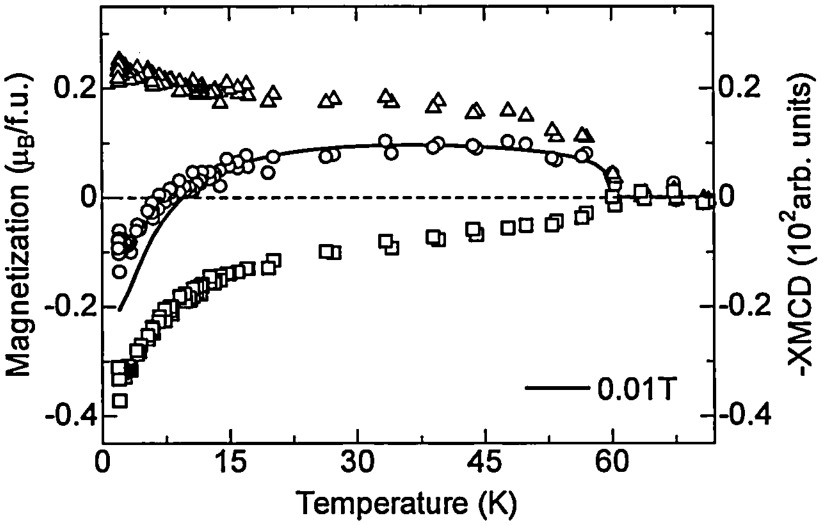

Figure 3.5. Left axis: T profiles of M measured at B_c = 0.01 T (after field-cooled procedure) for a single crystal of $SmMnO_3$. Right axis: Open triangles and squares represent XMCD signals at 6.553 keV (Mn-*K* edge) and 6.708 keV (Sm-L_3 edge), respectively. Open circles represent the sum of these two XMCD signals [= C×(Mn-*K*) + (Sm-L_3), where C is a constant value].

3.3.4. Asymmetric magnetocapacitance at compensation temperature

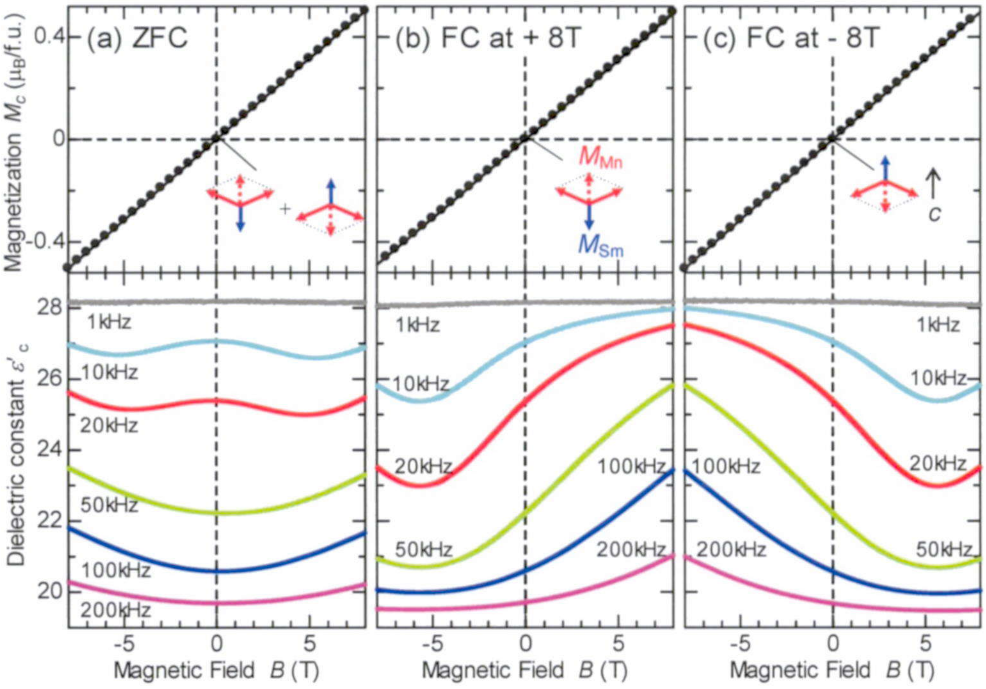

Figure 3.6. B dependence of M_c and ε'_c at $T_{\mathrm{comp}} = 9.4$ K after (a) ZFC, (b) FC at +8 T, and (c) FC at B = -8 T procedures. The insets show possible configurations of M_{Mn} and M_{Sm} in the respective cooled states.

Next, we present the peculiar cooling-field dependent asymmetric magnetocapacitance observed at T_{comp}. Figure 4 shows the B profiles of M_c and ε'_c at 9.4 K (= T_{comp}). The data in Figs. 3.6(a), 3(b), and 3(c) were measured after the zero-field cooling (ZFC), the FC at + 8 T, and the FC at - 8 T above T_N, respectively. Regardless of the cooling procedures, all the M_c-B curves show exactly the same B-linear behavior and pass through the origin (upper panels of Fig. 4), which means that the system behaves as an antiferromagnet at T_{comp} ($M_{\mathrm{Mn}} + M_{\mathrm{Sm}} = 0$). By contrast, the ε'_c-B curves strongly depend on the cooling process. In the ZFC data, the ε'_c-B curves display symmetric appearances centering around $B = 0$ T, while the ε'_c-B curves after the FC at +8 T and -8 T are asymmetric and show mirror-reversed appearances of each other. The observed cooling-process dependence on the magnetocapacitance can be explained by considering the existence of two-types of domains whose volume ratio depends on the cooling procedure, as illustrated in the insets of Fig. 3.6.

3.3.5. Dielectric dispersion

Rare-earth manganites show another intriguing phenomenon. With or without the ferroelectricity, most of the above-mentioned RMnO$_3$ show distinct dielectric dispersions, namely, a relaxation feature at low temperatures only when an ac electric field is applied along the c axis $E//c$ [7, 11]. So far, this feature has not been discussed in detail and its origin is unclear. In this thesis, we provide a detailed investigation of the relaxation effect of $E//c$ in SmMnO$_3$.

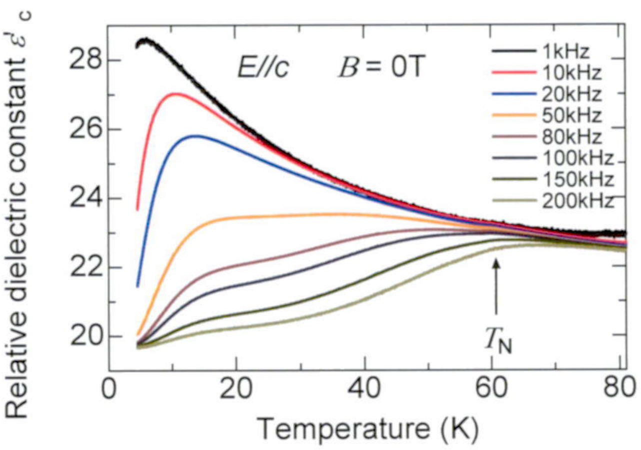

Figure 3.7. T dependent ε'_c at selected f with $B = 0$ T.

First, we show ε'_c dependent on T measured at $B = 0$ T. As seen in Fig. 3.7, ε'_c strongly depends on frequency f over a wide T range. Below $\sim T_N$, ε'_c is significantly suppressed with increasing f. Next, when B_c is applied, as seen in Fig. 3.8, the anomaly in ε'_c is not clear in the low-f (1 kHz) data but becomes pronounced with increasing f. The dielectric anomaly at T_{jump} is ascribed to the opposite magnetocapacitive effect, that is, the enhancement and the suppression of ε'_c by the application of B (up to ~6 T) above and below T_{jump}, respectively.

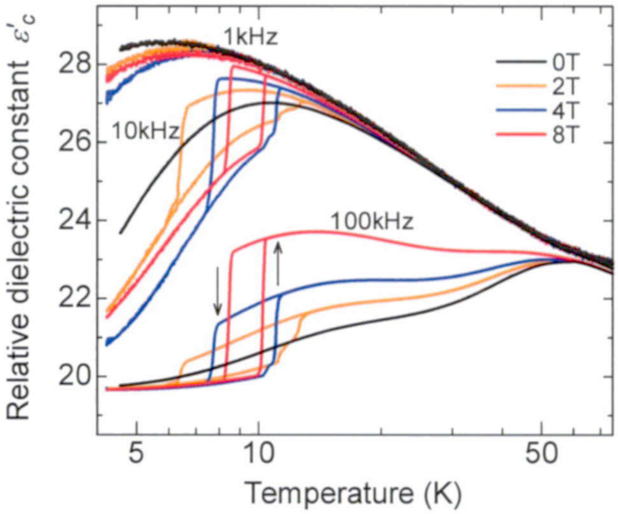

Figure 3.8. T profiles of ε'_c at selected f with B_c.

Then, we investigated f dependent ε'_c and ε''_c in the absence and presence of B_c. Figures. 3.9 (a), (b), and (c) show f profiles of ε'_c, ε''_c, and a Cole-Cole circular arc which is well fitted by the empirical Cole-Cole function measured at $B_c = 0$ at selected T, respectively. The Cole-Cole function considers various relaxation times different from the Debye equation where only one single relaxation time is assumed, as reported for various RMnO$_3$ [7]:

$$\varepsilon_r^* = \varepsilon_{r\infty} + \frac{\varepsilon_{r0} - \varepsilon_{r\infty}}{1 + (i\omega\tau_0)^{\beta}} , \tag{3.1}$$

$$\varepsilon_r' = \varepsilon_{r\infty} + \frac{1}{2}(\varepsilon_{r0} - \varepsilon_{r\infty})\left\{1 - \frac{\sinh \beta x}{\cosh \beta x + \cos(\beta\pi/2)}\right\} , \tag{3.2}$$

$$\varepsilon_r'' = \frac{1}{2}(\varepsilon_{r0} - \varepsilon_{r\infty})\frac{\sin(\beta\pi/2)}{\cosh\beta x + \cos(\beta\pi/2)}, \tag{3.3}$$

where τ_0 is average relaxation time, β is the degree of relaxation time dispersion, and $x = \ln\omega\tau_0$, respectively. Figures 3.10 and 3.11 show the f dependence of (a) ε'_c, (b) ε''_c, and (c) the Cole-Cole circular arc measured at $B_c = 8$ T on the field cooling and heating process at selected T, respectively. On the cooling (heating) process with 8 T, a shoulder in ε'_c abruptly shifted down (up) and a peak in ε''_c rapidly shifted toward lower f (higher f) around T_{jump} (10.1 K on heating process) where the anomaly in M_c and ε'_c appeared in Fig. 3.1.

From the fitting, we obtained the relaxation time τ which is given by $\tau = (2\pi f_p)^{-1}$, where f_p is the frequency of the ε''_c peak. As shown in Fig. 3.12(a), τ gradually increases with decreasing T at $B = 0$ T. Since the dielectric dispersion is evident below T_N (see Fig. 3.7), it implies that it is likely related to the magnetic ordering of the Mn moments. Additionally, in accordance with abrupt changes in M_c and ε'_c, τ in high B data also shows a sudden jump at T_{jump}. In Fig. 3.12(b), we also provide relaxation distribution β dependent on T and B given by ε'_c part fitting on the cooling run at selected B_c. The β gradually becomes large for lower T. At T_{jump} in M_c and ε'_c, the β displays abrupt jumps, and the magnitude of changes in β becomes larger with increasing B_c.

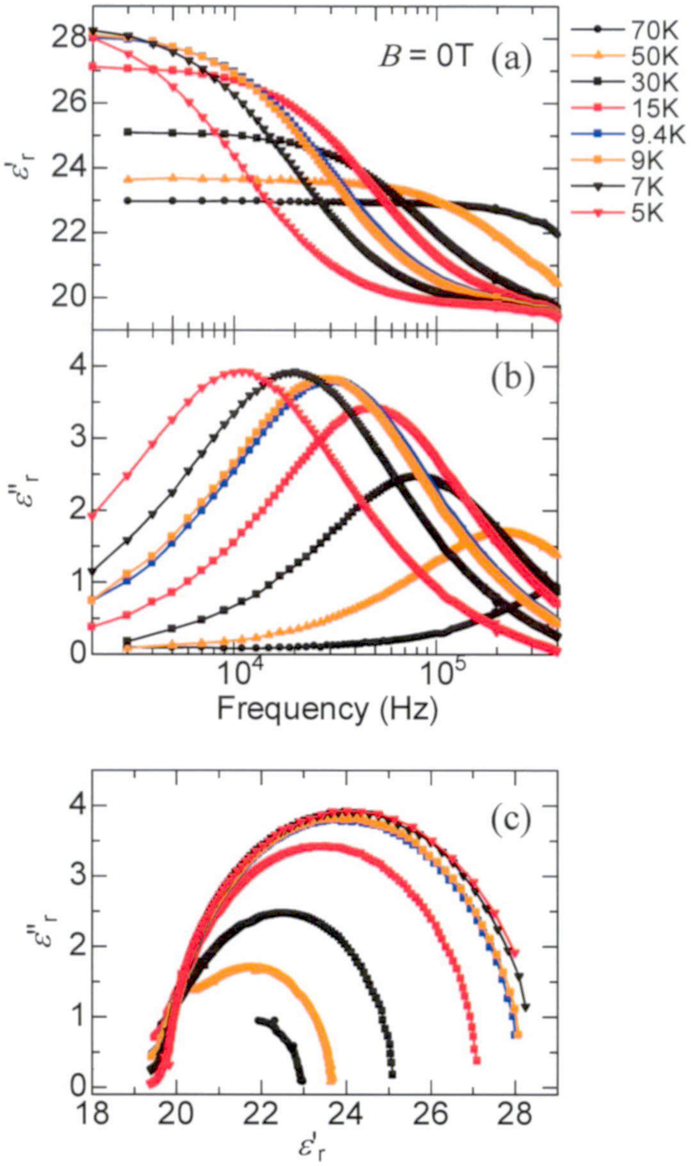

Figure 3.9. f dependent (a) ε'_c, (b) ε''_c, and (c) Cole-Cole circular arc without application of B at selected T.

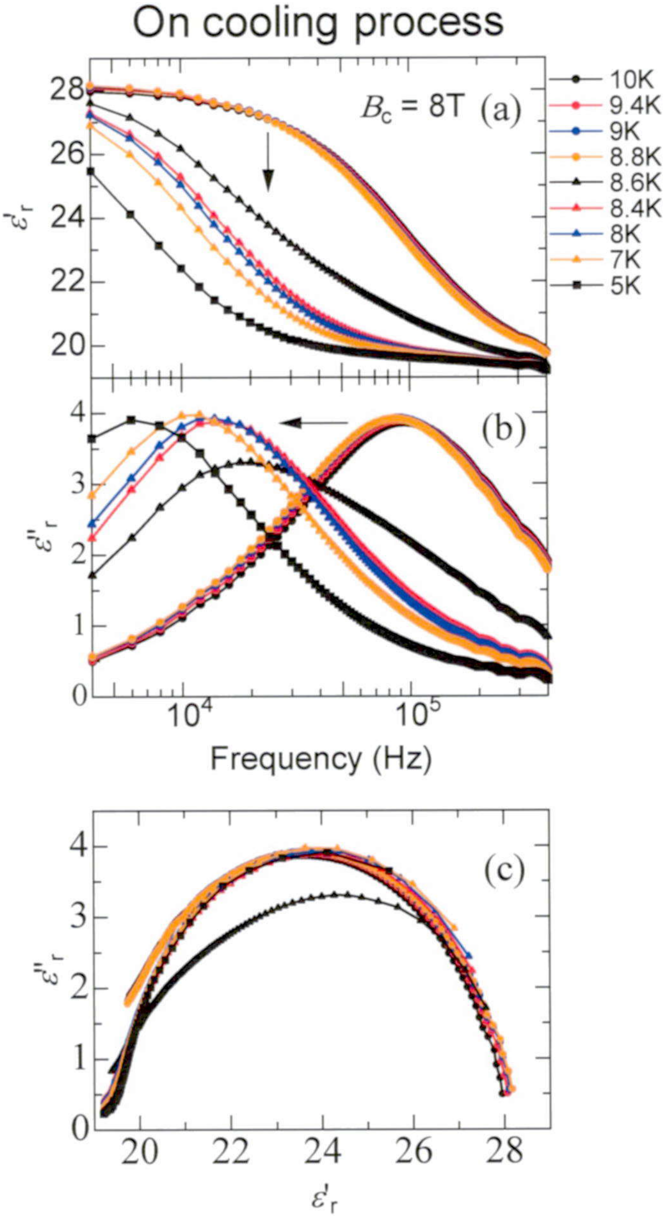

Figure 3.10. *f* dependent (a) ε'_c, (b) ε''_c, and (c) Cole-Cole circular arc with application of B_c = 8 T at selected *T* on the cooling run.

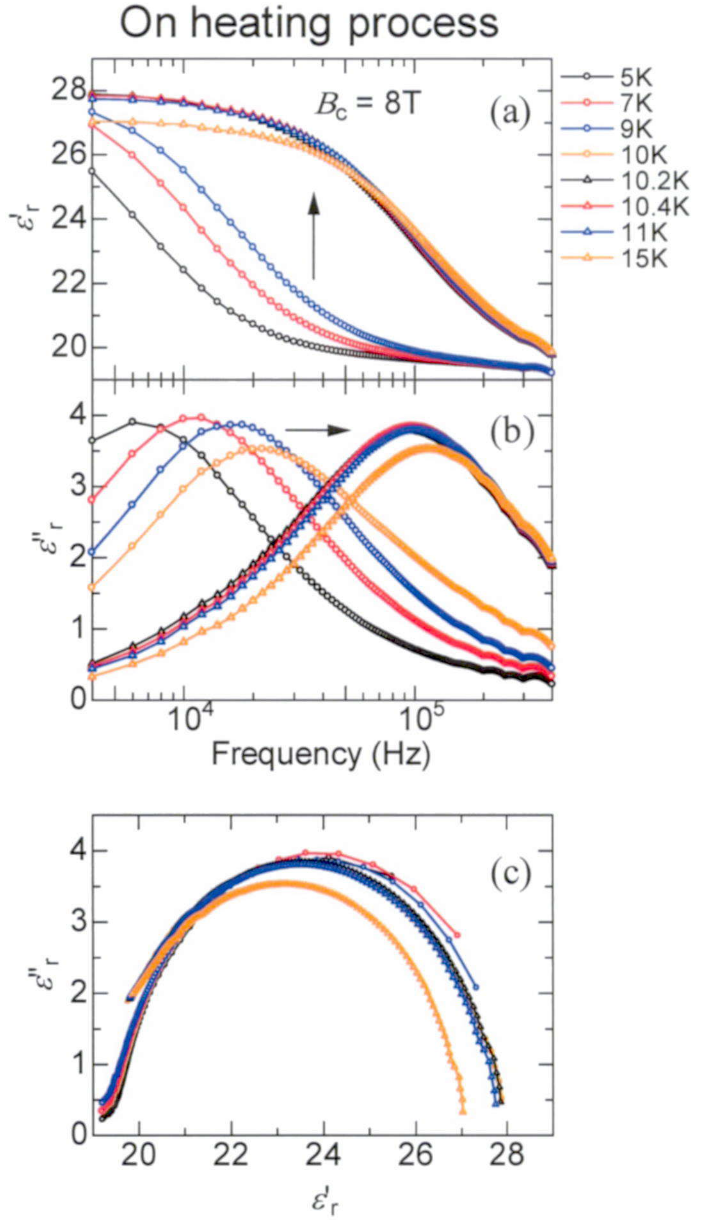

Figure 3.11. *f* dependent (a) ε'_c, (b) ε''_c, and (c) Cole-Cole circular arc with application of B_c = 8 T at selected *T* on the warming run.

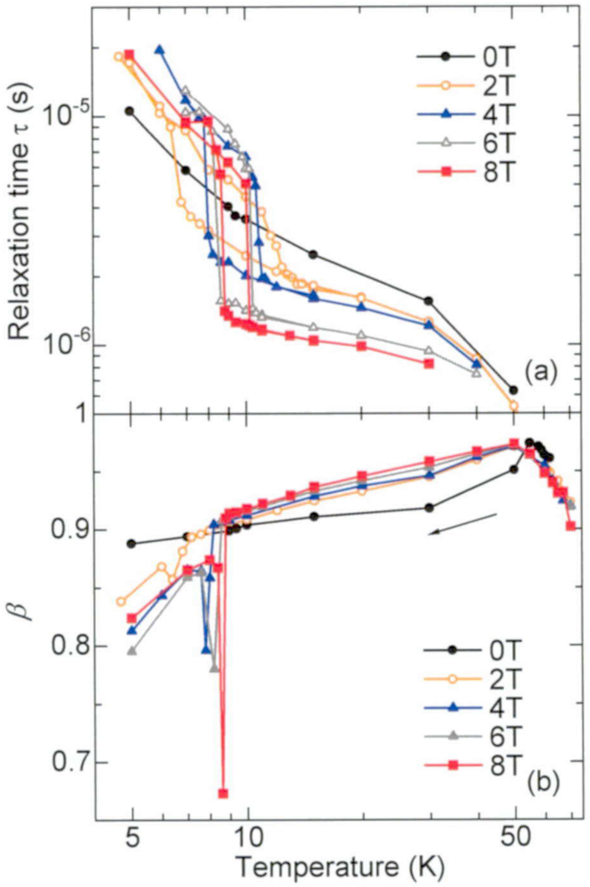

Figure 3.12. T profiles of (a) τ and (b) β at selected B_c.

3.4. Discussion

Let us discuss the origin of the distinctive magnetocapacitive effect in $SmMnO_3$. Since M_{Mn} is expected to be parallel to B above T_{jump}, the canting angle of the Mn moments (θ) becomes large with increasing B [upper-right inset of Fig. 3.3]. By contrast, θ becomes small with increasing B below T_{jump} where M_{Mn} is antiparallel to B [upper-left inset of Fig. 3.3]. Thus, the application of B yields opposite effects on θ above and below T_{jump}. As seen in Fig. 3.12(a), τ decreases monotonically with increasing B above T_{jump}, while τ increases with increasing B up to ~5 T below T_{jump}. The change in τ by applying B well corresponds to that in θ, which suggests that the change in θ plays an important role in the observed magnetocapacitive effect characterized by τ. Furthermore, sudden changes in τ as well as ε'_c at T_{jump} (or B_{coer}) can be also explained in terms of an abrupt change in θ. When the system crosses a boundary between phases with M_{Mn} parallel and antiparallel to B at T_{jump} (or B_{coer}), θ should also change abruptly. Although the microscopic mechanism of the close correlation between θ on τ is still unclear, the present finding will provide a clue to understanding the dielectric dispersion observed in RMnO$_3$.

3.5. Summary of this chapter

Magnetocapacitive effects were investigated for Néel *N*-type ferrimagnetic $SmMnO_3$ showing temperature-induced magnetization reversal due to keen competition between ferrimagnetically-coupled polarized Sm and canted Mn moments. It was found first-order like anomalies in the magnetic and dielectric properties around the compensation point, which consequently causes the large magnetocapacitive effects. The simultaneous reversals of the coupled Sm-Mn moments induced by applied magnetic fields are ascribed to the anomalies. Furthermore, the peculiar asymmetric magnetocapacitance was observed at the compensation temperature.

Bibliography for Chapter 3

[1]T. Kimura, T. Goto, H. Shintani, K. Ishizaka, T. Arima, and Y. Tokura, Nature **426**, 55 (2003).

[2]S.-W. Cheong and M. Mostovoy, Nat. Mater. **6**, 13 (2007).

[3]M. Kenzelmann, A. B. Harris, S. Jonas, C. Broholm, J. Schefer, S. B. Kim, C. L. Zhang, S.-W. Cheong, O. P. Vajk, and J. W. Lynn, Phys. Rev. Lett. **95**, 087206 (2005).

[4]M. Mostovoy, Phys. Rev. Lett. **96**, 067601 (2006).

[5]A. Sergienko, C. Sen, and E. Dagotto, Phys. Rev. Lett. **97**, 227204 (2006).

[6]V. Y. Pomajakushin, M. Kenzelmann, A. Doenni, A. B. Harris, T. Nakajima, S. Mitsuda, M. Tachibana, L. Keller, J. Mesot, H. Kitazawa, and E. Takayama-Muromachi, New. J. Phys. **11**, 043019 (2009).

[7]T. Goto, T. Kimura, G. Lawes, A. P. Ramirez, and Y. Tokura, Phys. Rev. Lett. **92**, 257201 (2004).

[8]S. Ishiwata, Y. Kaneko, Y. Tokunaga, Y. Taguchi, T. H. Arima, and Y. Tokura, Phys. Rev. B **81**, 100411(R) (2010).

[9]T. Kimura, S. Ishihara, H. Shintani, T. Arima, K. T. Takahashi, K. Ishizaka, and Y. Tokura, Phys. Rev. B **68**, 060403 (R) (2003)

[10]V. Skumryev, F. Ott, J. M. D. Coey, A. Anane, J. -P. Renard, L. Pinsard-Gaudart, and A. Revcolevschi, Eur. Phys. J. B **11**, 401 (1999).

[11]F. Schrettle, P. Lunkenheimer, J. Hemberger, V. Yu. Ivanov, A. A. Mukhin, A. M. Balbashov, and A. Loidl, Phys. Rev. Lett. **102**, 207208 (2009).

[12]V. Y. Ivanov, A. A. Mukhin, A. S. Prokhorov, and A. M. Balbashov, Phys. Stat. Sol. (b) **236**, 445 (2003).

[13]L. Néel, Ann. Phys. (Paris) **3**, 137 (1948).

[14]N. Menyuk, K. Dwight, and D. G. Wickhan, Phys. Rev. Lett. **4**, 119 (1960).

[15]M. Suzuki, N. Kawamura, M. Mizumaki, A. Urata, H. Maruyama, S. Goto, and T. Ishikawa, Jpn. J. Appl. Phys. **37**, L1488 (1998).

[16] e.g., J. P. Hanton and A. H. Morrish, J. Appl. Phys. **36**, 1007 (1965).

Chapter 4.

Lattice distortion accompanied by magnetization reversal in A-type antiferromagnetic manganites

---

4.1. Introduction

In this chapter, magnetostriction was investigated for layered A-type antiferromagnetic $SmMnO_3$ showing large magnetocapacitive effects around a temperature ($T_{TP} = T_{jump}$ in chapter 3) where ferrimagnetically coupled Mn $3d$ and Sm $4f$ moments are reversed simultaneously. At a sweeping temperature or a magnetic field, a significant lattice distortion was observed at T_{TP} or the coercive field, respectively. This indicates that the lattice is strongly coupled with the magnetic configuration. More recently, Cheng and coworkers reported that their measurements of in-field x-ray diffraction and specific heat for $SmMnO_3$ showed no evidence that the transition at T_{TP} is first-order (e.g., volume change and latent heat) despite its abrupt nature [1]. Therefore, to further examine the transition nature at T_{TP}, magnetostrictive effects were studied for single crystals of $SmMnO_3$ by measurements of the striction L with high resolution ($\Delta L/L < \sim 10^{-5}$). Our striction data demonstrate the presence of a discontinuous lattice distortion at T_{TP}, which has never been reported. We discuss the origin of the lattice distortion accompanied by the magnetization reversal at T_{TP} in terms of the partial change in orbital-occupancy of Mn e_g electrons.

4.2. Experimental procedures

A single crystal of $SmMnO_3$ was grown by the floating-zone method. The growth was carried out with the use of a halogen-lamp image furnace at a growth rate of 8 mm/h in a flow of N_2 gas. The obtained crystals were oriented by using Laue x-ray diffraction patterns and were cut into rectangular plates ($\approx 4 \times 4 \times 2$ mm^3) with the widest faces along the crystallographic principal axes: the *a*, *b*, and *c* axes, in the *Pbnm* setting, respectively. For the striction ($\Delta L/L$) measurements, uniaxial strain gauges with a length of 1 mm were used, which were attached to the widest face of the samples. Magnetic fields (B_c) were applied only along the *c* axis. To minimize the unwanted magnetoresistive effect of the gauges, the conventional active and dummy (a copper plate) method was carried out. The obtained striction data were corrected by subtracting the thermal expansion of copper [2]. Magnetization (M_c) and real part of dielectric constant (ε'_c) were also measured as reported previously [3]. For comparison with $SmMnO_3$ results, we also grew a single crystal of $EuMnO_3$, which is unaffected by rare-earth Eu moments ($Eu^{3+} = 4f^6$; $L = 3$, $S = 3$, and $J = 0$, i.e., non-magnetic ion) to its magnetic properties, and measured the magnetostriction along the *c* axis.

4.3. Striction measurement results

4.3.1. Temperature dependence of striction under magnetic fields for $SmMnO_3$

First, we performed re-measurements of M_c and ε'_c (10 kHz) dependent on T and B_c, respectively. As seen in Figs. 4.1(a) and (b), in a low magnetic field applied along c ($B_c <\sim 1$ T), $SmMnO_3$ shows temperature (T)-induced magnetization reversal at the compensation temperature ($T_{\mathrm{comp}} \approx 9.4$ K), while in higher B_c ($>\sim 1$ T), T profiles of M_c and ε'_c show an abrupt change with thermal hysteresis at a temperature (T_{TP}) around T_{comp}, suggesting that a first-order-like phase transition takes place at T_{TP} [see the 4 T and 8 T data in Fig. 4.1(a)] [3]. Furthermore, as seen in isothermal M_c [Fig. 4.1(c)] and magnetocapacitance [Fig. 4.1(d)] curves, the magnetization reversal at the coercive field (B_{coer}) accompanies a sudden change in ε'_c. Here, a distinct behavior is that the butterfly-shaped ε'_c–B_c curves below and above T_{TP} exhibit signs opposite to each other, which indicates the opposed magnetic configurations in the two T ranges for the $SmMnO_3$ system. It has been discussed that the anomalies in M_c and ε'_c at T_{TP} (or B_{coer}) are ascribed to the simultaneous reversal of the ferrimagnetically coupled Mn 3*d* and Sm 4*f* moments and the resultant sudden change in the canting angle of Mn moments [3].

Next, let us examine T dependence of the striction for $SmMnO_3$. Figures. 4.2(a), (b), and (c) show the T dependence of the striction parallel to the a, b, and c axes [$\Delta L_a(T)/L_a(70\mathrm{K})$, $\Delta L_b(T)/L_b(70\mathrm{K})$, and $\Delta L_c(T)/L_c(70\mathrm{K})$], respectively, in the absence and the presence of applied B_c. All the striction data were measured upon the heating process. First, let us focus on the data at $B_c = 0$ T. With decreasing T, an anomaly is evident at T_{N} in the data of $\Delta L_a(T)/L_a(70\mathrm{K})$ and $\Delta L_b(T)/L_b(70\mathrm{K})$, while no anomaly is observed in $\Delta L_c(T)/L_c(70\mathrm{K})$.

With further decreasing T, $\Delta L_a(T)/L_a(70\mathrm{K})$ steadily elongates while $\Delta L_b(T)/L_b(70\mathrm{K})$ and $\Delta L_c(T)/L_c(70\mathrm{K})$ gradually contract. A similar magnetostrictive effect, i.e., the elongation along a and the contraction along b below T_{N}, has been observed in a typical A-type AFM manganite, $LaMnO_3$, by a neutron diffraction measurement [4].

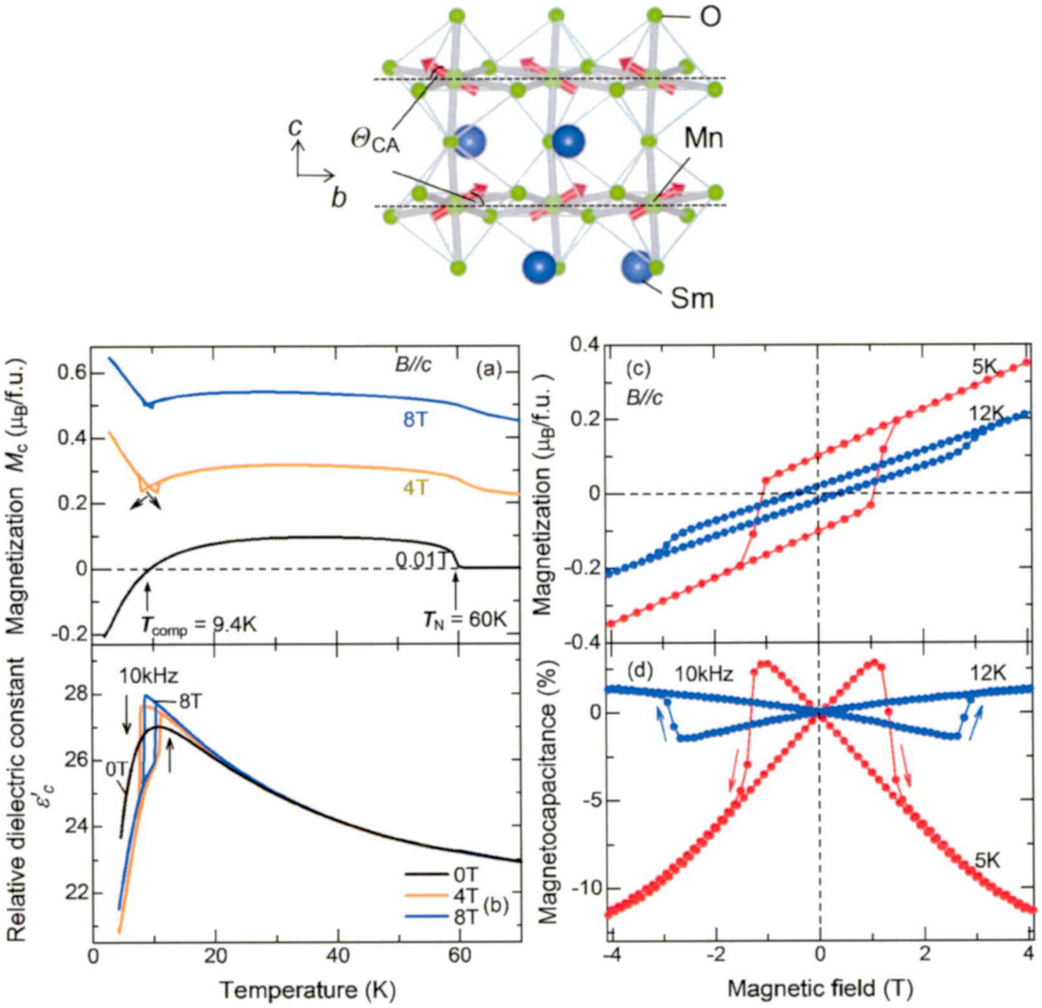

Figure 4.1. The upper figure illustrates crystal and magnetic structures of A-type AFM RMnO$_3$. Red arrows denote Mn moments, and Θ_{CA} corresponds to the canting angle of the Mn moments. T dependence of (a) M_c and (b) ε'_c (10 kHz) measured at selected B, and B dependence of (c) M_c and (d) magnetocapacitance (10 kHz) measured at 5 K and 12 K, below and above T_{comp} ($\approx$ 9.4 K) for single crystals of SmMnO$_3$, respectively. For all the measurements, magnetic fields were applied along the c axis ($B//c$).

Namely, the A-type AFM order in the manganites gives rise to a lattice distortion which is the most pronounced within the *ab* plane. This lattice distortion can be understood in terms of the exchange striction [5, 6]. The development of the A-type AFM order with the ferromagnetic coupling within the *ab* plane probably expands the Mn-O-Mn bond angle φ in the *ab* plane through the exchange striction. In fact, the *a* and *b* axes in RMnO$_3$ with large φ are longer and shorter than those in RMnO$_3$ with small φ, respectively [e.g., a = 5.5367(1) Å, b = 5.7473(1) Å, φ= 155.11(5)° in LaMnO$_3$ (ref. 7); a = 5.3548(6) Å, b = 5.8131(7) Å, φ= 147.53(5)° in SmMnO$_3$ (ref. 8)]. In light of these relationships, the present observation, i.e., the elongation of *a* and the contraction of *b* at T_N, can be reasonably explained.

Next, we focus on the striction data in B_c = 4 T and 8 T. At $T_{TP} < T < T_N$, Though the effect of B_c on $\Delta L_a(T)/L_a$(70K) is negligibly small, $\Delta L_b(T)/L_b$(70K) and $\Delta L_c(T)/L_c$(70K) gradually contract and elongate with increasing B_c, respectively. Another noteworthy feature in the in-field striction data is that sudden jumps appear in all the directions at T_{TP} where M_c-T and ε'_c-T curves show discontinuous anomalies. As seen in the insets of Fig. 4.2, $\Delta L_a(T)/L_a$(70K) and $\Delta L_b(T)/L_b$(70K) show a discontinuous jump at T_{TP} toward lower temperatures while $\Delta L_c(T)/L_c$(70K) suddenly drops at T_{TP}. With increasing B_c, T_{TP} approaches T_{comp} in the manner of M_c and ε'_c in Figs. 4.1(a) and 4.1(b), and the change in $\Delta L(T_{TP})/L$ increases in all directions. The largest magnetostrictive effect is observed in $\Delta L_c(T_{TP})/L_c$. Then, in contrast with the data at $T > T_{TP}$, $\Delta L_a(T)/L_a$(70K), and $\Delta L_b(T)/L_b$(70K) elongate while $\Delta L_c(T)/L_c$(70K) contracts with increasing B_c at $T < T_{TP}$. Though no lattice anomaly at T_{TP} had been observed in the previous in-field x-ray diffraction measurement at B = 5 T [1], our striction measurement with higher resolution clearly demonstrates the presence of the lattice anomaly at T_{TP}.

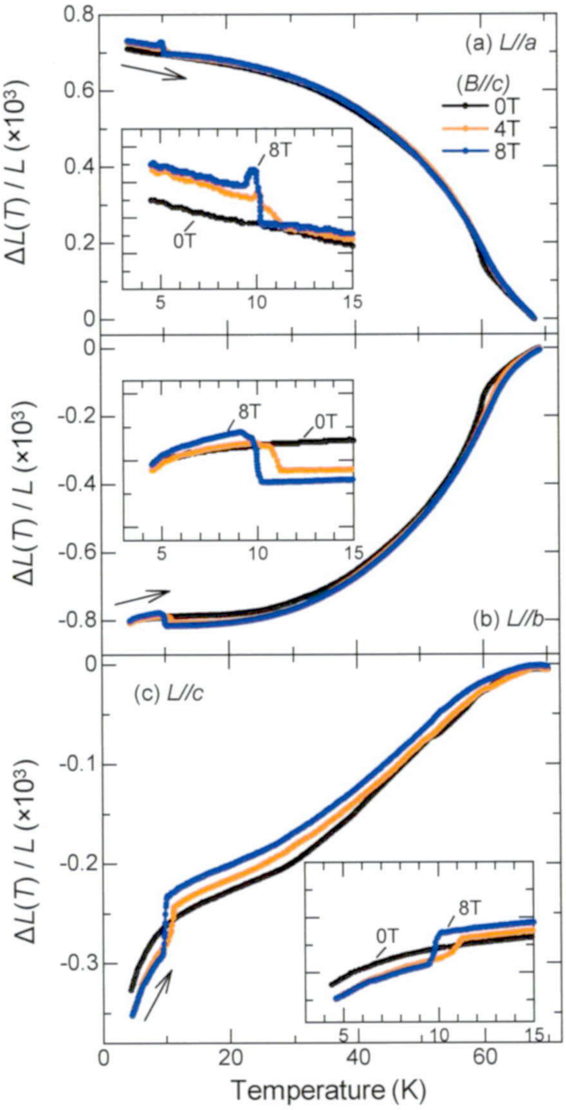

Figure. 4.2. *T* profiles of the striction parallel to the (a) *a*, (b) *b*, and (c) *c* axes [$\Delta L_a(T)/L_a(70\mathrm{K})$, $\Delta L_b(T)/L_b(70\mathrm{K})$, and $\Delta L_c(T)/L_c(70\mathrm{K})$] at selected B_c, respectively. All the data were measured during the heating process. The insets show the magnification around T_{comp}. Magnetic fields are applied along the *c* axis (*B*//*c*).

4.3.2. Magnetic field dependence of striction for $SmMnO_3$

To further examine the B effects on the striction behavior for $SmMnO_3$, we measured the isothermal magnetostriction along the a, b, and c axes [$\Delta L_a(B)/L_a$, $\Delta L_b(B)/L_b$, and $\Delta L_c(B)/L_c$]. Figures 4.3 shows (a) $\Delta L_a(B)/L_a$, (b) $\Delta L_b(B)/L_b$, and (c) $\Delta L_c(B)/L_c$ as functions of B_c at 5 K and 12 K, i.e., below and above T_{TP}. One of the remarkable features in Fig. 4.3 is that all the striction data except for $\Delta L_a(B)/L_a$ at 12 K display drastic changes at around B_{coer}, ± 1.2 T for 5 K and ± 2.7 T for 12 K [compare Fig. 4.3 and Fig. 4.1(c)], respectively. Though no anomaly was observed in $\Delta L_a(B)/L_a$ at 12 K (above T_{TP}), the result is consistent with that in the T dependence of $\Delta L_a(T)/L_a(70\mathrm{K})$ shown in Fig. 2(a) in which the negligibly small B effect was observed at $T_{TP} < T < T_N$. The drastic changes in $\Delta L(B)/L$ at B_{coer} mean that the magnetization reversal also affects the lattice. The magnitude of the magnetostriction along the c axis around B_{coer} is of the order of 10^{-4}, which is one order of magnitude larger than that along the a and b axes. Owing to the drastic change in $\Delta L(B)/L$ at B_{coer}, the isothermal magnetostriction curves form butterfly shapes. In all the configurations, $\Delta L(B)/L$ monotonically increases or decreases in all the B regions except for B_{coer}. Another noteworthy feature in Fig. 4.3 is the sign of the magnetostriction. At 12 K (above T_{TP}), $\Delta L_b(B)/L_b$ shows a sudden decrease at B_{coer} toward higher B while $\Delta L_c(B)/L_c$ exhibits an abrupt increase. At 5 K (below T_{TP}), by contrast, $\Delta L_b(B)/L_b$ increases while $\Delta L_c(B)/L_c$ decreases. Related to the opposite feature, the signs of the butterfly-shaped magnetostriction curves are reversed above and below T_{TP}. This contrasting butterfly shape in the magnetostriction reminds us of the magnetocapacitance result in Fig. 4.1(d).

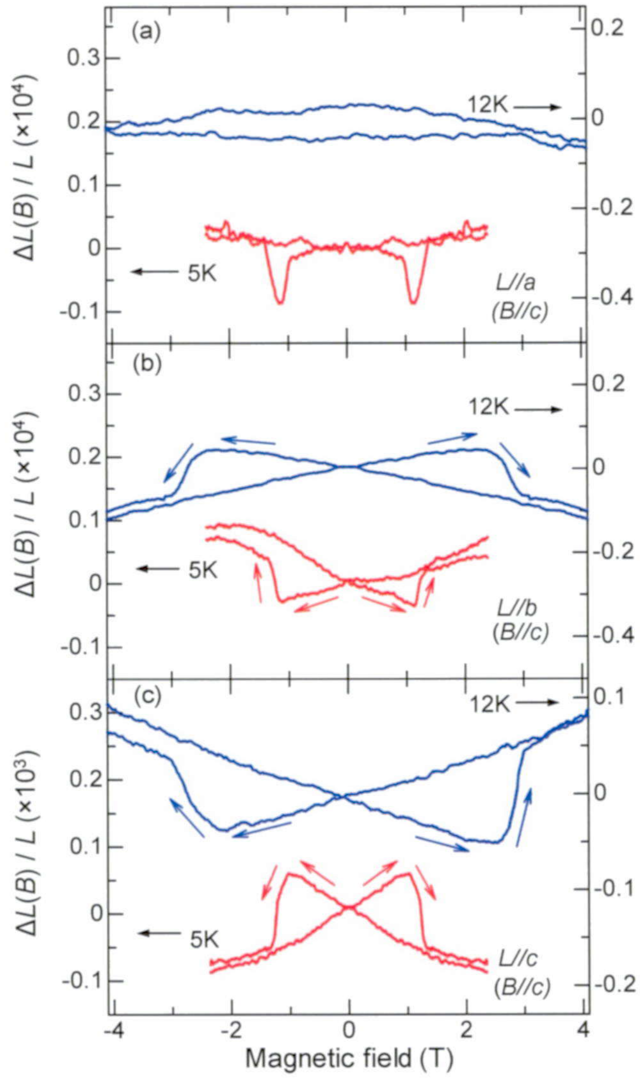

Fig. 4.3. Isothermal magnetostriction curves parallel to the (a) *a* and (b) *b* axes [$\Delta L_a(B)/L_a$ and $\Delta L_b(B)/L_b$] measured at temperatures, 5 K and 12 K (below and above T_{TP}), respectively, for $SmMnO_3$. (c) Corresponding the curves parallel to the *c* axis [$\Delta L_c(B)/L_c$] at 5 K and 12 K for $SmMnO_3$, respectively.

4.3.3. Magnetic field profiles of $EuMnO_3$ striction

Additionally, we also measured the magnetostriction of another A-type AFM manganite, $EuMnO_3$, in which the rare-earth moments do not contribute to its magnetic properties. The thin black lines in Fig. 4.4 show the $\Delta L_c(B)/L_c$ data of $EuMnO_3$ measured under the same conditions as those of $SmMnO_3$. The $\Delta L_c(B)/L_c$ at 12 K in $EuMnO_3$ is similar to that in $SmMnO_3$ in terms of the butterfly-shaped hysteresis and its sign. At 5 K in $EuMnO_3$, however, the sign of the butterfly-shaped $\Delta L_c(B)/L_c$ curve is the same as that at 12 K, which is in sharp contrast with the result of $SmMnO_3$. The magnitude of the magnetostriction in $EuMnO_3$ is much smaller than that in $SmMnO_3$ as well. These results suggest that while the 4*f* moments may enhance the magnetostrictive effect, the Mn moments alone can give rise to the effect.

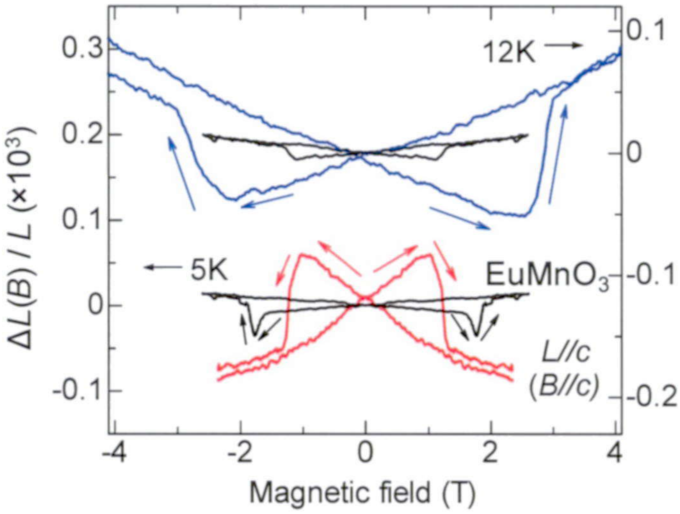

Figure 4.4. Isothermal magnetostriction curves parallel to the curves parallel to the *c* axis [$\Delta L_c(B)/L_c$] at 5 K and 12 K for $SmMnO_3$ (red and blue lines) and $EuMnO_3$ (black lines), respectively.

4.4. Discussion

By considering the magnetization and magnetostriction results, we infer a close connection between the magnetostriction and the canting angle of the weakly ferromagnetic Mn moments Θ_{CA}. The observed monotonic change in $\Delta L(B)/L$ may be ascribed to the monotonic change in Θ_{CA} by applying B_c. In this case, the existence of the sudden change in $L(B)/L$ at B_{coer} suggests that the magnetization reversal accompanies the change in Θ_{CA}. Furthermore, the sign change in the magnetostriction between the data above and below T_{TP} supports a former proposal [3] that the moment configurations composed of the ferrimagnetically coupled Sm and Mn moments are opposite at temperatures below and above T_{TP}.

4.4.1. In terms of the DM interaction

Let us discuss the microscopic mechanism of the observed lattice distortion. A possible driving force to induce the lattice distortion is the DM interaction. In the A-type AFM manganites, the spin canting toward the *c* axis originates from the DM interaction. The change in the canting angle Θ_{CA} may shift the position of oxygen ions intervening between adjacent Mn moments along the *c* axis through the inverse DM effect. At $T_{TP} < T < T_N$, the net magnetization due to the canted Mn moments is aligned along B_c, and then the application of B_c should increase Θ_{CA} and enhance the DM interaction. The enhancement of the DM interaction may displace the oxygen ions further away from the midpoint of adjacent Mn moments as displayed in Fig. 4.5(a). As a result, the buckling of MnO_6 octahedra should be enhanced by applying B_c. Then, the *c* axis should be shortened [(see Fig. 4.5(b)]. However, the changes in $\Delta L(T)/L$ obtained by the present experimental results contradict the DM scenario, so the DM scenario does not explain the observed lattice distortion.

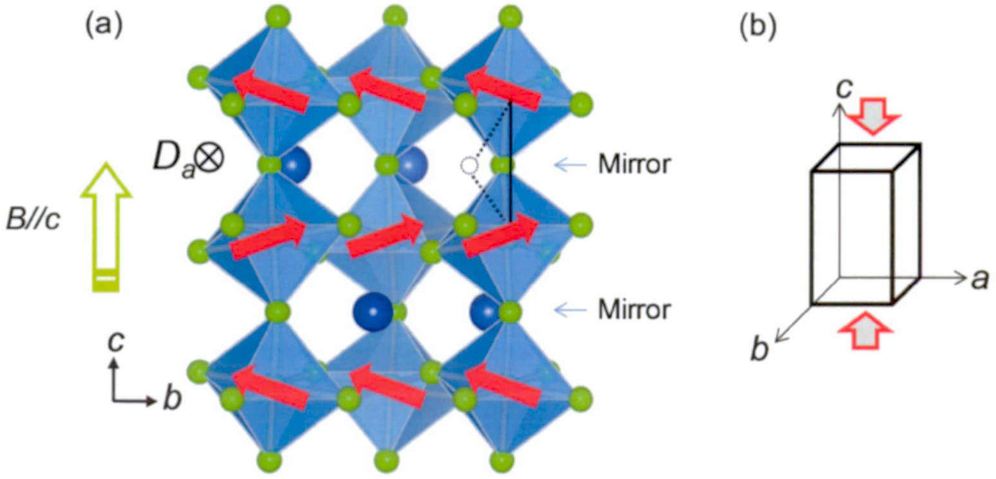

Figure 4.5. (a) A schematic for the DM scenario with oxygen displacement with increasing B_c. (b) shortened *c* axis with consideration of the DM scenario contrast to the magnetostriction result.

4.4.2. In terms of orbital occupancy change

A more plausible driving force to induce the lattice distortion is the change in the orbital occupancy of e_g electrons in Mn sites. In $R\mathrm{MnO_3}$, the occupied Mn e_g orbital wave function on the two inequivalent sites can be expressed by

$$|\pm\rangle^{1} = \cos\frac{\theta}{2}|3z^2 - r^2\rangle \pm \sin\frac{\theta}{2}|x^2 - y^2\rangle, \tag{4. 1}$$

where θ is the respective orbital component (see the lower panels of Fig. 4.6). When θ = 120°, $d_{3x^2-r^2}$ and $d_{3y^2-r^2}$ orbitals are staggeredly-ordered within the *ab* plane. For $\mathrm{SmMnO_3}$, $\theta \approx 114°$, which is obtained by the semiempirical estimate from the structural data [9], infers [c.f., $\theta \approx 108°$ for $\mathrm{LaMnO_3}$ (ref. 10)]. (The θ calculation will be explained in detail in Appendix A.) Apart from the DM interaction, it has been discussed that the competition between the AFM exchange and the local anisotropy can account for the alternating tilt of the magnetization direction which gives rise to a small resulting moment along the c axis [11]. The anisotropy which originates from the spin-orbit coupling may be reflected by the orbital occupancy. It is possible that the application of B_c at $T_{\mathrm{TP}} < T < T_{\mathrm{N}}$ increases the canting angle Θ_{CA}, enhances the c-axis component in the magnetization, and gives rise to the partial transfer of the e_g electrons from the $d_{x^2-y^2}$ to $d_{3z^2-r^2}$ state (i.e., the decrease of θ). Then, by applying B_c, the elongation of L_c is induced by the increase of $d_{3z^2-r^2}$ orbital occupancy while the contraction of the b axis arises from the decrease of $d_{3x^2-r^2}/d_{3y^2-r^2}$ orbital occupancy at $T_{\mathrm{TP}} < T < T_{\mathrm{N}}$.

This orbital-occupancy scenario also well explains the discontinuous change in L at T_{TP} (or B_{coer}) where the simultaneous reversal of Sm and Mn moments occurs. The net magnetization owing to the canted Mn moments is parallel to B_c above T_{TP} while it is antiparallel to B_c below T_{TP} (ref. 3) so that the canting angle above T_{TP} should be larger than that below T_{TP}. This consideration reasonably explains the experimental results, that is, the sudden jumps of L_a and L_b, and the abrupt drop of L_c at T_{TP} upon cooling temperature. Fig. 4.6 displays schematic illustrations which summarize the lattice distortions explained by the orbital-occupancy scenario.

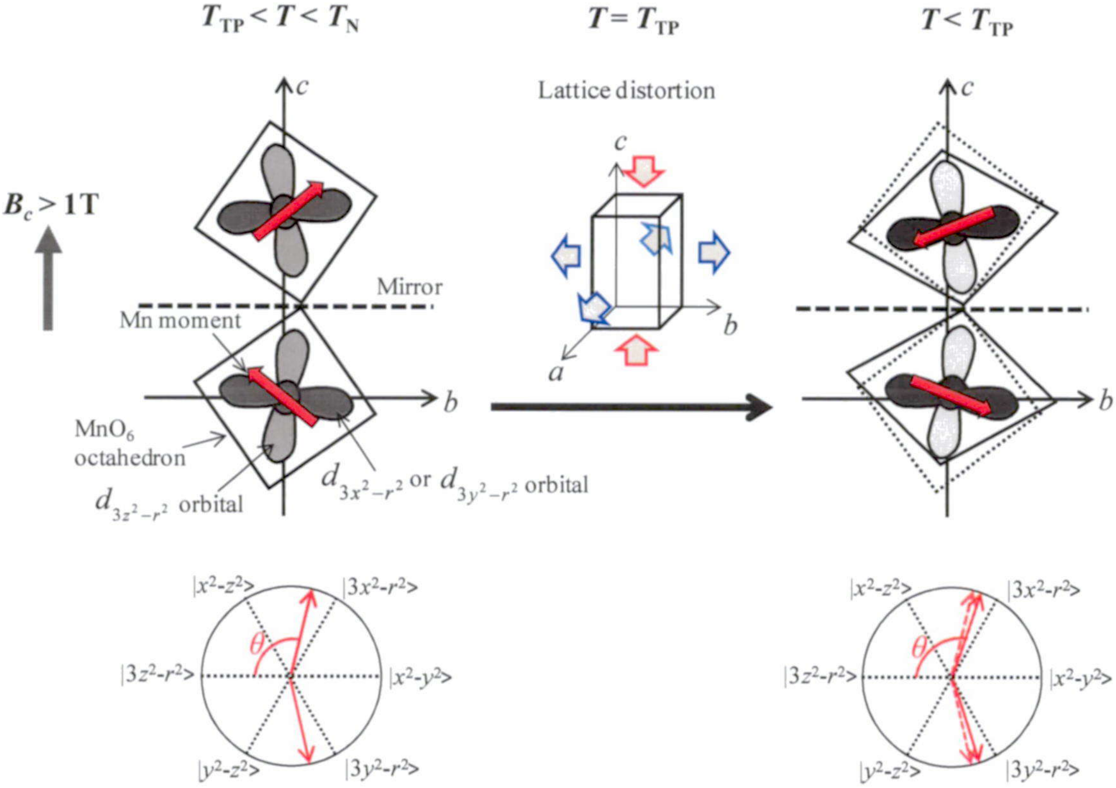

Fig. 4.6. Proposed orbital-occupancy change accompanied by the lattice distortion at T_{TP} in $B_c > 1$ T. (Upper panels) Schematic views of the Mn moments and the Mn $d_{3x^2-r^2}/d_{3y^2-r^2}$ and $d_{3z^2-r^2}$ orbital arrangements in the distorted MnO$_6$ octahedra at $T_{TP} < T < T_N$ (left) and $T < T_{TP}$ (right). The lattice distortion observed at T_{TP} is also illustrated (middle). The grayscale intensity in the orbitals represents the occupancy of Mn e_g electrons. (Lower panels) Proposed θ corresponding to the orbital state of the Mn electrons at $T_{TP} < T < T_N$ (left) and $T < T_{TP}$ (right).

4.5. Summary of this chapter

We investigated the magnetostrictive effect of $SmMnO_3$ with the A-type antiferromagnetic ground state by means of strain gauge measurement. When magnetic fields above 1 T are applied along the *c* axis, a remarkable lattice distortion was observed at the temperature where the simultaneous reversal of the ferrimagnetically coupled Sm 4*f* and Mn 3*d* moments occurs, and at the coercive field where the magnetization reversal arises. A similar but smaller lattice distortion at the coercive field was also observed in A-type antiferromagnetic $EuMnO_3$ in which only Mn moments contribute to its magnetic properties. This indicates that the Mn moments alone can induce the magnetostriction and the rare-earth moments may enhance the effect. We explain the origin of the magnetostriction in terms of the relative orbital-occupancy change in Mn e_g electrons.

Bibliography for Chapter 4

[1]J.-G. Cheng, J.-S. Zhou, J. B. Goodenough, Y. T. Sui, and Y. Ren, Phys. Rev. B **84**, 104415 (2011).

[2]F. R. Kroeger and C. A. Swenson, J. Appl. Phys. **48**, 853 (1977).

[3]J. -S. Jung, A. Iyama, H. Nakamura, M. Mizumaki, N. Kawamura, Y. Wakabayashi, and T. Kimura, Phys. Rev. B **82**, 212403 (2010).

[4]T. Chatterji, P. F. Henry, and B. Ouladdiaf, Phys. Rev. B 77, 212403 (2008).

[5]J. B. Goodenough, Magnetism and the Chemical Bond (John Wiley & Sons, New York, 1963).

[6]J. Kanamori, J. Phys. Chem. Solids **10**, 87 (1959).

[7]J. Rodríguez-Carvajal, M. Hennion, F. Moussa, A. H. Moudden, L. Pinsard, and A. Revcolevschi, Phys. Rev. B **57**, R3189 (1998).

[8]D. O'Flynn, C. V. Tomy, M. R. Lees, A. Daoud-Aladine, and G. Balakrishnan, Phys. Rev. B **83**, 174426 (2011).

[9]F. R. Kroeger and C. A. Swenson, J. Appl. Phys. **48**, 853 (1977).

[10]T. Chatterji, P. F. Henry, and B. Ouladdiaf, Phys. Rev. B 77, 212403 (2008).

[11]V. Y. Ivanov, A. A. Mukhin, A. S. Prokhorov, and A. M. Balbashov, Phys. Stat. Sol. (b) **236**, 445 (2003).

Chapter 5.

Direct evidence of simultaneous reversal of ferrimagnetically coupled Sm 4*f*-Mn 3*d* angular momenta in $SmMnO_3$ by means of soft XMCD technique

---

5.1. Introduction

As mentioned in chapter 3, we performed measurements of hard x-ray magnetic circular dichroism (XMCD) for powder samples of $SmMnO_3$. The results indicated that the observed magnetocapacitive effect is related to the coupling states of the Sm-Mn magnetic moment and their alignments with respect to the direction of an applied magnetic field. However, the XMCD technique using "hard x-ray" is limited to investigations around the Mn K edge ($1s \rightarrow 4p$) and Sm $L_{2,3}$ edges ($2p_{1/2,3/2} \rightarrow 5d$). Since these transitions are not directly related to Mn 3*d* and Sm 4*f* moments which mainly contribute to magnetic properties of $SmMnO_3$, the hard XMCD result could not lead us to the exact magnetic configurations of the Sm and Mn moments.

Therefore, the main target of this chapter is to investigate the respective magnetic states of Sm 4*f* and Mn 3*d* moments in $SmMnO_3$ below and above T_{TP} by means of XMCD measurements using "a soft x-ray", and is to understand the microscopic origin of the large magnetocapacitive effect. By using soft x-rays for the Sm $M_{4,5}$ ($3d_{3/2,5/2} \rightarrow 4f$) and Mn $L_{2,3}$ ($2p_{1/2,3/2} \rightarrow 3d$) edges, it is expected that we will obtain information about Sm 4*f* and Mn 3*d* magnetic states, respectively. Here, we introduce soft XMCD results depending on T and B_c, and represent the calculated sum rule deduced from the XMCD signals for Sm 4*f* and Mn 3*d* angular momenta, respectively. Finally, we discuss a plausible microscopic origin of the magnetocapacitive effect in terms of the simultaneously reversed angular momenta of Sm 4*f* and Mn 3*d*.

5.2. Experimental procedures

Our measurements were performed at the beamline BL25SU of SPring-8. We adopt the helicity-switching method with 1 Hz to obtain x-ray absorption spectra (XAS) and XMCD signals in the total photoelectron yield (TEY) technique. A single crystal of $SmMnO_3$ grown by the floating zone method was prepared for the measurement. For the TEY mode, the sample was fractured in air, and then, the fractured surface nearly parallel to the *c* axis was coated with 1 nm of platinum to prevent charge-up on the fractured surface of insulating $SmMnO_3$. The XMCD signals ($= I^+ - I^- = \mu^+ - \mu^-$) were obtained from the difference between the intensities of right and left polarized XAS or the difference between x-ray absorption coefficients with the helicity of the circular polarization parallel (μ^+) and antiparallel (μ^-) to the direction of magnetization. In this work, the polarized x-rays were irradiated on the fractured sample surface. Magnetic fields were applied normal to the surface, i.e., normal to the *c* axis (B_c) by an electromagnet. XAS and XMCD signals for Sm $M_{4,5}$ and Mn $L_{2,3}$ edges were measured at various T with $B_c = \pm 0.1$ and +1.9 T, on the heating process after the field-cooled procedure. To compare the XMCD signals with magnetization hysteresis loops, we measured XMCD signals at the respective edges as a function of B_c was also measured at 15 K. Prior to the XMCD measurements, *M*-*T* curves were measured at $B_c = +0.1$ and +1.9 T for a sample with the same shape as that for the XMCD measurements to confirm the reproducibility of the compensation temperature and the abrupt jump in magnetization as previously reported in Ref. [1].

5.3. Soft XMCD results

5.3.1. XMCD signals reversal by changing magnetic field signs

In Fig. 5.1, we show *M-T* curves measured at B_c = +0.1 and +1.9 T. As seen in the figure, *T*-induced magnetization reversal appears below T_{comp} at B_c = +0.1 T, and M_c displays abrupt anomalies around T_{comp} at B_c = +1.9 T. These results are consistent with those shown in chapters 2 and 3.

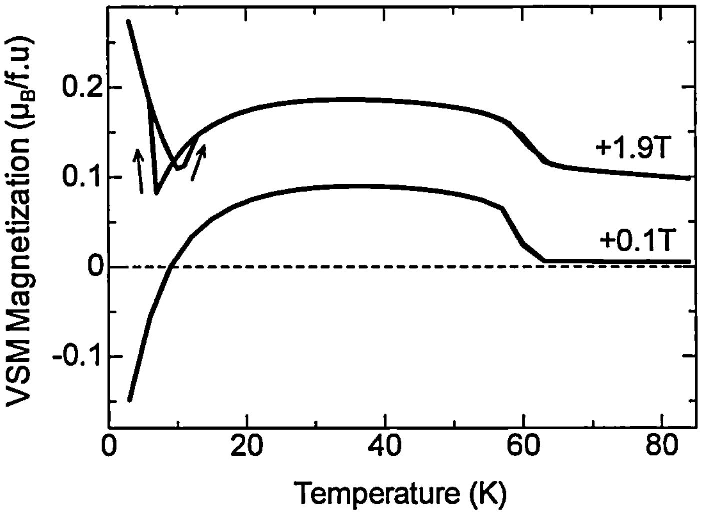

Figure 5.1. *T* profiles of M_c measured at +0.1 and +1.9 T for a single crystal used for soft XMCD measurement. The measurements were done with a VSM-SQUID magnetometer.

Figures 5.2(a) and (b) show normalized XAS and XMCD signals of Sm $M_{4,5}$ edges at 20 K with $B_c = \pm 0.1$ T, respectively. The shape of XAS in Fig. 5.2(a) reveals the typical feature of the trivalent nature of Sm ion [2, 3]. Figures 5.2(a') and 5.2(b') [inset of Fig. 5.2(a)] magnify the peak structure around the M_5 edge and represent μ^+ and μ^- recorded at 20 K with B_c = +0.1 T and –0.1 T, respectively. XMCD signals, i.e., the difference between μ^+

and μ^-, measured at B_c = ±0.1 T are displayed in Fig. 5.2(b). This result clearly demonstrates that the XMCD signals are reversed by changing the sign of B_c, which means that polarized Sm moments are reversed by changing the sign of B_c.

Figure 5.3 shows (a) XAS and (b) XMCD spectra around Mn $L_{2,3}$ edges, measured under the same measurement conditions as the Sm case. Figures 5.3(a') and (b') display magnified views of the XAS spectra around the peak position, measured at B_c = +0.1 T and -0.1 T, respectively. The observed XAS and XMCD signals show sharp peaks at Mn $L_{2,3}$ edges, and characterize the (weak) ferromagnetic behavior of the Mn 3*d* moment in $SmMnO_3$ [1]. T. Koide and coworkers [4] reported the results of XAS and XMCD at Mn $L_{2,3}$ edges for polycrystalline $LaMnO_3$, which is a typical system showing the A-type AF and weak ferromagnetic state. Comparing our data with the results obtained by Ref. 4, our data show more complexity [see the two notable XMCD peaks at an inverted open triangle in Fig. 5.3(b)]. We will discuss this complexity later. Regardless of the existence of the two abnormal peaks, XMCD signals of Mn $L_{2,3}$ edges are also well reversed as seen in Fig. 5.3(b), when applying B_c = -0.1 T. The result also indicates that the canted Mn moments are reversed by changing the sign of B_c.

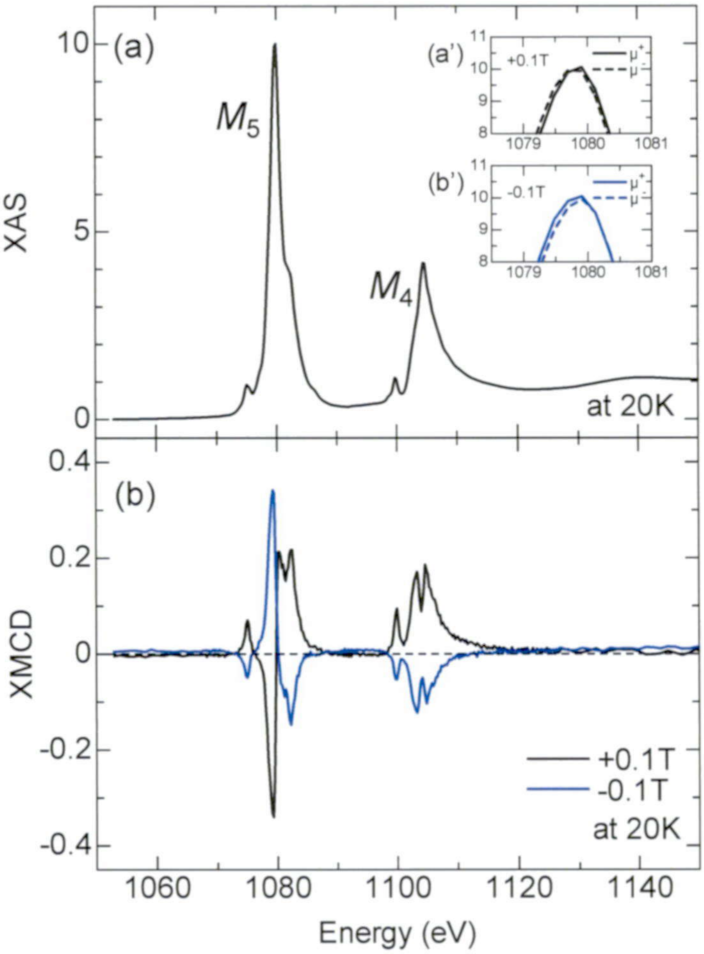

Figure 5.2. Photon energy profiles of (a) XAS and (b) XMCD for Sm $M_{4,5}$ edges recorded at 20 K in $B_c = \pm 0.1$ T for a single crystal of SmMnO$_3$. The insets in Fig. 5.2(a) show μ^+ and μ^- at +0.1 T (a') and -0.1 T (b').

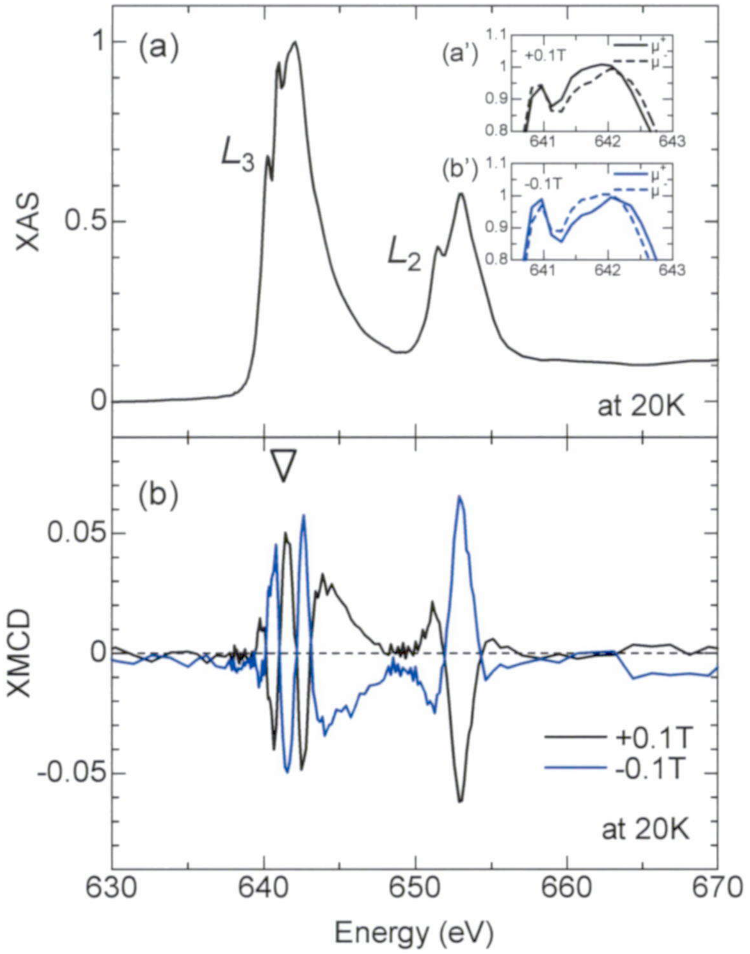

Figure 5.3. Photon energy profiles of (a) XAS and (b) XMCD for Mn $L_{2,3}$ edges recorded at 20 K in $B_c = \pm 0.1$ T for a single crystal of $SmMnO_3$. The insets in Fig. 5.3(a) show μ^+ and μ^- at +0.1 T (a') and -0.1 T (b'), respectively. The inverted open triangle in Fig. 5.3(b) points out the notably complicated peak structures from those of Mn $L_{2,3}$ edges.

5.3.2. *T* and *B* profiles of XMCD signals

Next, we investigated temperature dependent XMCD (=μ^+ - μ^-) signals of Sm $M_{4,5}$ and Mn $L_{2,3}$ edges at various T in a weak (strong) B_c = +0.1 T (+1.9 T). In B_c = +0.1 T, the XMCD intensity of the elements shows no signal at 70 K above T_N, whereas it starts to appear below T_N and gradually increases with decreasing T as seen in Figs. 5.4(a) for Sm and 5.5(a) for Mn. This gradual increase of the XMCD intensity for the two elements is coincident with the hard XMCD results reported in Ref. [1]. The gradual increase of both XMCD intensities can be ascribed to the increasing canting angle of the Mn moments and to enhancing polarization of the Sm moment due to the antiferromagnetic interactions between the Sm and Mn moments [1, 5]. Furthermore, the shapes of the both XMCD signals in B_c = +0.1 T do not change at any of the T ranges studied here.

In the strong B_c (= +1.9 T), the XMCD intensities of Sm $M_{4,5}$ [Fig. 5.4(b)] and Mn $L_{2,3}$ [Fig. 5.5(b)] edges increase with decreasing T in $T_{TP} < T < T_N$, and present almost the same shape as those in the strong B_c (= +1.9 T) at the respective temperatures. However, remarkable features in the XMCD signals of the two edges are observed below T_{TP} ($\approx$ 10.6 K, on heating process) where the abrupt anomalies in both ε'_c and M_c are observed [1]. The reversal of the XMCD signals indicates that both polarized Sm and canted Mn moments are reversed at T_{TP} at the same time. This observation supports the proposal by Jung and coworkers [1] that the large magnetocapacitive effect observed in $SmMnO_3$ is attributed to the simultaneous reversal of the Sm and Mn moments. Below T_{TP}, the XMCD intensities around Sm $M_{4,5}$ and Mn L_3 edges are enhanced with decreasing T (See and compare the data at 9.5 K and at 5.2 K). To further investigate the magnetic field effect on the XMCD signals, we measured the B_c profiles of XMCD at selected photon energies where the XMCD signals show peaks at 15 K. The obtained data around Sm $M_{4,5}$ and Mn L_3 edges are shown in Fig. 5.6(a) and 5.6(b), respectively (Sm M_5-a: 1080.2 eV, Sm M_5-b: 1081.5 eV, Sm M_4-a: 1105.8 eV, Mn L_3-a: 644.2 eV, Mn L_3-b: 644.9 eV, and Mn L_3-c: 646.0 eV). The results clearly demonstrate that hysteresis loops are seen in all of the data. Comparing the coercive field observed in the magnetization (See Fig. 3.2) and the XMCD, we can conclude that the simultaneous reversals of both polarized Sm and canted Mn moments occur at the magnetization reversal observed in M_c-B_c curves.

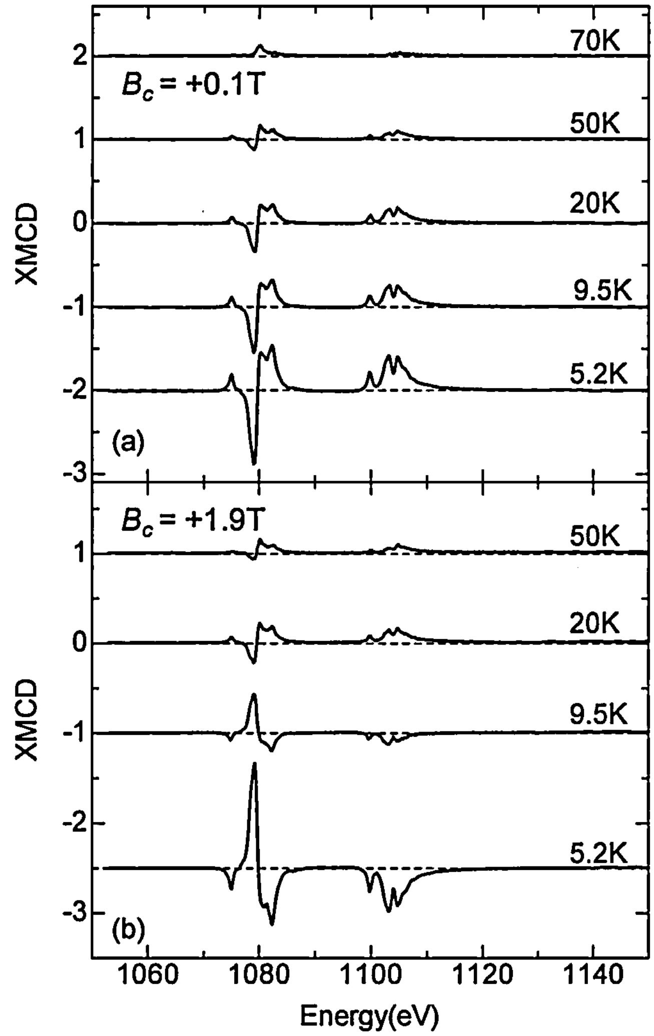

Figure. 5.4. XMCD signals recorded around Sm $M_{4,5}$ edges with photon energy scan in (a) B_c = +0.1 T and (b) B_c = +1.9 T. The measurements were done at 50 K, 20 K, 9.5 K, and 5.2 K.

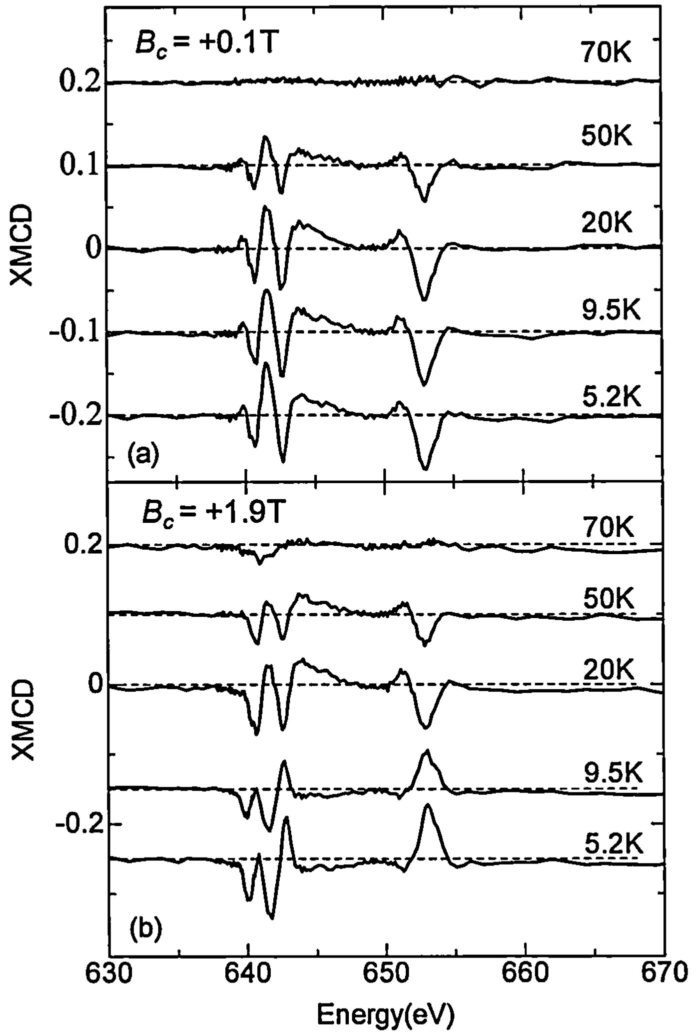

Figure. 5.5. XMCD signals recorded at Mn $L_{2,3}$ edges with photon energy scan at (a) B_c = + 0.1 T and (b) B_c = + 1.9 T. The measurements were done at 50 K, 20 K, 9.5 K, and 5.2 K.

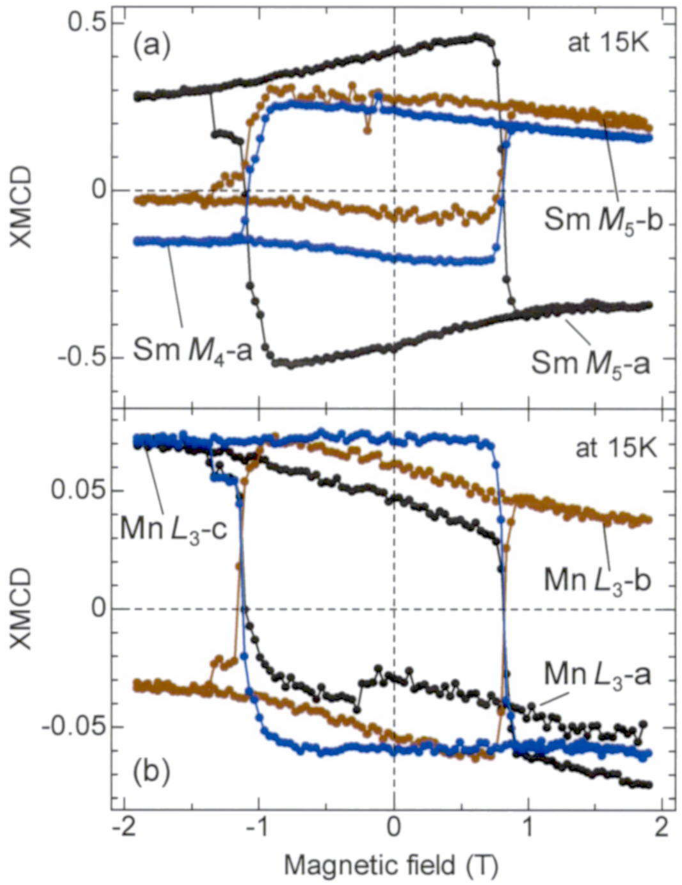

Figure. 5.6. *B* profiles of XMCD signals measured at the selected photon energies corresponding to XMCD peaks of (a) Sm $M_{4,5}$ and (b) Mn L_3 edges at T = 15 K (Sm M_5-a: 1080.2 eV, Sm M_5-b: 1081.5 eV, Sm M_4-a: 1105.8 eV, Mn L_3-a: 644.2 eV, Mn L_3-b: 644.9 eV, and Mn L_3-c: 646.0 eV).

5.3.3. Sum rules for Sm $M_{4,5}$ and Mn $L_{2,3}$ edges

One merit of the soft XMCD technique is that values of spin and orbital angular momenta of 3*d* and 4*f* can be determined separately by the sum rule through the obtained XMCD information [6-8]. We investigated spin and orbital angular momenta m_{SZ}^{Sm} and m_{LZ}^{Sm} for the Sm 4*f* ions, and spin angular momentum m_S^{Mn} for the Mn 3*d* ions as a function of temperature, by using the sum rule based on our XMCD results shown in the previous subsection. The value of Mn 3*d* m_L^{Mn} was too small to observe. Generally, 3*d* transition metals have a small orbital momentum owing to the crystal field effect. For example, reference [4] reported that the orbital momentum value of Mn 3*d* in a polycrystal of $LaMnO_3$ is 3 % of the spin momentum one, which is induced by the DM interaction.

In Fig. 5.7(a) and 5.7(b), we display *T* profiles of separated m_{LZ}^{Sm} and m_{SZ}^{Sm} obtained from XMCD data of Sm $M_{4,5}$ edges at B_c = +0.1 T and +1.9 T, respectively. For the sum rule calculation, we used equations (2.9) and (2.10) for m_{LZ}^{Sm} and m_{SZ}^{Sm} in section 2.5, respectively, and considered magnetic dipole operator $\langle T_Z \rangle$ with the correction factor in Refs. [9,10]. In addition, it assumed that the number of holes in the Sm 4*f* shell is $n_h = 9$, regarded as a free ion (Sm^{3+} with $4f^5$ configuration). As seen in Figs. 5.7(a) and 5.7(b), m_{LZ}^{Sm} and m_{SZ}^{Sm} are always aligned antiparallel to each other, which follows the Hund's rule for $^6H_{5/2}$ in a less-than-half-filled 4*f* electron number. This antiparallel behavior of Sm 4*f* has also been observed in other Sm compounds such as (Sm, Gd)Al_2 [10,11].

As seen in Fig. 5.7(a), in the weak B_c (= +0.1 T), m_{LZ}^{Sm} and m_{SZ}^{Sm} start to be magnetized around T_N at the same time. This indicates that the Sm 4*f* moments are polarized with Mn moment ordering via Sm-Mn antiferromagnetic interaction. With decreasing *T*, m_{LZ}^{Sm} (m_{SZ}^{Sm}) is positive (negative) and gradually increases (decreases), which means that m_{LZ}^{Sm} (m_{SZ}^{Sm}) is parallel (antiparallel) to the net magnetization at B_c = +0.1 T [see Fig. 5.8(a)]. The ratio of $|m_{LZ}^{Sm} / m_{SZ}^{Sm}| > 1$ holds in the whole *T* range. This result, $|m_{LZ}^{Sm} / m_{SZ}^{Sm}| \neq 1$, directly informs us that the zero magnetization at T_{comp} in Fig. 5.1 cannot be achieved only by Sm 4*f* moments, and Mn 3*d* moments aligned antiparallel to the Sm 4*f* moments need to be considered for it.

In a strong B_c (= +1.9 T), m_{LZ}^{Sm} (m_{SZ}^{Sm}) shows the same T dependent behavior and the same positive (negative) value with those in B_c = +0.1 T in $T_{\mathrm{TP}} < T < T_{\mathrm{N}}$ [see Fig. 5.7(b)]. On the other hand, m_{LZ}^{Sm} (m_{SZ}^{Sm}) in B_c = +1.9 T shows a remarkable change at T_{TP} (≈ 10.6 K) , where an anomaly in M_C was observed (Fig. 5.1) and XMCD signals of Sm $M_{4,5}$ edges were reversed [Fig. 5.4(b)]. The m_{LZ}^{Sm} (m_{SZ}^{Sm}) is abruptly switched into a negative (positive) value below T_{TP}. Furthermore, the ratio of $\left|m_{LZ}^{Sm} / m_{SZ}^{Sm}\right|$ suddenly changes at T_{TP} and becomes $\left|m_{LZ}^{Sm} / m_{SZ}^{Sm}\right| < 1$ below T_{TP}, as seen in Fig. 5.8(b). As a result, m_{LZ}^{Sm} (m_{SZ}^{Sm}) becomes antiparallel (parallel) to the net magnetization at B_c = +1.9 T.

Next, let us examine m_S^{Mn} obtained by the sum rule of Mn $L_{2,3}$ edges in B_c = +0.1 and +1.9 T, respectively. For the sum rule calculation, Equation (2.8) in the section 2.5 was used. The 3*d* electron hole number was assumed as n_h = 5.5 which was used for LaMnO$_3$ in Ref. [4]. The correction factor for underestimated m_S^{Mn} values in Mn^{3+} was taken from Refs. [4,12]. Figure 5.9 presents the T dependence of m_S^{Mn} in B_c = +0.1 and +1.9 T. Negative values of m_S^{Mn} start to increase at T_{N}, and they gradually grows with decreasing T in B_c = +0.1 T and +1.9 T. Only in B_c = +1.9 T, m_S^{Mn} shows an abrupt jump around T_{TP} and changes into positive values at below T_{TP}. Though we could not obtain a reliable value of m_L^{Mn} in this measurement, it is expected that m_L^{Mn} (> 0) is always antiparallel to m_S^{Mn} (< 0) for less-than-half-filled 3*d* electron systems. Therefore, when m_S^{Mn} (> 0) is switched at T_{TP} in B_c = +1.9 T, m_L^{Mn} (< 0) should be switched at the same time.

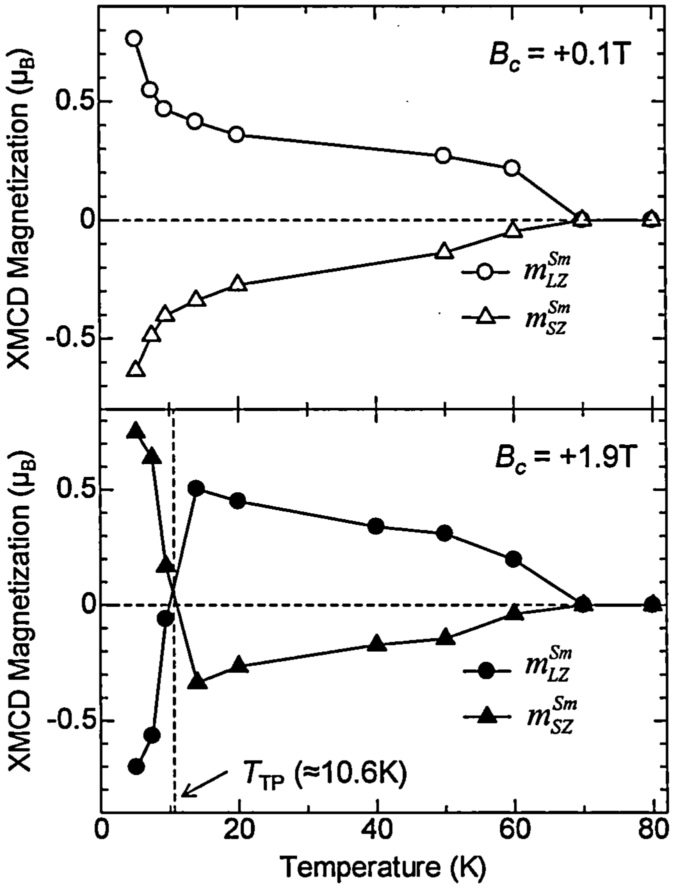

Figure 5.7. *T* profiles of m_{LZ}^{Sm} and m_{SZ}^{Sm} calculated by the sum rule based on Sm $M_{4,5}$ XMCD signals measured at (a) $B_c = +0.1$ T and (b) +1.9 T.

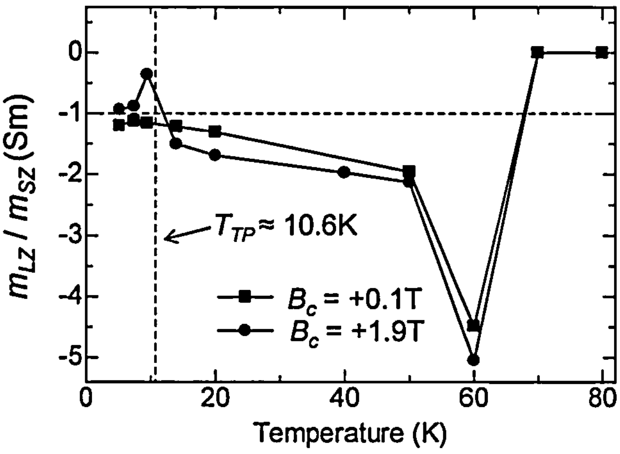

Figure 5.8. *T* profiles of m_{LZ}^{Sm} / m_{SZ}^{Sm} in B_c = +0.1 T and +1.9 T.

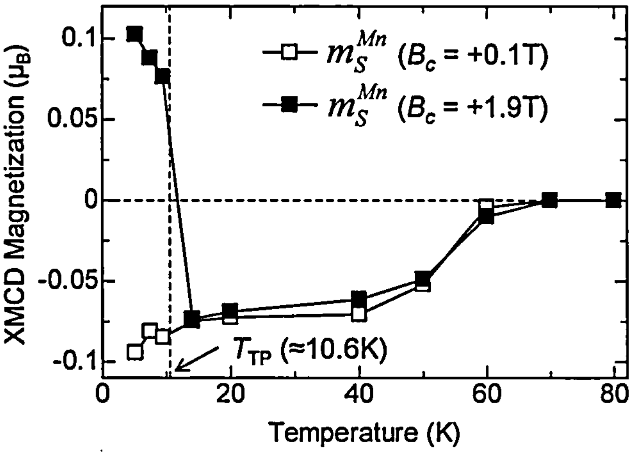

Figure 5.9. *T* profiles of m_S^{Mn} calculated by the sum rule based on Mn $L_{2,3}$ XMCD signals measured at B_c = +0.1 T and +1.9 T.

5.4. Discussion

Now, we discuss the obtained XMCD results of Sm $M_{4,5}$ and Mn $L_{2,3}$ edges. Our first purpose in performing soft XMCD measurement in this study was to ascertain the magnetic states or the magnetic configurations of the Sm $4f$ and Mn $3d$ moments, especially below and above T_{TP} with respect to applied magnetic fields. However, it seems to be difficult to define the magnetic alignment of Sm $4f$ and Mn $3d$ moments (which moment is parallel or antiparallel to $+B_c$) based on the XMCD and sum rule results in this measurement. We observed two notable peaks in XMCD signals for Mn $L_{2,3}$ edges in all the T and B_c ranges investigated in this study [pointed by the inverse triangle in Fig. 5.3(b)]. Such a two-peak structure has never been observed in polycrystalline $LaMnO_3$ [4]. The modulated XMCD intensity by the two peaks may affect the sum rule result not only in that m_S^{Mn} of $SmMnO_3$ single crystal becomes negative, but also in that the sign of m_{LZ}^{Sm} and m_{SZ}^{Sm}, i.e., XMCD signals, is reversed, as Sm-Mn moments should be aligned antiferromagnetically in the present magnetic field region. In fact, it has been reported that the magnitude of the antiferromagnetic interaction between Sm and Mn moments (or internal exchange field) estimated from specific heat and high field measurements corresponds to 15 T [13, 14]. In contrast, m_S^{Mn} of polycrystalline $LaMnO_3$ is positive with respect to $+B$, and the XMCD signal in $LaMnO_3$ never shows the abnormal two-peak structure as observed in $SmMnO_3$. It is widely understood that Mn $3d$ moments in A-type AF ordering $RMnO_3$ are canted via the DM interaction, and their alignments are parallel to an applied magnetic field as shown in m_S^{Mn} (> 0) in a polycrystalline sample of $LaMnO_3$. In spite of this, our result with m_S^{Mn} is the opposite. A possible reason for this opposite result in a single crystal sample of $SmMnO_3$ may be attributed to a sample surface problem. Careful sample preparation is necessary for the soft XMCD technique since XMCD signals are sensitive to the condition of sample surface. In our measurement, however, when a single crystal of $SmMnO_3$ was fractured in an air atmosphere before coating Pt., the sample surface might have reacted to impurities in the air and/or contain excess oxygen so that the valence of some Mn sites becomes 4+ on the surface, which causes the formation of two different crystallographic sites, such as Mn^{3+}/Mn^{4+}. Considering that XMCD signals reflect the magnetic states of a material, the abnormal XMCD signal including the notable two-peak structure in Mn $L_{2,3}$ edges for $SmMnO_3$ might be related to the presence of two different crystallographic sites on the surface. For this reason, the directions of Sm $4f$ and Mn $3d$ moments with respect to B_c were not determined in this study.

However, the sum rule result of Sm $M_{4,5}$ and Mn $L_{2,3}$ XMCD provided us with important information about the magnetic states of Sm $4f$ and Mn $3d$ moments in $B_c = +1.9$ T. We observed simultaneous reversals of m_L^{Sm}, m_S^{Sm}, and m_S^{Mn} angular momenta for the Sm $4f$ and Mn $3d$ at T_{TP}. Additionally, though m_L^{Mn} data were not clearly observed, its value should be finite and is expected to be reversed in accordance with the reversal of m_S^{Mn} at T_{TP} due to Hund's rule. Therefore, our XMCD results reflecting total angular momentum somewhat confirm our previous proposal (described in chapter 3) that the simultaneous reversal of ferrimagnetically coupled Sm $4f$ and Mn $3d$ moments at T_{TP} leads to the large magnetocapacitive effect [1].

Here, let us discuss a plausible microscopic origin of the magnetocapacitive effect accompanied by simultaneous reversal of angular momenta of the Sm $4f$ and Mn $3d$ ions at T_{TP} in $SmMnO_3$. In the previous chapter, we proposed that the origin of the magnetostrictive effect (significant lattice distortion) at T_{TP} is intimately related to the change in the canting angle of Mn moments and to a relative orbital occupancy change from $d_{x^2-y^2}$ to $d_{3z^2-r^2}$ or from $d_{3z^2-r^2}$ to $d_{x^2-y^2}$ in Mn e_g electrons [15]. It is possible that the increased canting angle of Mn moments by applying B_c enhances the orbital angular momentum of the c-axis component and increases the relative occupancy of the $d_{3z^2-r^2}$ orbital state in Mn e_g electrons at $T_{\mathrm{TP}} < T < T_{\mathrm{N}}$ [see Fig. 3.1(b)]. The increased $d_{3z^2-r^2}$ orbital occupancy may evoke hybridization with other $d_{3z^2-r^2}$ orbitals along the c axis via oxygen $2p$ orbitals. Thus, charge transfer through Mn $d_{3z^2-r^2}$ - O $2p$ - Mn $d_{3z^2-r^2}$ hybridization along the c axis may change by applying B_c. In that case, it is plausible that the change in the hybridization along the c axis plays a crucial role in dielectric properties and results in the magnetocapacitive effect. The O 2*p* - Mn 3*d* hybridization may well explain the abrupt change of ε_c at T_{TP}, where the simultaneous reversal of angular momenta of Sm 4*f* and Mn 3*d* occurs. Thus, we conclude that a possible origin of the large and abrupt magnetocapacitive effect at T_{TP} in $\mathrm{SmMnO_3}$ is ascribed to the change in relative O 2*p* – Mn 3*d* hybridization strength caused by the angular momenta inversion, i.e., simultaneous reversal of the Sm 4*f* and Mn 3*d* moments. The Sm 4*f* moments antiferromagetically coupled with Mn 3*d* ones and considered as free ions may not be involved in the magnetocapacitive effect directly, but contribute to the simultaneous angular momenta reversal as the driving force in $\mathrm{SmMnO_3}$ system.

5.5. Summary of this chapter

By means of the soft XMCD technique, we investigated the element specific magnetism in *N*-type ferrimagnetic $\mathrm{SmMnO_3}$ to clarify its origin of the large magnetocapacitive effect. We obtained XMCD signals and performed the sum rule analyses of Sm $M_{4,5}$ and Mn $L_{2,3}$ edges for a single crystal of $\mathrm{SmMnO_3}$. We directly demonstrate that the angular momenta of Sm 4*f* and Mn 3*d* are simultaneously reversed at the transition temperature where the large magnetocapacitive effect is observed. Furthermore, we propose that the magnetocapacitive effect originates from the change in 3*d*-2*p* hybridization which is strongly correlated with magnetic configurations and lattice distortion. The e_g electrons in Mn 3*d* play an important part in the magnetocapacitive effect, while Sm 4*f* may not directly contribute to the effect, it may support the angular moment reversal.

Bibliography for Chapter 5

[1]J. -S. Jung, A. Iyama, H. Nakamura, M. Mizumaki, N. Kawamura, Y. Wakabayashi, and T. Kimura, Phys. Rev. B **82,** 212403 (2010).

[2]B. T. Thole, G. van der Laan, and J. C. Fuggle, Phys. Rev. B **32,** 5107 (1985).

[3]S. S. Dhesi, G. van der Laan, P. Bencok, N. B. Brookes, R. M. Galéra, and P. Ohresser, Phys. Rev. B **82,** 180402(R) (2010).

[4]T. Koide, H. Miyauchi, J. Okamoto, T. Shidara, T. Sekine, T. Saitoh, A. Fujimori, H. Fukutani, M. Takano, and Y. Takeda, Phys. Rev. Lett. **87,** 246404 (2001).

[5]V. Y. Ivanov, A. A. Mukhin, A. S. Prokhorov, and A. M. Balbashov, Phys. Stat. Sol. (b) **236,** 445 (2003).

[6]B. T. Thole, P. Carra, F. Sette, and g. van der Laan, Phys. Rev. Lett. **68,** 1943 (1992).

[7]M. Altarelli, Phys. Rev. B **47,** 597 (1993).

[8]P. Carra, B. T. Thole, M. Altarelli, and X. Wang, Phys. Rev. Lett. **70,** 694 (1993).

[9]T. Jo, Electron Spectrosc. Relat. Phenom. **86,** 73 (1997).

[10]S. Qiao, A. Kimura, H. Adachi, K. Iori, K. Miyamoto, T. Xie, H. Namatame, M. Taniguchi, T. Muro, S. Imada, and S. Suga, Phys. Rev. B **70,** 134418 (2004).

[11]S. Qiao, A. Kimura, H. Adachi, T. Kambe, K. Yoshikawa, K. Yaji, C. Hirai, H. Sato, Y. Takeda, H. Namatame, M. Taniguchi, A. Tanaka, T. Muro, S. Imada, and S. Suga, Physica B **351,** 333 (2004).

[12]Y. Teramura, A. Tanaka, and T. Jo, J. Phys. Soc. Jan. **65,** 1053 (1996).

[13]J.-G. Cheng, J.-S. Zhou, J. B. Goodenough, Y. T. Sui, and Y. Ren, Phys. Rev. B **84,** 104415 (2011).

[14] A. Iyama, J. –S. Jung, E. Choi, J. Hwang, Y. Wakabayashi, and T. Kimura, J. Phys. Soc.

Jpn. **81,** 013703 (2012).

[15]J. -S. Jung, A. Iyama, H. Nakamura, Y. Wakabayashi, and T. Kimura, Phys. Rev. B **85,** 174414 (2012).

Chapter 6.

Conclusion

Accomplishments obtained in this work

The main targets of this thesis are as follows:

1. **Discovery of magnetic field effects on dielectric and magnetic properties in A-type antiferromagnetic and *N*-type ferrimagnetic $SmMnO_3$.**
2. **Development of approaches to resolve origin of dielectric dispersion in *R*MnO_3.**
3. **Understanding significant lattice distortion induced by change in magnetic configurations.**
4. **Clarification of complex magnetic states due to coupling between Sm 4*f* and Mn 3*d* moments to understand the microscopic origin of the magnetocapacitive effect in $SmMnO_3$.**

To achieve and reach these purposes, we have investigated the correlation between magnetic and dielectric properties in $SmMnO_3$ single crystals by means of macroscopic (magnetization, dielectric constant, and strain) measurements and microscopic (XMCD techniques) measurements. The obtained results through the measurements are:

[For purpose (1)]

We have succeeded in observing the magnetic field effect on the magnetic and dielectric constant and in discovering a new type of magnetodielectrics or magnetocapacitive effect coupled with an *N*-type ferrimagnet of A-type antiferromagnetic $SmMnO_3$ for the first time. Based on the obtained experimental results concerning magnetization and dielectric constant, we inferred that the canting angle of Mn moments is closely correlated to the magnetocapacitive effect and that simultaneous reversal of ferrimagnetically coupled Sm-Mn moments is ascribed to the large and abrupt magnetocapacitive effect at the first order-like-phase transition temperature. Hard XMCD results support our suggestion of simultaneously reversed Sm and Mn moments. However, we could not reach a conclusion to explain the microscopic origin of the magnetocapacitive effect using the obtained results.

[For the purposes (1) and (2)]

We have observed dielectric dispersion in $SmMnO_3$, which is always reported in rare-earth manganites regardless of ferroelectricity. We found the real and imaginary parts in the relative dielectric constant fit the Cole-Cole equation well, and the change in relaxation time by applying magnetic fields corresponds to the change in the canting angle of Mn moments. Although the microscopic mechanism of the correlation between the canting angle, and relaxation time, and of dielectric dispersion are still unclear, the findings of this study will provide a clue to understanding the dielectric dispersion observed in rare-earth manganites.

[For the purposes (1) and (3)]

We have found the magnetostrictive effect of $SmMnO_3$. A remarkable and discontinuous lattice distortion, which has never been reported, was observed at the first order transition temperature. The observed lattice distortion has been connected with variations of Mn moments. We concluded that orbital occupancy in Mn e_g electrons plays an important role in the magnetostriction.

[For the purposes (1), (3), and (4)]

Using the soft XMCD technique, we have investigated the magnetic states and the microscopic origin of the magnetocapacitive effect in $SmMnO_3$. We succeeded in obtaining XMCD signals from a single crystal of insulator $SmMnO_3$. We have verified that the angular momenta of Sm $4f$ and Mn $3d$ are simultaneously reversed at the transition temperature. Finally, we suggest that the microscopic origin of the magnetocapacitive effect is induced by an intimate combination among magnetic configurations, lattice distortion, and *p-d* hybridization.

Perspective and future work

In this thesis work, we discovered that A-type antiferromagnetic $SmMnO_3$ which does not show ferroelectricity exhibits a novel magnetodielectric(s) (effect) coupled with *N*-type ferrimagnetism. The obtained results attract attention to the multiferroics field, which is one of the hottest issues in condensed matter physics, to understand the origin of magnetoelectric coupling. We hope this result will trigger and develop research fields in magnetodielectrics and multiferroics scientifically and technologically.

We have suggested the observed magnetocapacitive effect is attributable to the simultaneous reversal of Sm 4*f* and Mn 3*d* angular moments and have proposed the origin is the close combination among magnetic configurations, lattice distortion, and *p-d* hybridization. Since the magnetic alignments of Sm 4*f* and Mn 3*d* moments in magnetic fields and the microscopic origin are still unclear, we need to perform neutron scattering measurements for a single crystal of $SmMnO_3$ to clarify the configurations and to discover materials which have similar physical properties to those of $SmMnO_3$. Based on the exact magnetic configurations of $SmMnO_3$ or on physical properties of other materials, it may lead to an understanding of the microscopic mechanism of the magnetocapacitive effect.

Appendix A. Orbital component θ calculation of $SmMnO_3$

Considering the e_g orbital ordering and its symmetry, the occupied ($|\pm\rangle^1$) and unoccupied ($|\pm\rangle^2$) e_g orbital wave functions[1] on the two inequivalent sites are given as:

$$|\pm\rangle^1 = \cos\frac{\theta}{2}|3z^2 - r^2\rangle \pm \sin\frac{\theta}{2}|x^2 - y^2\rangle$$

$$|\pm\rangle^2 = \pm\sin\frac{\theta}{2}|3z^2 - r^2\rangle - \cos\frac{\theta}{2}|x^2 - y^2\rangle,$$

where θ is the respective orbital component as mentioned in chapter 4. The simplest case is that the alternating $d_{3x^2-r^2}$ and $d_{3y^2-r^2}$ are ordered in $\theta = 120°$ as seen in Fig. A.

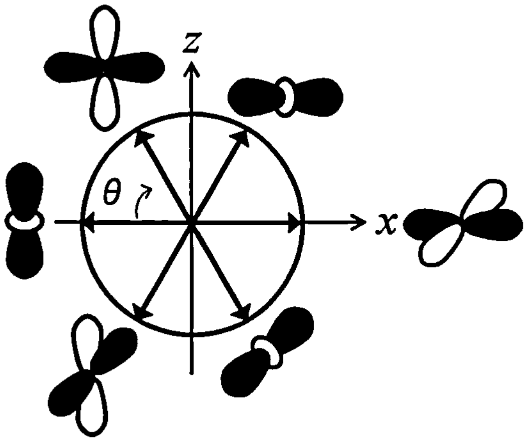

Figure A. The e_g orbital shape corresponding to the respective θ.

For obtaining the θ of $SmMnO_3$, the geometrical parameters which are directly related to the JT effect are necessary[2]. The local modes characterizing the JT effect in $LaMnO_3$ are defined as:

$$Q_2 = 2(l-s)/\sqrt{2} \text{ and } Q_3 = 2(2m-l-s)/\sqrt{6},$$

where m, l, and s are medium, long, and short Mn-O distances, respectively. The bonding (ψ_g) and antibonding (ψ_e) orbitals are determined as the linear function:

$$\Psi_g = c_1\phi_{x^2-y^2} + c_2\phi_{3z^2-r^2} \text{ and } \Psi_e = c_2\phi_{x^2-y^2} - c_2\phi_{3z^2-r^2},$$

where the coefficients c_1 and c_2 determining the orbital occupation describe the breaking of the degeneracy of e_g orbitals due to the JT effect. The coefficients c_1 and c_2 ($c_1^2 + c_2^2 = 1$) can be given by the relations:

$$\tan\varphi = Q_2/Q_3 \text{ and } \tan(\varphi/2) = c_1/c_2.$$

The calculated parameters and θ referred to by D. O'Flynn and coworkers[3] for $SmMnO_3$ at 1.5 and 300 K are displayed in Table A, including that of $RMnO_3$[4].

Table A. Calculated geometrical parameters and the θ of RMnO$_3$'s.

	$LaMnO_3$	**$NdMnO_3$**	**$SmMnO_3$**		**$TbMnO_3$**	**$DyMnO_3$**
	300 K	**300 K**	**1.5 K**	**300 K**	**300 K**	**300 K**
l	2.178	2.210	2.196	2.205	2.221	2.2238
m	1.968	1.953	1.939	1.944	1.940	1.9437
s	1.907	1.9087	1.913	1.910	1.905	1.903
Q_2	0.38325	0.42610	0.40004	0.41615	0.44690	0.45368
Q_3	-0.12166	-0.17367	-0.18811	-0.18606	-0.20069	-0.19547
$\tan\varphi$	-3.15024	-2.45354	-2.12659	-2.23659	-2.22672	-2.32098
$\tan(\varphi/2)$	-0.73174	-0.67229	-0.63481	-0.64829	-0.64712	-0.65802
c_2	0.807019	0.82989	0.84426	0.83909	0.83955	0.83537
c_1	0.590526	0.55793	0.53594	0.54398	0.54329	0.54969
$\cos(\theta/2)$	107.61	112.17	115.18	114.09	114.18	113.31
$\sin(\theta/2)$	72.39	67.83	64.82	65.91	65.82	66.69

[1] K. Tobe, T. Kimura, Y. Okimoto, and Y. Tokura, Phys. Rev. B 64, 184421 (2001).

[2] J. Rodríguez-Carvajal, M. Hennion, F. Moussa, A. H. Moudden, L. Pinsard, and A. Revcolevschi, Phys. Rev. B 57, R3189 (1998).

[3] D. O'Flynn, C. V. Tomy, M. R. Lees, A. Daoud-Aladine, and G. Balakrishnan, Phys. Rev. B 83, 174426 (2011).

[4] J. A. Alonso, M. J. Marínez-Lope, M. T. Casais, and M. T. Fernández-Díaz, Inorg. Chem. 39, 917 (2000).

Acknowledgements

This Ph.D. thesis could not have been completed without a number of people. My deepest gratitude goes out to Professor Tsuyoshi Kimura who always patiently helped me and generously supported all aspects of my life and study including my TOSHIBA internship in Japan. I also would like to thank Associate Professor Yusuke Wakabayashi and Assistant Professor Hiroyuki Nakamura. They have helped me to develop a deeper understanding of the research process and have mentored me well. I would like to express my appreciation to the members of Kimura lab: Dr. K. Kimura (graduated), A. Iyama, and T. Honda for their perceptive comments related to measurement methods and experimental results, and to all of previous and present master & doctoral degree students for their cooperation in all experiments and comments enriching my understanding of Physics. I am also grateful to Etsuko Hazama of Kimura lab for her constant support and help.

The research accomplishments listed in this thesis were contributed to by some collaborators. I am deeply grateful to Dr. M. Mizumaki and Dr. N. Kawamura (JASRI/Spring-8) for hard XMCD measurement, and to Dr. T. Nakamura (JASRI/Spring-8) and Associate Prof. Y. Shiratsuchi (Department of Materials Engineering, Osaka University) for soft XMCD measurement with sample preparation, explanation about the measurement method, and fruitful discussion about the obtained results.

I would like to express my eternal gratitude to my mother for always sacrificing herself for her sons and to my younger brother for always cheering me up. Also, I wish to thank friends in and out of Japan, especially, to Frank who has enormously affected my life. I am very thankful to all of Korean friends in Korea and Japan who have helped me overcome these tough times.

Finally, I would like to express my heartfelt thanks to Professor Tadashi Itoh and Professor Kazumasa Miyake at Osaka University for recommending Kimura lab and for their words of encouragement. I also thank Japanese government, which has helped to support me financially so that I have been able to concentrate on my studies.

List of Publications

---

[1] S. Danjoh, **J. -S. Jung**, H. Nakamura, Y. Wakabayashi, and T. Kimura
"*Anomalous induction of ferroelectric polarization by magnetization reversal in the phase-separated multiferroic manganite* $Eu_{0.8}Y_{0.2}MnO_3$"
Phys. Rev. B **80**, 180408(R) (2009).

[2] **Jong-Suck Jung**, Ayato Iyama, Hiroyuki Nakamura, Masaichiro Mizumaki, Naomi Kawamura, Yusuke Wakabayashi, and Tsuyoshi Kimura
"*Magnetocapacitive effects in the Néel N-type ferrimagnet* $SmMnO_3$"
Phys. Rev. B **82**, 212403 (2010).

[3] H. Nojiri, S. Yoshii, M. Yasui, K. Okada, M. Matsude, **J. -S. Jung**, T. Kimura, L. Santodonato, G. E. Granroth, K. A. Ross, J. P. Carlo, and B. D. Gaulin
"*Neutron Laue Diffraction Study on the Magnetic Phase Diagram of Multiferroic MnWO4 under Pulsed High Magnetic Fields*"
Phys. Rev. Lett. **106**, 237202 (2011).

[4] Ayato IYAMA, **Jong-Suck JUNG,** Eun Sang CHOI, Jungmin HWANG, Yusuke WAKABAYASHI, and Tsuyoshi KIMURA
"*High-magnetic-field effect on interplay between Sm 4f and Mn 3d moments in* $SmMnO_3$"
J. Phys. Soc. Jpn. **81** (2012) 013703.

[5] **Jong-Suck Jung**, Ayato Iyama, Hiroyuki Nakamura, Yusuke Wakabayashi, and Tsuyoshi Kimura
"*Lattice distortion accompanied by magnetization reversal in A-type antiferromagnetic manganites*"
Phys. Rev. B **85**, 174414 (2012).